

# **The role of barotropic and baroclinic waves in oceanic teleconnections**

by

**Sagar Bora**

A thesis submitted in partial fulfilment  
of the requirements for the degree of

**Doctor of Natural Sciences**

**in Physics**

to University of Bremen

Approved Referees

---

Prof. Dr. Gerrit Lohmann  
(Alfred Wegener Institute, University of Bremen)

---

Prof. Dr. Peter Lemke  
(Alfred Wegener Institute, University of Bremen)



# Acknowledgments

- I would like to acknowledge my supervisor, Prof. Dr. Gerrit Lohmann, for providing me the opportunity to work in this exciting project. His continued encouragement and support has been pivotal in the completion of this thesis project. He has shown me how to do research and how to think like a researcher.
- I would also like to acknowledge Dr. Sergey Danilov. Most of what I know about oceanic waves has been an accumulation from a myriad of discussions I had with Dr. Sergey Danilov. He has always had his door open so I could spontaneously drop by his office any time when I had a question in my mind. I thank him for sharing his knowledge with me.
- I would also like to acknowledge Prof. Dr. Peter Lemke for being a reviewer of this thesis. I thank him for his insightful discussions on climate science in lectures during my Masters and PhD.
- I would also like to acknowledge the "Earth System Science Research School (ESS-ReS)", an initiative of the Helmholtz Association of German research centres (HGF) at the Alfred Wegener Institute for Polar and Marine Research. I would like to thank Dr. Klaus Grosfeld for organizing many helpful lectures and soft-skill trainings during the last three years.
- I've been associated with the Paleoclimate group of the AWI for years now. I thank all my colleagues from my group who have provided me valuable inputs from many discussions regarding this project. Special thanks to my office mates and friends:

Christian Stepanek, Gong Xun, Xu Zhang, Michael Staerz, Paul Gierz and Conor Purcell for always answering any spontaneous question that popped into my head. I would also like to thank Conor and Krissy for correcting all the grammatical and spelling errors.

- I would like to thank the AWI for providing me with all the infrastructural needs I had during the PhD
- I would like to thank all my friends for keeping me fantastic company for the many good years that I have spent in Bremen. Many thanks to all of you, specially to name a few: Nikhil, Rahul, Abhinav, Iza, Ina, Maria, Upakul, Mara...Thanks for always making sure that I was never bored or down. Thanks to my friends back home in Guwahati as well.
- Lastly, I would like to acknowledge the tremendous support I have always received from my family and my girlfriend Diana. I thank them all for keeping me in their thoughts. Mom, dad, my sister Tina and Diana...well, you four have always been there - for better and for worse. Thank you for always believing in what I have pursued and for always being there and supporting me throughout the journey.

# Abstract

Buoyancy forcing in the high latitudes and variability in North Atlantic Deep Water formation leads to weakening of the Meridional Overturning Circulation (MOC). Perturbations at the high latitudes of the North Atlantic are adjusted via coastally trapped waves, equatorial Kelvin waves and westward propagating Rossby waves. This thesis works towards understanding the importance of oceanic teleconnections in transmitting variability through wave mechanisms.

The effect of mesh resolution on off-shore decay characteristics and phase speed of baroclinic Kelvin waves is examined analytically and through a series of numerical simulations performed with a reduced-gravity Finite Element Shallow Water Model. The mesh resolution is refined down to 5 km at the coast and 20 km at the equator to resolve first mode of the baroclinic Kelvin waves. A parameter  $\Delta$  is defined to be the ratio of horizontal mesh resolution and Rossby radius. A stable off-shore decay structure is found for any  $\Delta$  for coastal Kelvin waves in a finite element shallow water model with unstructured triangular  $P_1 - P_1$  mesh. For  $\Delta \ll 1$ , the off-shore decay structure of a Kelvin wave resembles the off-shore decay structure of a classical Kelvin wave. For  $\Delta > 1$ , the off-shore decay structure broadens with increasing  $\Delta$ , however, the overall adjustment via westward propagating Rossby wave is not strongly affected. The phase speed of the Kelvin wave is independent of  $\Delta$  on uniform meshes if consistent mass matrices are used. The numerical experiments also show that the Kelvin wave characteristics are hardly disturbed for a reasonable range of lateral viscosity. Results show that the finite element method with unstructured triangular grid is a convenient tool to represent wave dynamics in an

ocean model.

The time scale and amplitude of response to variability in MOC due to buoyancy forcing at high latitudes is analysed. Barotropic and baroclinic dynamics operating at different frequency ranges is also assessed using the Barotropic-Baroclinic Interaction (BarBI) model. It is found that there is an overestimation of the amplitude and time scale of response in experiments conducted on reduced gravity setups compared to the amplitude and time scales on BarBI which includes the interaction of waves with topography and background mean circulation. There is a significant reduction in amplitude of response, and increase in the time scales upon the interaction of waves with topography and a mean background circulation. It is also found that the response is highly dependent on the frequency of forcing. Barotropic dynamics dominate the high frequency regime while baroclinic dynamics dominate the low frequency regime. The response through barotropic dynamics is limited to the basin where the forcing was applied. Low frequency baroclinic adjustment is mainly responsible for propagation of variability into adjacent basins.

Furthermore, wave adjustment due to low frequency atmospheric variability over the North Atlantic, North Atlantic Oscillation, and over the South Atlantic, Southern Oscillation on ocean circulation is analysed via a series of numerical simulations. It is found that the magnitude of impact is significant in the hemisphere where the perturbation is applied and weakens significantly before reaching the opposite hemisphere, or another ocean basin.

# Contents

<b>Contents</b>	<b>v</b>
<b>1 Introduction</b>	<b>1</b>
<b>2 Key concepts and Model set up</b>	<b>7</b>
2.1 Shallow water equations . . . . .	7
2.2 Models and their grids . . . . .	9
2.2.1 Reduced gravity model . . . . .	11
2.2.1.1 Wave sensitivity to grid resolution and viscosity set-up .	12
2.2.1.2 Wave Sensitivity to frequency of forcing and wave path- ways . . . . .	13
2.2.2 BarBI . . . . .	15
2.2.2.1 Spin - up . . . . .	17
<b>3 Kelvin waves on <i>PI-PI</i> triangular grids in a Finite Element Shallow Water Model</b>	<b>21</b>
3.1 Shallow water equations in a Finite Element Model . . . . .	22
3.1.1 Dependence of phase speed on resolution . . . . .	25
3.1.2 The role of consistent mass matrices and stabilization . . . . .	25
3.2 Kelvin wave in Finite Element Shallow-Water Model . . . . .	27
3.2.1 Dependence of Kelvin wave on viscosity . . . . .	35
3.2.2 Dependence of Kelvin wave on mesh resolution . . . . .	45

3.3	Discussion . . . . .	50
<b>4</b>	<b>Dependence of oceanic wave adjustment on frequency of variability and topography</b>	<b>53</b>
4.1	Dependence of tropical response on the frequency of high latitude perturbation . . . . .	54
4.1.1	Set-up of experiments . . . . .	54
4.1.2	Tropical response to high latitude forcing . . . . .	55
4.2	Global wave adjustment to high latitude white noise forcing . . . . .	58
4.2.1	Setup of the 3 experiments . . . . .	58
4.2.2	Results . . . . .	58
4.2.2.1	Global oceanic wave adjustment as a function of frequency of forcing . . . . .	59
4.2.2.2	Wave adjustment in the <i>reduced gravity</i> setup . . . . .	66
4.2.2.3	Wave adjustment in the <i>no spin-up</i> setup . . . . .	69
4.2.2.4	Wave adjustment in the <i>with spin-up</i> setup . . . . .	72
4.2.2.5	Amplitude of response in the three setups . . . . .	75
4.2.2.6	Time scale of adjustment in the three experiments . . . . .	78
4.3	Discussion . . . . .	80
<b>5</b>	<b>Oceanic wave adjustment due to low frequency atmospheric variability</b>	<b>83</b>
5.1	Model set up . . . . .	83
5.2	Results . . . . .	86
5.2.1	SAM perturbation . . . . .	86
5.2.1.1	How SAM affected SO . . . . .	86
5.2.1.2	Wave adjustment in the Atlantic, Pacific and Indian Ocean . . . . .	87
5.2.2	NAO perturbation . . . . .	93
5.3	Conclusion . . . . .	98
<b>6</b>	<b>Summary and Outlook</b>	<b>101</b>

<b>Bibliography</b>	<b>105</b>
<b>List of Figures</b>	<b>113</b>

# Chapter 1

## Introduction

The large heat capacity of water enables ocean basins to regulate the Earth's climate by interacting with the atmosphere in various ways. Differential heating from the Sun's radiation leads to differences in density with latitude, which leads to mixing and large scale circulation of water. Along with wind driven upwelling and downwelling, horizontal and vertical density gradients generate a global ocean circulation called the thermohaline circulation (THC) eg. Rahmstorf (2006). Zonally integrated transport of this ocean circulation is known as the meridional overturning circulation (MOC). Figure 1.1 shows a schematic picture of the path of the mixed thermohaline and wind driven circulation.

The MOC globally transports approximately 20 Sv ( $1 \text{ Sv} = 10^6 \text{ m}^3/\text{s}$ ) of warm water northwards and approximately 1.2 PW ( $1 \text{ PW} = 10^{15} \text{ W}$ ) of heat (Macdonald and Wunsch, 1996; Roemmich and Wunsch, 1985). The Atlantic component of the MOC is unique as the surface flow of warm water is directed northwards from the Southern Hemisphere. Due to this large heat transport, the North Atlantic is  $\sim 5 \text{ K}$  warmer than similar regions in the Pacific Ocean leading to warmer conditions in north-western Europe compared to similar latitudes in North America (Peixoto and Oort, 1992). Hence, both regional and global variations of the MOC can have a severe impact on climate. Collapse of the THC can lead to cooling of the Northern Atlantic and warming of the Southern Atlantic (Vellinga and Wood, 2002; Knutti et al., 2004; Manabe and Stouffer, 1993; Delworth

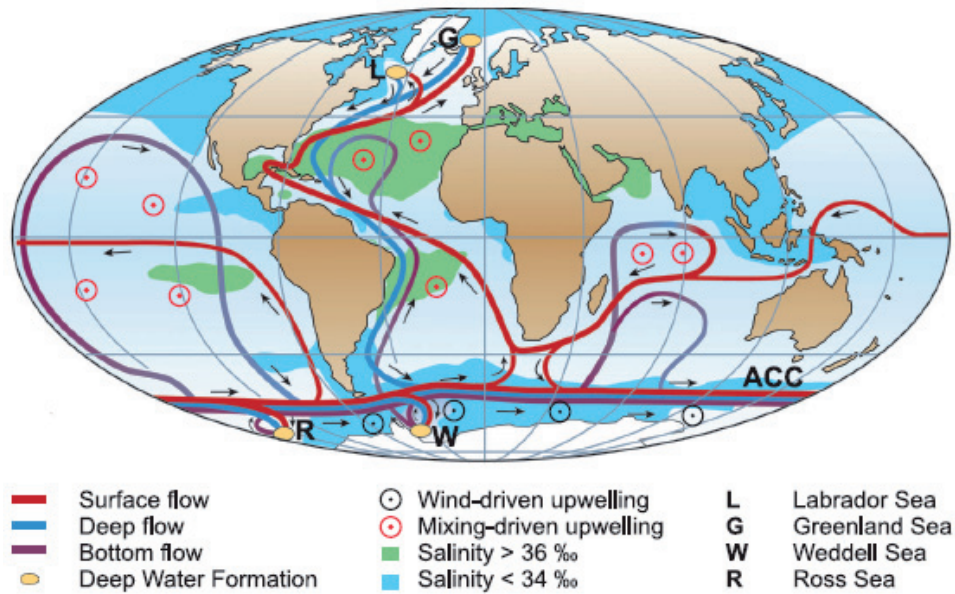


Figure 1.1: Ocean thermohaline circulation with sinking site and upwelling sites marked (Broecker, 1991; Rahmstorf, 2006).

et al., 1993).

Variations of the MOC can be induced via:

i) buoyancy perturbation eg. localised variations in the North Atlantic Deep Water (NADW) formation.

ii) wind driven disturbances, for example large scale, low frequency, basin wide atmospheric pressure modes like the North Atlantic Oscillation (NAO) (Wallace, 1981; Walker and Bliss, 1932) or Southern Annular Mode (SAM) (Thompson and Wallace, 2000).

Paleoclimate records have shown variations in NADW formation, and it has been suggested that some of the recorded past climate shifts have occurred in response (Dansgaard et al., 1993). The ‘8200 yr BP’ cold event, recorded in the North Atlantic region, is an example of abrupt climate change. It has been proposed that any past shutdown or near shutdown of the Atlantic thermohaline circulation has been caused by freshwater input from the drainage of the Laurentide lakes leading to a dramatic cooling of the northern hemisphere (Barber et al., 1999; Lohmann, 2003).

Various studies of recent observational and hydro-graphic data sets have shown that NADW formation is subject to changes at frequencies ranging from semi-annual to decadal

(Aagaard, 1968; Clarke et al., 1990; Meincke, 1990; Dickson and Lee, 1988; Dickson et al., 1990, 1996; Dickson and Brown, 1994; Dickson et al., 1999; Schlosser and Bayer, 1991; Haekkinen, 1999, 2001; Bacon, 1998). Taking this into consideration, the question arises as through which oceanic route and via which mechanisms these buoyancy or wind driven perturbations are transmitted from one location of the ocean to another, and that can manifest into abrupt climate change. Anomaly transmission via advection is associated with decadal or larger timescales. The time scale of interest for abrupt climate change is on inter-annual to centennial range.

One possible mechanism of rapid variability transmission in the ocean is through coastally trapped waves and equatorial Kelvin wave propagation along the coast and the equator (Gill, 1982). Additionally, Rossby waves adjust the interior of the ocean (Kawase, 1987). As these waves can transmit variability from one ocean basin to another within a few years, they represent an oceanic route that allows fast teleconnections. Coastal waves, equatorial Kelvin waves and Rossby waves are observed via satellite altimetry in sea surface height signal (Chelton and Schlax, 1996; Polo et al., 2008) and in bathythermometric observation data sets from National Oceanographic Data Center, (Jacobson and Spiesberger, 1998). Using sea level data from stations along the western coast of North America, Meyers et al. (1998) observed coastally- trapped Kelvin waves following the 1982 - 1983 El Niño, along the western coast of North America, propagating at a speed of 2 - 3 m/s. Various analytical and modeling studies have shown that coastal waves and coastal Kelvin wave dynamics along western boundaries are important in generating westward propagating planetary Rossby waves that adjust the interior ocean (McCalpin, 1995; Milliff and McWilliams, 1994; Liu et al., 1999) Rossby waves also interact with the western boundary currents (Gulf Stream in the Atlantic and Kuroshio current in the Pacific Oceans) by intensifying or diverting them from their usual path (Jacobs et al., 1994). Cipollini et al. (2001) observed westward propagating Rossby waves in ocean colour data, suggesting that Rossby waves affect the biology of the ocean.

Due to the extreme complexity of the coupled ocean-atmosphere system, it is diffi-

cult to quantify the magnitude of the impact in one ocean basin caused by atmospheric variability or buoyancy perturbation in another basin via oceanic wave mechanism in modeling studies. As the coastally trapped waves and Kelvin waves propagate along the coast in a narrow channel whose width is defined by the Rossby radius of deformation, modeling them utilising a traditional model is rather difficult (Hsieh et al., 1983). Waj-sowicz and Gill (1986) showed that Kelvin wave speed and attenuation rate suffers due to poor resolution and high lateral viscosities in ocean general circulation models. Importantly, Doescher et al. (1994) reported significant differences in the dynamic response time of the overturning circulation to NADW perturbations in fine and coarse resolution structured meshes.

Studies have shown that waves generated by weakening of the MOC due to fresh-water discharge in the North Atlantic can deepen or uplift the thermocline in the Pacific Ocean by 10-20 m (Cessi et al., 2004; Timmermann, 2005; Timmermann et al., 2005). Displacement of the thermocline with such amplitudes can intensify or suppress ENSO in the Pacific Ocean (Timmermann, 2005).

Many of previous modeling studies to link variations in NADW and MOC variability through Kelvin and Rossby waves utilise idealised reduced gravity setups, which ignores the interaction of these waves with topography, bathymetry and circulation (Huang et al., 2000; Hsieh and Bryan, 1996; Johnson and Marshall, 2002, 2004; Cessi et al., 2004). Presence of topography and continental shelves can distort the phase speed of a Kelvin wave (Gill, 1982). Since the anomaly (isopycnal displacement in this case) signal sits on the upper layer of the ocean in a reduced gravity setup, the influence of the bottom topog-raphy is not represented. The interaction of waves with the mean background circulation is also critical in modeling studies (Fevrier et al., 2007). The background circulation is as a rule neglected, and the experiments are started with basic state of the ocean at rest. With this in mind, the question arises as to what extent is the influence of wave propagation. One can expect bottom topography and ocean circulation to hinder wave propagation, attenuate the signal, and increase the adjustment time-scales. Nevertheless, a closer look

into the interaction of waves with these variables is imperative.

The time scale and amplitude response through wave adjustment also depends on the frequency of the perturbation (atmospheric or buoyancy) which causes it (Johnson and Marshall, 2002, 2004). However, different dynamics (barotropic or baroclinic) are dominant in different frequency ranges. To have a clear understanding of how important, and how influential are ocean teleconnections through waves, it is important to analyse the relationship between the amplitude of impact, frequency of variability, and the frequency ranges at which these mechanisms are dominant.

In order to study the influence of Kelvin waves in anomaly propagation through modeling studies, the first step is to correctly resolve or accurately simulate their phase speed and spatial structure in models. Furthermore, the time-scales and magnitude of impact of wave mechanisms depend on the interaction of waves with topography, the background mean circulation, and frequency of perturbation via atmospheric or buoyancy forcing. Hence, to understand the role of wave mechanisms in rapid anomaly propagation and their impact on climate, we must analyse how the amplitude and time scale of wave propagation is affected by bottom topography and background mean circulation, and which processes are active in which frequency ranges.

In order to address the question of dependence of global wave adjustment in the presence of background ocean circulation, realistic bottom topography, and to the frequency of forcing, we use an ocean general circulation model with triangular grids, BarBI (barotropic-baroclinic-interaction model) (Olbers and Eden, 2003). Although, the physics of BarBI is simplified to the basic dynamical processes, the model allows us to tackle barotropic and baroclinic dynamics in the presence of topography, bathymetry and circulation. BarBI also allows us to analyse the response in terms of barotropic and baroclinic dynamics as a function of frequency of forcing. The results from BarBI are compared with experiments performed with a Finite Element reduced gravity model, also on triangular grids. We analytically study the behavior of Kelvin waves on triangular grids

However, the question arises as to whether these models can simulate Kelvin waves

on triangular grids. Previous studies have shown that under certain conditions, traditional models utilising *B*-grids and *C*-grids have certain limitations. For baroclinic Kelvin waves, under poor resolution, the phase speed is distorted on *B*-grids, while strong grid scale oscillations occur on *C*-grids(Hsieh et al., 1983). We analytically study the behavior of Kelvin waves on triangular grids. In order to validate the analytical findings, we perform numerical simulations on structured and unstructured triangular grids of various resolutions. Results are compared with previous findings regarding the behavior of Kelvin waves on regular structured grid, and presented in Chapter 3.

This thesis will be structured as follows. A complete description of BarBI and its setup, in addition to the reduced gravity setup is presented in Chapter 2. Chapter 3 illustrates the analytical study of Kelvin wave properties on triangular grids and presents the results of numerical simulations performed to validate the analytical findings. In Chapter 4 and 5, i) the global ocean wave response, ii) interaction of wave with topography and circulation, and iii) the wave adjustment dependence on frequency of perturbation due to buoyancy and wind stress forcing respectively, are discussed.

# Chapter 2

## Key concepts and Model set up

### 2.1 Shallow water equations

Shallow water equations are a simplification of the Navier-Stokes equations for fluid motion under that assumption that the horizontal length scale is much greater than the vertical length scale:

$$\frac{\partial u}{\partial t} - fv = -c^2 \frac{\partial h}{\partial x} + \vartheta \nabla^2 u - du \quad (2.1)$$

$$\frac{\partial v}{\partial t} + fu = -c^2 \frac{\partial h}{\partial y} + \vartheta \nabla^2 v - dv \quad (2.2)$$

$$\frac{\partial h}{\partial t} + \frac{\partial u}{\partial x} + \frac{\partial v}{\partial y} = 0 \quad (2.3)$$

Here,  $u$  and  $v$  are zonal and meridional transport velocities respectively;  $c = \sqrt{g'h}$  is the (reduced) gravity wave speed;  $h$  is the surface displacement,  $f$  is the Coriolis parameter,  $\vartheta$  is the viscosity coefficient and  $d$  is the damping coefficient. As coordinates, we take the coast along the eastern boundary, with positive  $x$  going eastward (onshore), and introduce non-dimensionalization so that distances are scaled with Rossby radius  $L_R = c/f$ , and frequency, with the Coriolis parameter. The remaining dimensional factor (the phase speed  $c$ ) can be absorbed, for example in  $h$ , in which case  $u$ ,  $v$  and  $h$  will have same dimensionality of  $m^2/s$ .

A complete solution for a Kelvin wave can be derived by solving the shallow water equations for wave solutions at the boundaries. Detailed derivation can be found at Gill (1982). The solution for the amplitude of a Kelvin wave is given by  $\eta = \eta_0 e^{-y/L_R} G(x - ct)$ , where  $G$  is an arbitrary function,  $L_R$  is the Rossby radius of deformation. The amplitude of Kelvin waves decreases exponentially with increasing distance from the coast.

Kelvin waves can propagate quite fast (phase speed in the order of meters per second) and transmit an anomaly from one basin to the other. However, as they propagate in a narrow channel along the coast, resolving them with traditional models intended for climate studies is difficult (Hsieh et al., 1983), because the Rossby radius of deformation is 40 km or less in the mid and high latitudes. On coarse meshes, the propagation characteristics are sensitive to discretization. Since we use triangular meshes, in Chapter 3, Section 3.2, we look for solutions of the shallow water equations on discretised triangular grids and show that they are a proper tool to analyse the Kelvin wave propagation.

Rossby or planetary waves are another set of important waves adjusting the interior of the ocean. Their phase always propagate westward, and their phase speed decreases as one moves from the equator towards the poles. Rossby waves are generated at the western coast by boundary wave dynamics, or perturbations from the atmosphere, or internal ocean dynamics. Baroclinic Rossby waves propagate as isopycnal displacement, with amplitude of the order of  $\sim 50$  m (Gill, 1982). However, the reflection of such amplitude of isopycnal displacement on the sea surface height (SSH) is of the order of a few centimeters, making them difficult to observe. They have a typical phase speed of a few centimeters per second. As discussed in the Chapter 1, they are important in delaying the effects of climate events in the North Atlantic and the North Pacific oceans (El-Nino), intensifying western boundary currents. The dispersion relation of Rossby waves is given by:

$$\omega = \frac{-\beta k}{k^2 + l^2 + L_R^{-2}} \quad (2.4)$$

Figure 2.1 shows the dispersion relation of Rossby waves. We can see that Rossby

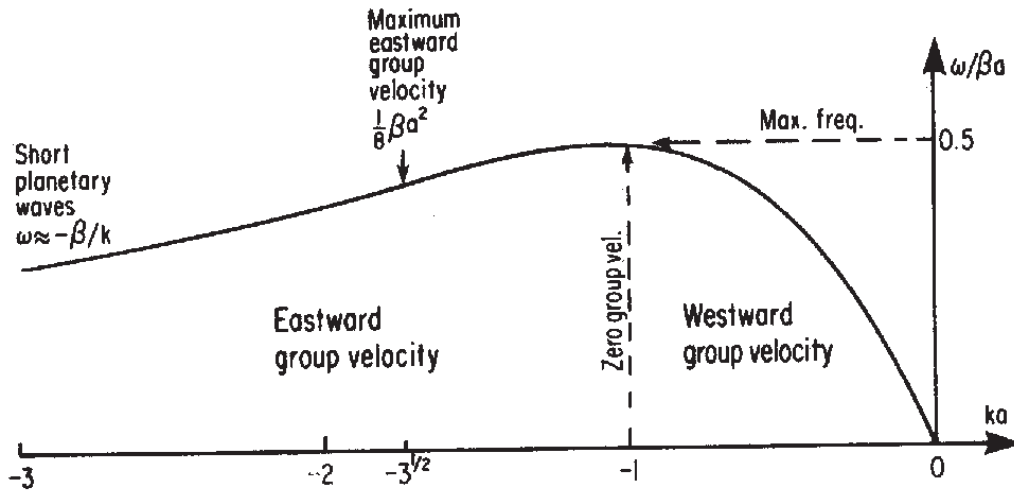


Figure 2.1: Properties of planetary wave dispersion relation(Gill, 1982)

waves can be separated into two groups: short Rossby waves with eastward group velocity and long Rossby waves with westward group velocity. We notice that at low frequency limits, only the long Rossby waves with westward group velocity exists. On the modeling studies described in this thesis, we will deal mostly with the long Rossby waves, as the short Rossby waves are dissipated quickly as their wavelength is short. Denoting viscosity by  $\nu$ , we estimate the dissipation time scale as  $\tau = \omega^2 / \beta^2 / \nu$ . Taking a period of  $N$  days, the estimate reduced to  $\tau = R_E^2 / (4N^2 \nu)$ , with  $R_E$  the Earth's radius, or  $\tau \approx 15$  days. for  $\nu = 100 \text{ m}^2/\text{s}$ , and a period of 3 years.

In chapter 4 and 5, the time-scales and importance of ocean adjustment through Rossby waves are discussed in details.

## 2.2 Models and their grids

In this thesis, two models are used to analyse the behavior of Kelvin waves and other coastally trapped waves, and to understand the magnitude of impact waves can have in oceanic teleconnections and propagation of anomaly generated by buoyancy and wind stress perturbations.

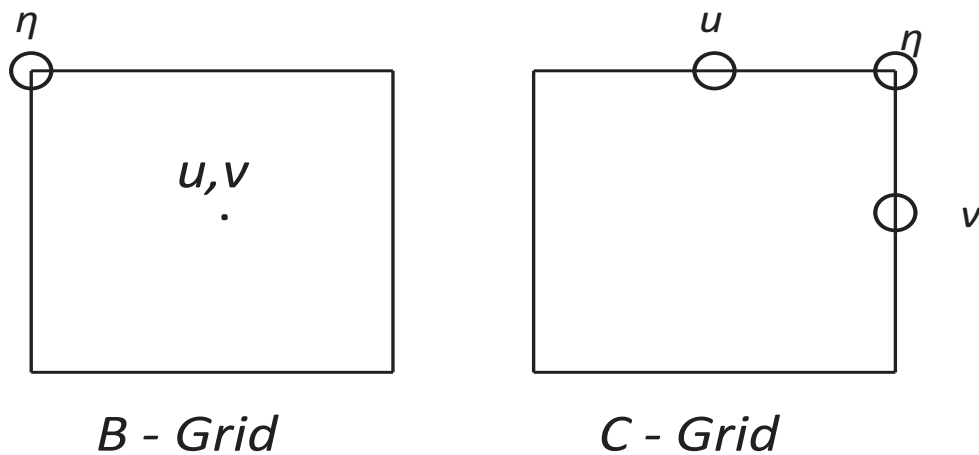


Figure 2.2: Location of the velocity components  $u$  and  $v$ , and the sea surface displacement  $\eta$  Arakawa  $B$  and  $C$  grids.

Most Ocean General Circulation models utilise Arakawa  $B$  or  $C$  grids. Figure 2.2 shows the location in  $B$  and  $C$  grids where the horizontal velocities and the surface displacement is calculated. Previous studies have shown that under certain conditions, traditional models utilising  $B$ -grids and  $C$ -grids have certain limitations. For baroclinic Kelvin waves, under poor resolution, the phase speed is distorted on  $B$ -grids, while strong grid scale oscillations occur on  $C$ -grids (Hsieh et al., 1983).

All the experiments here are performed on triangular  $P_1 - P_1$  grids. Hence, as a first step, we analytically study the behavior of Kelvin wave characteristics on triangular  $P_1 - P_1$  grids, and show that triangular grids are a proper tool to analyse Kelvin waves. Figure 2.4 shows the location of the velocity components  $u$  and  $v$ , and the sea surface displacement  $h$  in a  $P_1 - P_1$  grid. Numerical simulations were performed on a reduced gravity shallow water model with triangular grids to verify the analytical findings. Section 2.2.1 describes the setup of the experiments.

In order to understand of dependence of global wave adjustment in the presence of background ocean circulation, realistic bottom topography, and to the frequency of forcing, we use an ocean general circulation model with triangular grids, BarBI (barotropic-baroclinic-interaction model (Olbers and Eden, 2003)). Results from simulations on BarBI

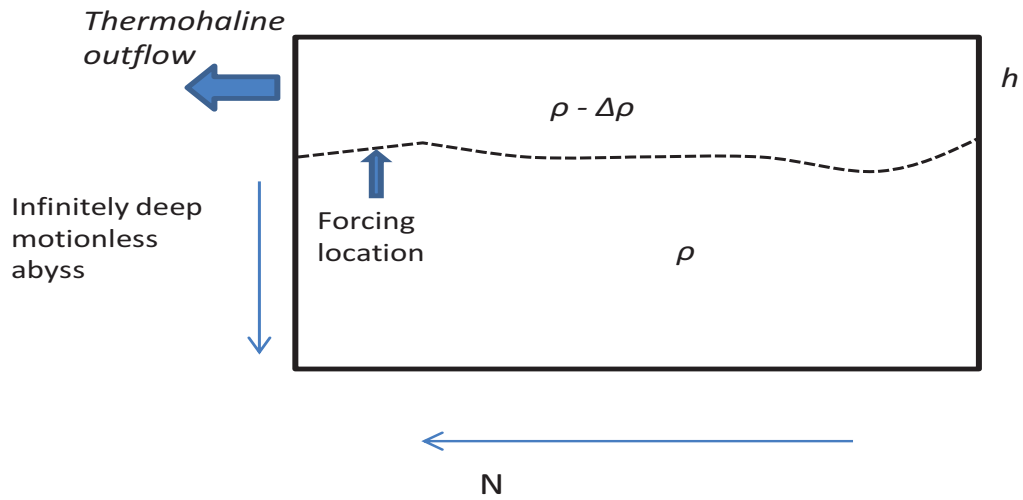


Figure 2.3: Shallow-water model with moving surface layer and infinitely deep, motionless, lower layer. Thermohaline overturning is represented by a prescribed outflow from the surface layer on the northern boundary. Different model domains are used for different experiments and they are described in the corresponding setup sections in this chapter.

are compared with identical experiments performed on a reduced gravity model based on shallow water equations with triangular grids and a reduced gravity setup.

### 2.2.1 Reduced gravity model

A shallow-water model based on  $P_1 - P_1$  discretization is used to perform sensitivity experiments to evaluate the dependency of Kelvin wave characteristics on triangular grids. It is derived from the Finite-Element-Ocean-Model (FEOM). FEOM is an ocean general circulation model, with an unstructured triangular surface mesh and prismatic volume elements, developed at the Alfred Wegener Institute (Danilov et. al. 2004).

Under a reduced gravity setup, the warm limb of the thermocline is represented by a moving surface layer (with an initial depth of 500 m in all the experiments) sitting on a infinitely deep motionless abyss (Figure 2.3). This setup does not include any mean background circulation.

Deep water formation is represented in this model as a prescribed outflow at the Labrador Sea. The model is forced by perturbing the deep water formation rate, or in other words, perturbing the prescribed outflow ( $T_N$ ) in the north-west corner or the Labrador Sea

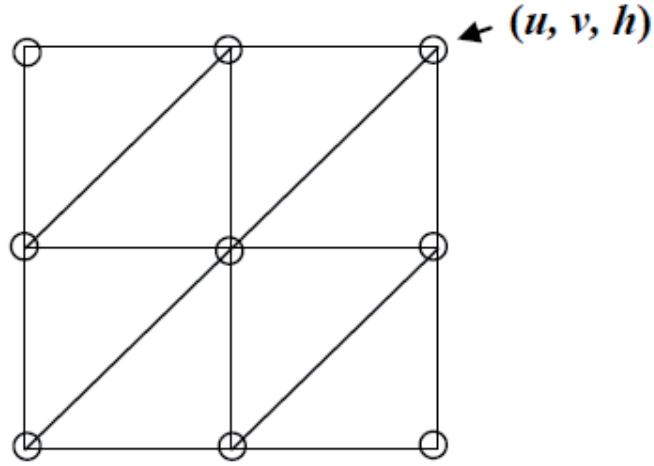


Figure 2.4: Location of the velocity components  $u$  and  $v$ , and the sea surface displacement  $h$  in a  $P_1 - P_1$  grid.

region of the domain. The perturbation is applied through the right hand side of equation 2.3 as:

$$\frac{\partial h}{\partial t} + \frac{\partial u}{\partial x} + \frac{\partial v}{\partial y} = \alpha(h^{obs} - h) \quad (2.5)$$

where  $\alpha$  is the rate of change and  $h^{obs}$  is an arbitrary amplitude. The perturbation is applied as:

$$\alpha(h^{obs} - h) = A(t)F(x_{lat}, y_{lon}) \quad (2.6)$$

where  $A(t)$  is a time dependent amplitude, and  $F(x_{lat}, y_{lon})$  is a Gaussian function centered at  $x_{lat}$  and  $y_{lon}$ .

### 2.2.1.1 Wave sensitivity to grid resolution and viscosity set-up

To test the sensitivity of Kelvin waves on grid resolution and viscosity, 5 grids covering a rectangular box were created, each with coastal resolution of: 7 km (henceforth termed as fine mesh), 50 km, 75 km, 100 km, and 125 km (henceforth termed as coarse mesh). This particular box set-up is used to isolate the effect of resolution and viscosity on wave propagation. A reduced gravity  $g'$  value of  $0.01 \text{ m/s}^2$ , and the layer thickness of 2000

$m$  is used in the setup. This gives us a mid-latitude deformation radius of  $\sim 40$  Km. The resolution at the equatorial region is also higher than the mid-latitude interior ocean to resolve the equatorial Kelvin wave. A perturbation is generated by switching on a transport anomaly  $T_N$ , at the north western corner of the domain with a prescribed Gaussian distribution  $F(x_{lat}, y_{lon})$  of 2 degrees in width centered at  $57.5^\circ$  N and  $57.5^\circ$  W which varies periodically in time ( $A(t)$ ) with a period of 10 years. Results are discussed in Chapter 3.

### 2.2.1.2 Wave Sensitivity to frequency of forcing and wave pathways

To test the dependence of the tropical response due to high latitude perturbation through waves on wave paths and frequency of perturbation, the reduced gravity setup mentioned above is used. A series of sensitivity tests are performed on a North Atlantic mesh with varying horizontal resolution. The horizontal grid resolution is set to 5 km near the coast, 20 km at the equator and  $\sim 100$  km at the mid-latitude interior ocean. Figure 2.5 a) shows the mesh used and Figure 2.5 b) shows a magnified part of the mesh of the Gulf of Mexico region, to illustrate the resolution of the mesh near the coast and equator. With a horizontal resolution of 5 km in the coastal regions, the mesh is resolving the Rossby radius and is capable of producing a Kelvin wave with the correct phase speed and off-shore decay structure. The depth of the layer is set to 500 m.

To test the sensitivity of the wave response to wave pathways and topography, a mesh of the North Atlantic without the Gulf of Mexico has been generated. The region of Gulf of Mexico, that has been removed, as shown in Figure 2.5 c). The coastal and equatorial resolution of the new mesh is same as above (5 km at the coast, 20 km at the equator and 100 km at the mid-latitude interior ocean).

A coarse mesh with a resolution of 1.5 degrees in the entire domain is created. The global coarse mesh does not resolve the Rossby radius of deformation at mid and high latitudes. However, as we show analytically and through a series of numerical simulations in Chapter 3, and Chapter 4, section 4.1.2, the numerical setup of the triangular grid can produce Kelvin waves & other boundary waves with a stable phase speed and off-shore

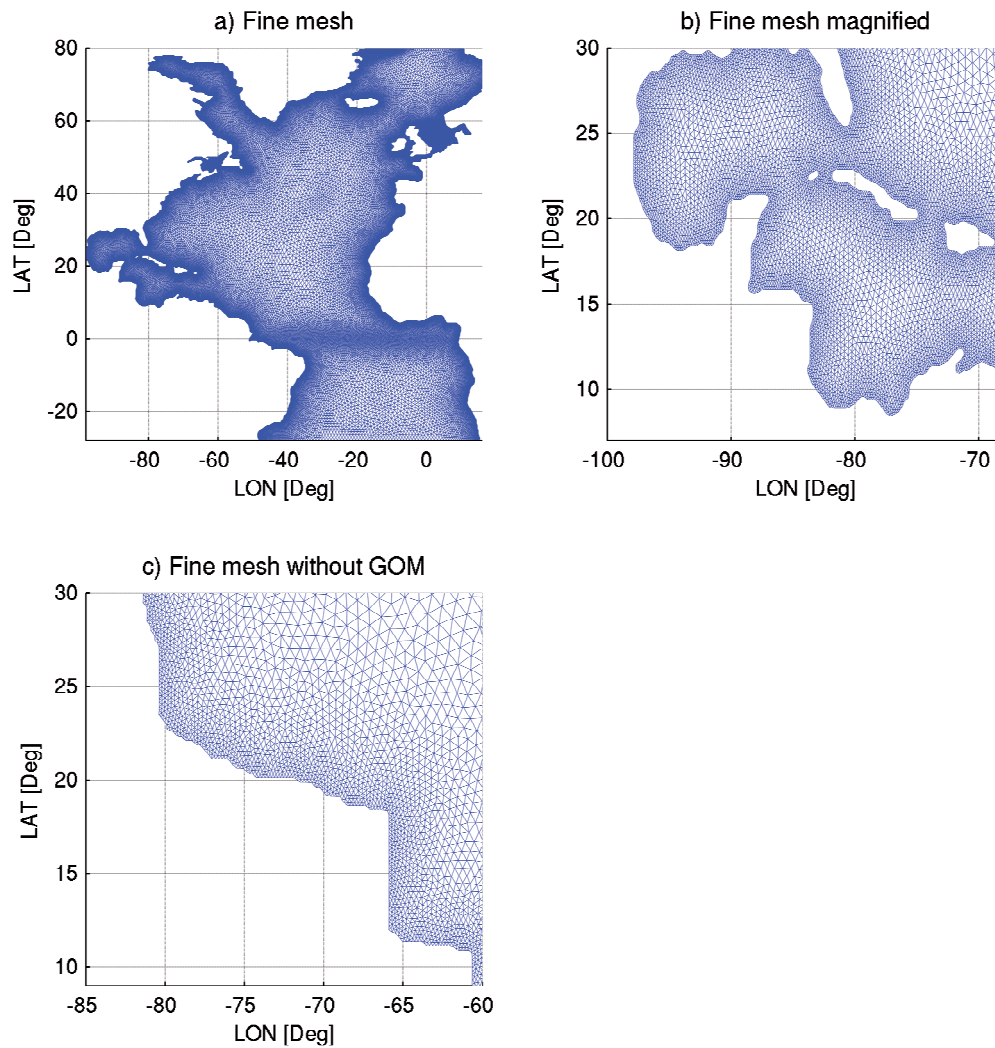


Figure 2.5: a) North Atlantic mesh; b) Magnified Gulf of Mexico of the North Atlantic mesh; c) Magnified region of the mesh without Gulf of Mexico

decay structure even when the Rossby radius of deformation is not resolved. In this mesh, a perturbation is generated by switching on a transport anomaly  $T_N$  with a white noise spectrum ( $A(t) \rightarrow$  white noise) at the Labrador Sea, and the adjustment process is compared with the adjustment process in BarBI simulating the barotropic and baroclinic flow under the influence of topography and circulation. The results are discussed in Chapter 4, section 4.2.2.

### 2.2.2 BarBI

BarBI is a simplified model derived from the primitive equations as described by Olbers and Eden (2003). The name is the abbreviation from "Baroclinic and Barotropic Interaction". The model in its simplest form reduces the dynamics to that of barotropic mode represented by the transport velocity  $U$ , and baroclinic mode represented by the potential energy  $E = g \int z \rho \mathbf{d}z / \rho_o$  and second velocity moment  $\mathbf{u}' = \int z^2 \mathbf{u} \mathbf{d}z$ . In the integrals above the integration is over the entire depth. The governing equations are:

$$\partial_t E + h \mathbf{U} \nabla \frac{E}{h^2} = \frac{N_o^2}{6} \mathbf{U} \cdot \nabla h^2 + \frac{N_o^2}{2} \nabla \mathbf{u}' + K \cdot \nabla^2 E + T_N \quad (2.7)$$

$$\partial_t \mathbf{U} + f \mathbf{k} \times \mathbf{U} = -h \nabla P - \nabla E + \tau_o + A_h \nabla^2 \mathbf{U} \quad (2.8)$$

$$\partial_t \mathbf{u}' + f \mathbf{k} \times \mathbf{u}' = \frac{h^2}{3} (\nabla E^2 - \tau_o - A_h \nabla^2 \mathbf{U}) + A_h \nabla^2 \mathbf{u}' \quad (2.9)$$

In this set of equations,  $h$  is the ocean depth,  $P$  the bottom pressure normalised with the reference density  $\rho_o$ ,  $N_o$  is the reference Brunt-Väisälä frequency,  $f$  the Coriolis parameter,  $T_N$  is the buoyancy forcing or transport anomaly applied at the Labrador Sea in certain experiments and  $\mathbf{k}$  the unit vertical vector. The set of equations above is complemented by the requirement that the barotropic transport velocity is divergence-free:

$$\nabla \cdot \mathbf{U} = 0 \quad (2.10)$$

Although BarBI represents a substantial simplification of real dynamics, it allows one to tackle, in the simplest form, dynamics of barotropic and baroclinic waves in the presence of topography, bathymetry and circulation. On one hand, other simplified systems, such as quasi-geostrophic two-layer equations, are only valid if variations of  $h$  are small. On the other hand, full primitive-equation ocean circulation model, usually using  $z$ -coordinate, will be suboptimal in representing coastally-trapped baroclinic Kelvin waves due to limitations on resolution. BarBI also allows us to analyse the wave response in terms of barotropic and baroclinic dynamics as a function of frequency of forcing, and understand the interaction of barotropic and baroclinic waves with topography and back-

ground mean ocean circulation. This explains our interest in using BarBI as a simplified system suitable to maintain dynamics of low-frequency waves in the ocean, to study the role of barotropic and baroclinic waves in fast oceanic teleconnections.

A comprehensive description of BarBI can be found in Olbers and Eden (2003). The original BarBI code was based on routines of a primitive equation model MOM (Pacanowski, 1995) and employed regular structured mesh. To better resolve coastally trapped Kelvin waves it was re-formulated to triangular meshes. The horizontal viscosity is set to  $A_h = 10^3 m^2/s$  and the eddy diffusivity  $K = 5 \times 10^2 m^2/s$ . The constant Brunt-Väisälä frequency is set to  $N_o = 2 \times 10^{-3} s^{-1}$ . BarBI is forced by surface windstress and a source of potential energy. For our purposes, we use two setups of BarBI, one without any background velocities, (referred to as *no spin-up* hereafter) and one with background velocities driven by wind stress (referred to as *with spin-up* setup hereafter). The *no spin-up* setup has no background circulation. The *with spin-up* setup is purely driven by a time mean windstress upto equilibrium. The spin-up is briefly discussed in the following section.

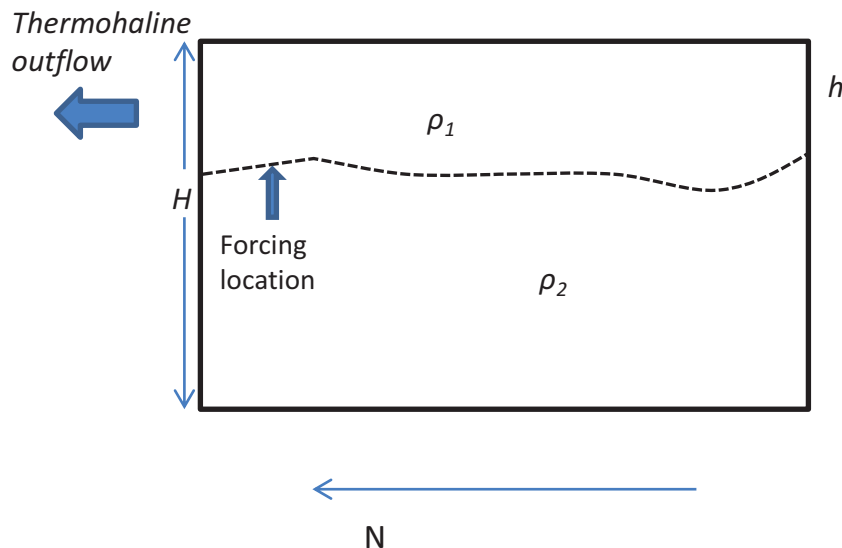


Figure 2.6: Two layer ocean to show the derivation of the buoyancy forcing in BarBI

In chapter 4, we compare the adjustment processes due to buoyancy forcing  $T_N$  at the Labrador Sea in setups with and without spin up. As in the reduced gravity setup,

the forcing in BarBI is applied at the Labrador Sea as a perturbation in the rate of deep water formation. The potential energy in BarBI is given by  $E = g \int z\rho dz / \rho_o$ , where  $\rho$  is a deviation from a mean background density profile  $\rho_o$ , given by the Brunt - Väisälä frequency  $N^2(z) = -g \frac{\partial \rho_o}{\partial z}$ , which is constant in our case. To be on the same footing in terms of forcing as the reduced gravity setup, let us consider a two layer ocean as show in Figure 2.6. Then, the potential energy can be written as:

$$E = g \int_{-H}^0 z\rho dz / \rho_o = \frac{g}{\rho_o} \left( \int_{-h}^0 z\rho_1 dz + \int_{-H}^{-h} z\rho_2 dz \right) \quad (2.11)$$

$$\partial_t E = \frac{1}{\rho_o} (\partial_t h(h\rho_1 g) - \partial_t h(h\rho_2 g)) = \frac{gh}{\rho_o} \partial_t h(\rho_1 - \rho_2) = -\frac{g\Delta\rho}{\rho_o} \frac{\partial_t h^2}{2} \quad (2.12)$$

From equation 2.12, we can approximately associate the response in potential energy to the response in equivalent depth of thermocline in BarBI, due to change in the rate of deep water formation. The forcing term  $T_N$  is applied as:

$$T_N = N^2 H h \partial_t h = N^2 H h (A(t) f(x_{lat}, y_{lon})) = B(t) f(x_{lat}, y_{lon}) \quad (2.13)$$

where  $B(t)$  is a time dependent amplitude and  $f(x_{lat}, y_{lon})$  is a Gaussian function centered at  $x_{lat}$  and  $y_{lon}$ . We select for  $B(t)$  the same white noise spectrum as in the reduced gravity setup for the buoyancy perturbation experiments. The results are shown in Chapter 4. For the wind stress perturbation experiments,  $B(t)$  is set to 0. The non-equivalence between BarBI and the reduced gravity setup comes from the fact that potential energy is quadratic in  $h$ . Hence, we discuss the response of reduced gravity setup in terms of potential energy as well (which is also quadratic in  $h$ ).

### 2.2.2.1 Spin - up

To generate a wind driven circulation, BarBI was forced from a state of rest with a time mean windstress  $\bar{\tau}(x, y)$  and integrated to equilibrium. The output was used as an initial

state for the *with spin-up* experiment as discussed in Chapter 4, and for the low frequency wind stress variability experiments as discussed in Chapter 5.

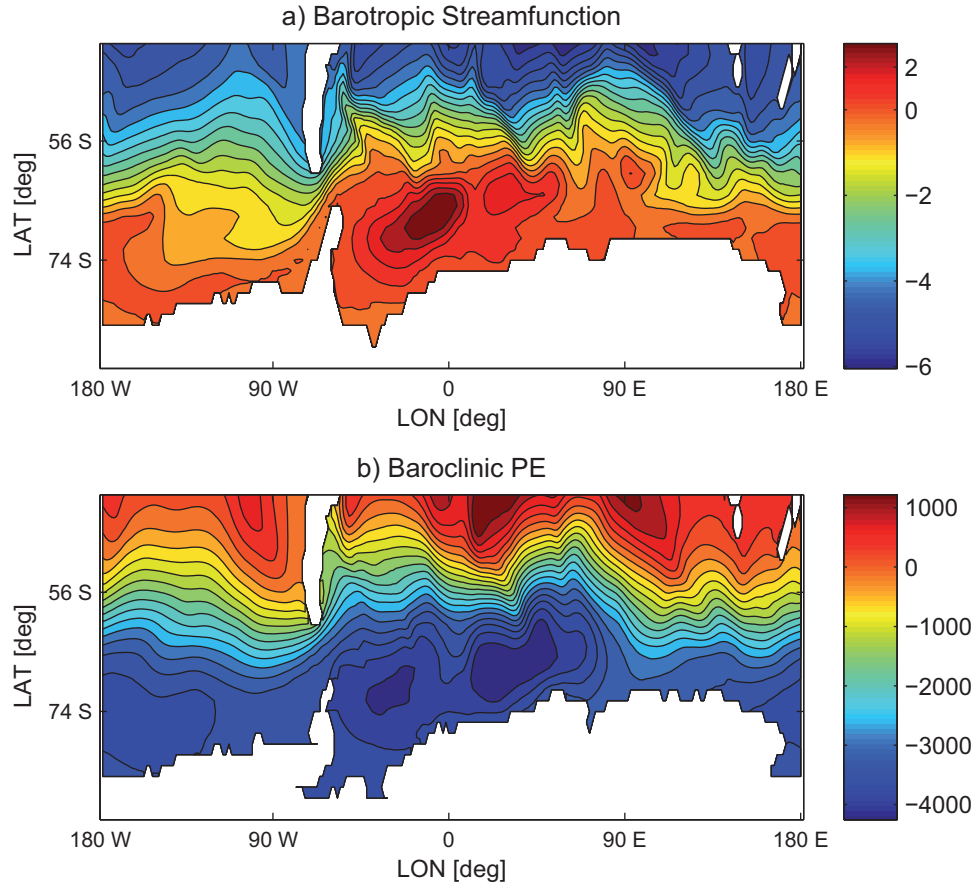


Figure 2.7: a) Barotropic streamfunction [Sv] and b) Baroclinic potential [ $m^3/s^2$ ] energy after 200 years of forcing BarBI with a time mean wind stress

Olbers et al. (2007a) have studied several steady state circulation of the Southern Ocean with barotropic and baroclinic conditions. Figure 2.7 a) and b) presents the steady state barotropic streamfunction and baroclinic potential energy (PE) respectively. Note that the barotropic streamfunction partly follows the topography and the pattern of potential energy is agreeing with the steady state simulated by Olbers et al. (2007b).

Figure 2.8 illustrates the development of the ACC transport from a state of rest, after switching on the time mean windstress  $\bar{\tau}(x,y)$ . The transport approaches equilibrium according to an exponential law. ACC reaches a steady state in approximately 60 years,

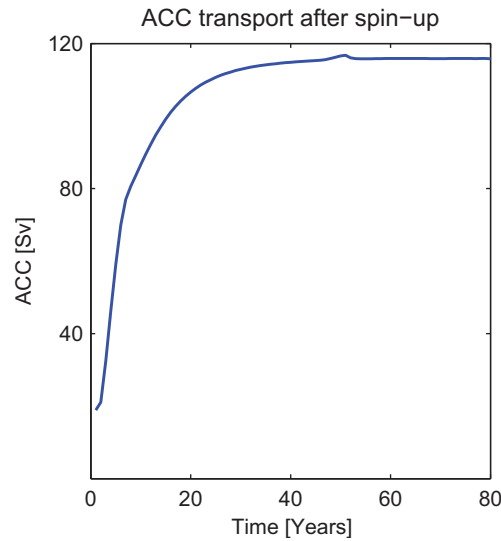


Figure 2.8: ACC transport in BarBI after switching on the time mean wind stress

and the transport is 120 Sv. The values agree well with previous simulation by Olbers and Lettmann (2007). A more detailed description of the spinup can be found in Olbers et al. (2007a) and Olbers and Lettmann (2007).

Figure 2.9 shows the steady state of the barotropic streamfunction of all the ocean basins after 200 years of forcing BarBI with a time mean windstress  $\bar{\tau}(x,y)$ . In both the Northern and Southern Hemisphere, BarBI produces a reasonable anticyclonic subtropical gyres in both Atlantic and Pacific Oceans. Note that the strength of the gyres is weaker than in observations as the BarBI was forced purely by windstress. For our study, the gyre strength suffices, as we study the first order wave interaction with currents in Chapter 4, and in Chapter 5 we study a purely wind driven wave adjustment mechanism.

At the Southern Ocean, we can see the current flows slightly northwards after passing the Drake Passage following the  $f/h$  contours as in Olbers and Lettmann (2007). BarBI also produces a strong anti-cyclonic subtropical gyre in the Indian Ocean with a strong southward flowing Mozambique current (Figure 2.9). This is of interest to us, as the Kelvin wave and other coastally trapped waves originated at the Atlantic Ocean propagates along the Cape of Good Hope into the Indian Ocean in the opposite direction of the currents. The interaction of the wave and the current is discussed in Chapter 4. The interaction of Rossby waves in the Pacific with the western boundary current is also briefly

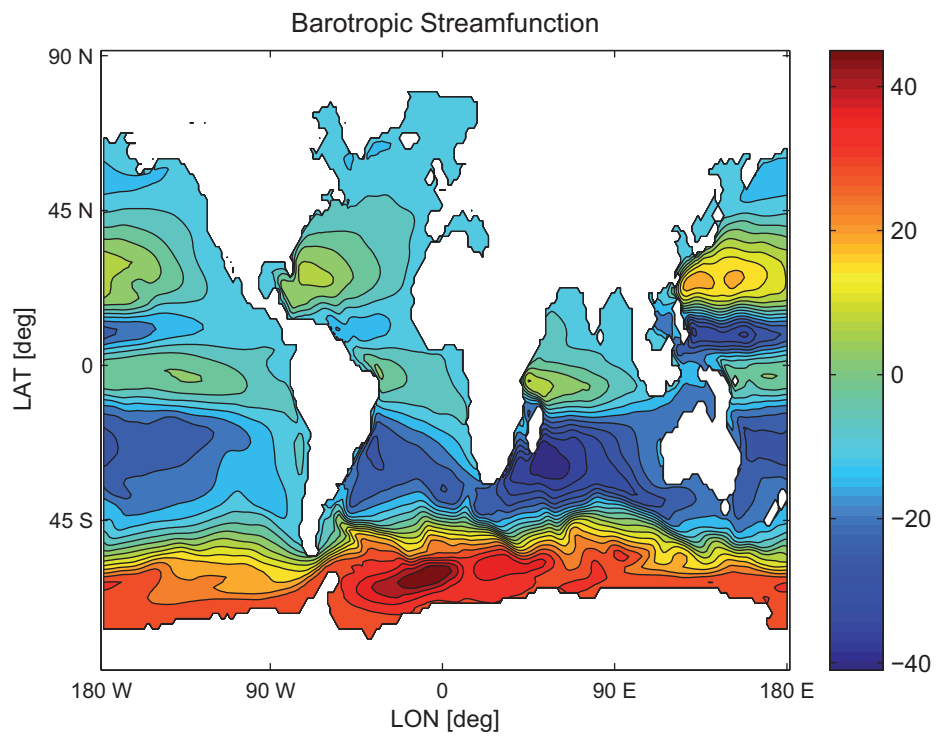


Figure 2.9: Steady state of all the ocean basins after 200 years of forcing BarBI with a time mean windstress  $\bar{\tau}(x,y)$ , in units of Sv.

discussed in Chapter 4 & 5.

## Chapter 3

# Kelvin waves on $P1$ - $P1$ triangular grids in a Finite Element Shallow Water Model

In this chapter, the dynamics of coastal Kelvin waves and other coastally trapped waves on a structured triangular mesh in shallow water model with element wise-linear  $P_1 - P_1$  representation of variables (Massmann et al., 2010) has been analytically studied. Numerical simulations have been performed on structured and unstructured triangular grids of various resolutions to validate the analytical studies. A reduced gravity setup is used, hence, the elevation of sea surface height (SSH) represents the displacement of isopycnals at the thermocline depth in the ocean. In section 3.1, the shallow water equations are introduced and solved using Finite-Element discretization with the standard Galerkin method to find the dependence of Kelvin wave phase speed and off-shore decay structure on mesh resolution and viscosity. The simulation results of dependence of Kelvin wave characteristics on mesh resolution and viscosities are discussed in section 3.2.

### 3.1 Shallow water equations in a Finite Element Model

We begin with the linearized shallow water equations written in the same notation as in Davey et al. (1983) [henceforth referred to as DHW]:

$$\frac{\partial u}{\partial t} - fv = -c^2 \frac{\partial h}{\partial x} + \vartheta \nabla^2 u - du \quad (3.1)$$

$$\frac{\partial v}{\partial t} + fu = -c^2 \frac{\partial h}{\partial y} + \vartheta \nabla^2 v - dv \quad (3.2)$$

$$\frac{\partial h}{\partial t} + \frac{\partial u}{\partial x} + \frac{\partial v}{\partial y} = 0 \quad (3.3)$$

Here,  $u$  and  $v$  are zonal and meridional transport velocities respectively;  $c$  is the (reduced) gravity wave speed;  $h$  is the surface displacement,  $f$  is the Coriolis parameter,  $\vartheta$  is the viscosity coefficient and  $d$  is the damping coefficient. We take the coast along the eastern boundary, with positive  $x$  going eastward (onshore), and introduce non-dimensionalization so that distances are scaled with Rossby radius  $L_R = c/f$ , and frequency, with the Coriolis parameter. The remaining dimensional factor (the phase speed  $c$ ) can be absorbed, for example in  $h$ , in which case  $u$ ,  $v$  and  $h$  will have same dimensionality of  $m^2/s$ . We consider wave solutions of the form:

$$[u, v, h] = [U, V, H] e^{ikx + ily - i\omega t} \quad (3.4)$$

Assuming alongshore geostrophy, performing finite-element discretization with the standard Galerkin method and  $P_1$  elements, and substituting the representation, equation 3.4, in the result, we reduce the original set of equations to:

$$V = G_x H \quad (3.5)$$

$$-i\omega V + U = -G_y H + DV \quad (3.6)$$

$$-i\omega H + G_x U + G_y V = 0 \quad (3.7)$$

In these equations,  $G_x$  and  $G_y$  are eigenvalues of  $x$  and  $y$  differentiation operators, respectively, for the discretization exploiting linear  $P_1 - P_1$  elements, and  $D$  is the respective

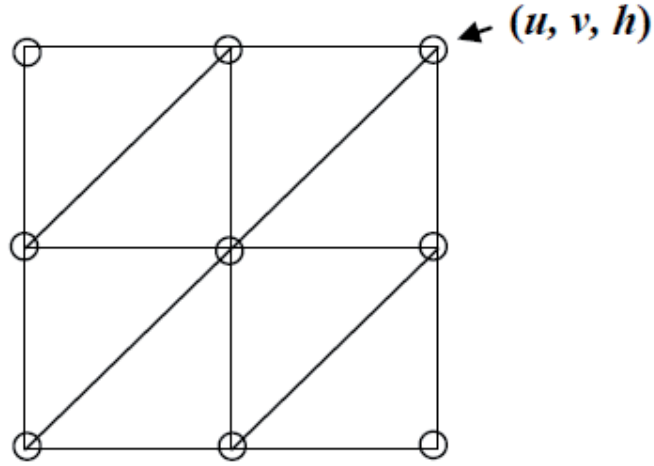


Figure 3.1: Location of the velocity components  $u$  and  $v$ , and the sea surface displacement  $h$  in a  $P_1 - P_1$  grid.

eigenvalue of dissipation operator. At the current stage, mass matrices are replaced by nodal quadratures for the sake of simplicity. Taking them into account would redefine  $\omega$  as  $\omega M/M_l$ , where  $M$  and  $M_l$  are the eigenvalues of consistent and lumped mass matrices (see further). The expressions for the eigenvalues depend on the mesh used and can be written in the analytical form only for uniform triangular meshes. Here we consider an example of mesh shown in Figure 3.1, the behavior in other cases is qualitatively similar. For the mesh of Figure 3.1, the standard Galerkin method gives:

$$G_x = \frac{i}{3\Delta}(2 \sin k\Delta - \sin l\Delta + \sin(k+l)\Delta) \quad (3.8)$$

$$G_y = \frac{i}{3\Delta}(2 \sin l\Delta - \sin k\Delta + \sin(k+l)\Delta) \quad (3.9)$$

and  $D = \vartheta L - d$  where

$$L = 2(\cos k\Delta + \cos l\Delta - 2)/\Delta^2 \quad (3.10)$$

with  $L$  being the eigenvalue of the Laplace operator, and  $\Delta$  the non-dimensional mesh spacing. Eliminating  $U$  and  $V$  from equation 3.5, 3.6 and 3.7 we end up with:

$$(-i\omega + i\omega G_x^2 + G_x D G_x)H = 0 \quad (3.11)$$

We will look into the case of no friction. The case with friction and viscosity will be discussed in more detail in the next section. So we have  $G_x^2 = 1$  or

$$G_x = \pm 1 \quad (3.12)$$

Bearing in mind the analogy to the continuous case, it is natural to expect that the positive root will be associated with the eastern boundary, and the negative one, with the western boundary. Having in mind typical applications, we consider the limit of long alongshore waves (same as in Hsieh et al. (1983)),  $l\Delta \ll 1$ . In this limit:

$$G_x \approx i \sin k\Delta / \Delta \quad (3.13)$$

Introducing the amplification factor  $\xi = e^{ik\Delta}$  in the zonal direction, we re-write equation 3.12 as:

$$\xi - 1/\xi = \pm 2\Delta \quad (3.14)$$

which should be solved for  $\xi$ . Note that because of particular form of equation 3.12, the solution to equation 3.14 comes in pairs  $\xi_1^\pm$  and  $\xi_2^\pm$ , where

$$\xi_1^\pm = \Delta \pm \sqrt{1 + \Delta^2} \quad (3.15)$$

$$\xi_2^\pm = -\Delta \pm \sqrt{1 + \Delta^2} \quad (3.16)$$

and,  $\xi_1^+$  and  $\xi_2^+$  are respectively the solution for eastern and western boundary. Their negative counterparts are spurious modes which oscillate on mesh scale. We did not see them in numerical simulations, presumably because of stabilization, on which we comment later. It can be readily shown that in the limit  $\Delta \ll 1$ , both  $\xi_1^+$  and  $\xi_2^+$  approach the respective theoretical result and  $k = 1$ . If the mesh is coarse,  $\xi_1^+$  and  $\xi_2^+$  describe

broader Kelvin waves than in theory. In this case, for example,  $\xi_2^+ \approx 1/2\Delta$ , so that broadening is  $\Delta/\ln(2\Delta)$ , which remains rather moderate unless the mesh is too coarse.

### 3.1.1 Dependence of phase speed on resolution

To look for the dependence of phase speed on a triangular mesh, we start with the continuity equation. As  $U = 0$ , we have

$$-i\omega + G_x G_y = 0 \quad (3.17)$$

which gives  $\omega = -iG_y$  for the eastern boundary. Hence it follows that

$$c_p = \frac{\omega}{l} \approx \frac{1}{3}(2 + \cos k\Delta) \quad (3.18)$$

The appearance of cosine owes its existence to the finite-element discretization which mixes meridional and zonal directions. For that reason  $G_y$  is not equal to  $il$  even for small  $l\Delta$  if  $k\Delta$  is not small. Since  $\cos k\Delta \sim \Delta$  on coarse meshes, wave propagates faster than in theory in that limit. In the other limit, we find theoretical prediction  $c_p = 1$ . As a whole, the behavior is similar to the B-grid case of Hsieh et al. (1983).

### 3.1.2 The role of consistent mass matrices and stabilization

Since  $PI$ - $PI$  pair is known to support pressure modes, the code we are using is stabilized as described in Massmann et al. (2010) and uses consistent mass matrices. Using consistent mass matrices effectively redefines frequency, but does not affect the localization. It can readily be shown that on the mesh selected by us, the eigenvalue

$$\frac{M}{M_l} = \frac{1}{6}(3 + \cos k\Delta + \cos l\Delta + \cos(k+l)\Delta) \quad (3.19)$$

$M_l$  equals twice the triangle area on the uniform mesh. In the limit of small  $l\Delta$  the eigenvalue reduces to:

$$\frac{M}{M_l} \approx \frac{1}{3}(2 + \cos k\Delta) \quad (3.20)$$

Direct comparison to the expression for  $c_p$  shows that making use of consistent mass matrices effectively eliminates the  $k$ -dependence up to terms of the first or higher order in small  $l\Delta$ , leaving  $c_p \approx 1$ . In this respect one gains the result of C-grid in Hsieh et al. (1983). Note, that the cancellation effect is not necessarily complete on non-uniform meshes, so that we cannot expect  $c_p \approx 1$  to hold in a general case.

The stabilization used by us works in time stepping mode so that we have to specify time stepping to express it in an analytical form. For simplicity, here we give the result for the case when the Coriolis, elevation and divergence terms are all implicit. Introducing the time amplification factor  $\lambda = \exp(-i\omega\tau)$ , where  $\tau$  is dimensionless time step, after some algebra, we obtain:

$$\frac{\lambda - 1}{\tau} \left[ 1 - \frac{\tau^2 \lambda}{(\lambda - 1)^2 + \tau^2 \lambda^2} (G_x^2 + G_y^2) \right] + \tau(\lambda - \gamma)(G_x^2 + G_y^2 - L) = 0 \quad (3.21)$$

Here the term proportional to  $\lambda - \gamma$  is the consequence of stabilization, and  $\gamma$  is the stabilization parameter which is selected as close to 1 as possible. In a situation relevant for baroclinic Kelvin waves  $\tau$  and  $\omega$  are both very small, so that  $(\lambda - 1)/\tau$  can be replaced with  $-i\omega$  and in all other cases  $\lambda$  can be replaced with 1. This reduces the dispersion equation to an easier recognizable form:

$$-i\omega \left[ 1 - \frac{1}{1 - \omega^2} (G_x^2 + G_y^2) \right] + \tau(1 - \gamma)(G_x^2 + G_y^2 - L) = 0 \quad (3.22)$$

On fine meshes, the difference of two Laplace operators,  $G_x^2 + G_y^2 - L$  is approximately  $\Delta^2/4$ , i.e., small, so that effects of stabilization should not noticeably modify the answer with respect to the unstabilized case. If, however,  $\Delta \gg 1$ ,  $G_x^2 + G_y^2 - L \approx 1$ , the effects of stabilization can indeed modify the result, especially if  $\omega$  is very small (periods from weeks to years are of interest to baroclinic dynamics). It is essential to keep  $\gamma$  as close to 1 as is compatible with the stale code performance to minimize them. We do not analyze

this limit case in more detail here. Note, however, that the overall effect of stabilization is damping, and also that for spurious modes,  $L$  tends to a constant value (for them  $\cos k\Delta < 0$ ) even for small  $\Delta$ , so the stabilization is strong for them.

## 3.2 Kelvin wave in Finite Element Shallow-Water Model

A shallow-water model based on  $P_1 - P_1$  discretization is used to perform sensitivity experiments to evaluate the dependency of Kelvin wave characteristics on triangular grids. The experiments were performed using a reduced gravity setup. The reduced-gravity model mimics the dynamics of the thermocline layer resting on an abyssal ocean layer. The reduced gravity was selected such that the model simulates the first baroclinic mode of Kelvin and Rossby waves. Phase speed of Kelvin wave in this set-up is given by  $c = \sqrt{g'H}$ , where  $g'$  is the reduced gravity (0.01 g) in this case, and  $H$  is the depth. Under a reduced gravity set-up, the SSH perturbations are considered to represent isopycnal displacement of a stratified ocean.

To test the sensitivity of Kelvin waves on grid resolution and viscosity, 5 rectangular grids with different resolutions were created, each with coastal resolution of: 7 km (henceforth termed as fine mesh), 50 km, 75 km, 100 km, and 125 km (hereafter coarse mesh). We use this particular set-up to isolate the effect of resolution and viscosity on wave propagation. A reduced gravity  $g'$  value of  $0.01 \text{ m/s}^2$ , and the layer thickness of 2000 m is used in the set-up. This gives us a mid-latitude deformation radius of  $\frac{\sqrt{g'H}}{f} \sim 40 \text{ Km}$ . To resolve the equatorial Kelvin wave the resolution in the equatorial region is also higher than the mid-latitude interior ocean .

A perturbation is generated by relaxing SSH to a prescribed Gaussian distribution of 2 degrees in width, centered at  $57.5^\circ \text{ N}$  and  $57.5^\circ \text{ W}$ , which varies periodically in time with a period of 10 years. Figure 3.2 shows the initial Kelvin wave adjustment process in the fine mesh. A coastal Kelvin wave carries the perturbation southward with a speed of  $\sim 4.2 \text{ m/s}$ , agreeing closely with the theoretical value in our set-up of 4.5

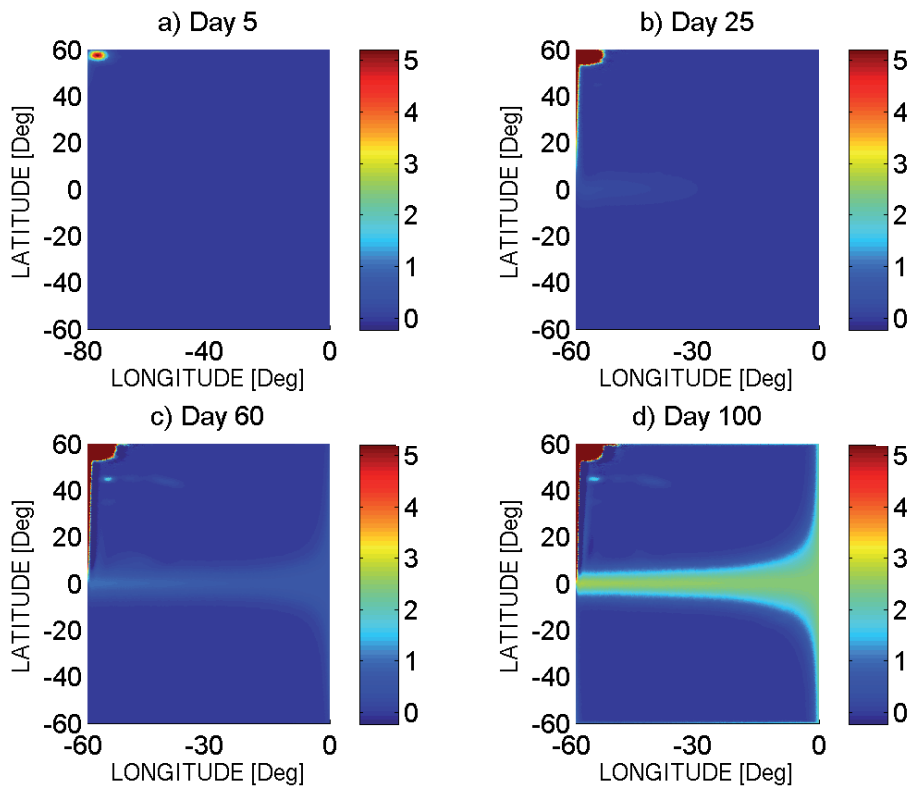


Figure 3.2: Kelvin wave adjustment in the North Atlantic after the SSH perturbation is turned on at the north-west corner of the domain. Wave propagates as a SSH (isopycnal displacement in reduced gravity set up) signal, with unit of meters.

m/s. It reaches the equator in a month. Then it turns and propagates eastward along the equator. After reaching the eastern coast the wave splits and propagates polewards in both hemispheres. Whilst propagating polewards, the Kelvin wave sheds westward propagating Rossby waves. Figure 3.3 shows the Rossby wave adjustment. From the shape of the wave-front we can see that the phase speed of the Rossby wave decreases as we move from the equator towards the pole. The Rossby wave propagates at a speed of a few cm/s and as we can see from Figure 3.3, it takes more than 4 years to reach the western boundary.

A zonal section of the ocean at 45 N for various resolution is shown in Figure 3.4. Along the western boundary, we can see the Kelvin wave propagating in a narrow section with width proportional to the Rossby radius. As the source of the forcing is oscillating with a period of 10 years, the amplitude of the Kelvin wave is maximum in 2.5 years, and

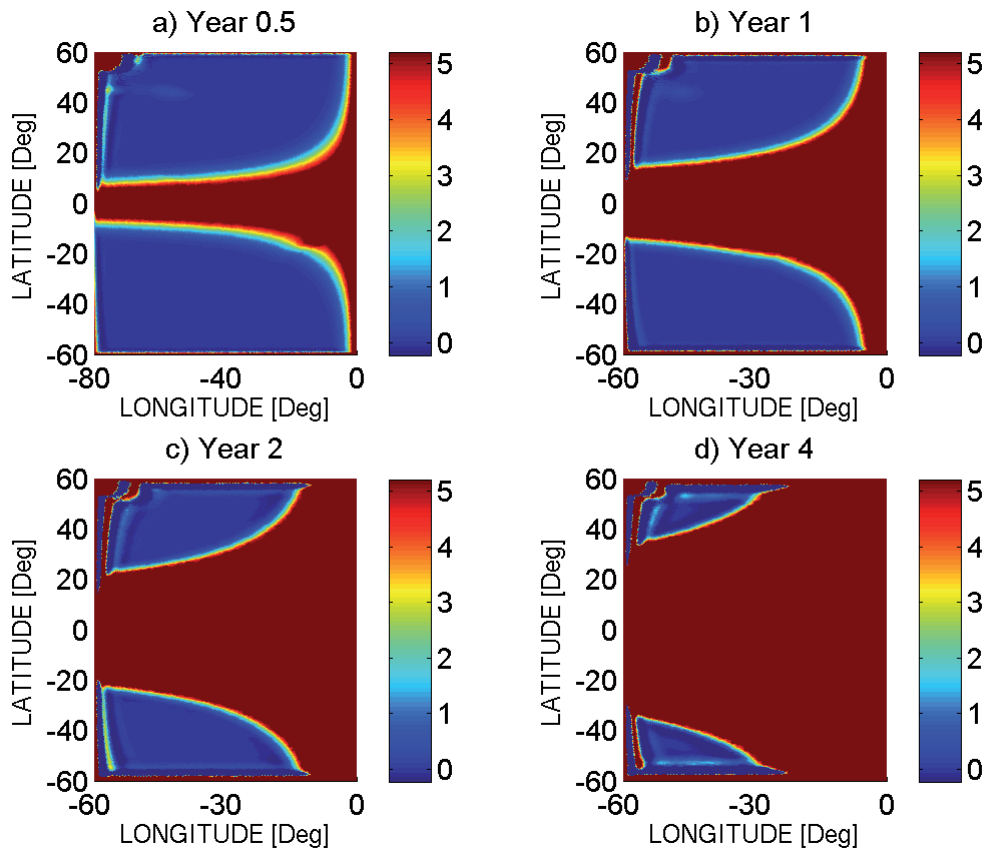


Figure 3.3: Rossby wave adjustment. Wave propagates as a SSH (isopycnal displacement in reduced gravity set up) signal, with unit of meters.

then it decreases. The width of the channel along which the Kelvin wave is propagating, increases with worsening resolution. The phase speed of the theoretical Rossby wave at 45 N is proportional to the Rossby radius and is  $\sim 2.5 \text{ cm/s}$ . The phase speed of the Rossby wave in the various meshes varies from  $\sim 2.3 \text{ cm/s}$  (fine mesh) to  $\sim 2.7 \text{ cm/s}$  (coarse mesh).

The theoretical phase speed of Rossby wave at 15 N is  $\sim 29 \text{ cm/s}$ . Figure 3.5 shows a zonal section along 15 N. The Rossby wave at this latitude has already reached the western boundary in 2 years. The following Figures 3.6 and 3.7 show the zonal section at 45 S and 15 S respectively, to show the propagation of Kelvin and Rossby waves in the Southern hemisphere. There is a clear difference in the response along the western boundaries of the Northern and the Southern hemispheres. This difference is due to the

buffer zone that the equatorial region creates by imposing restrictions on zonal pressure gradients (Johnson and Marshall, 2002). Hence, the response to the south of the equator is only due to Rossby wave adjustment.

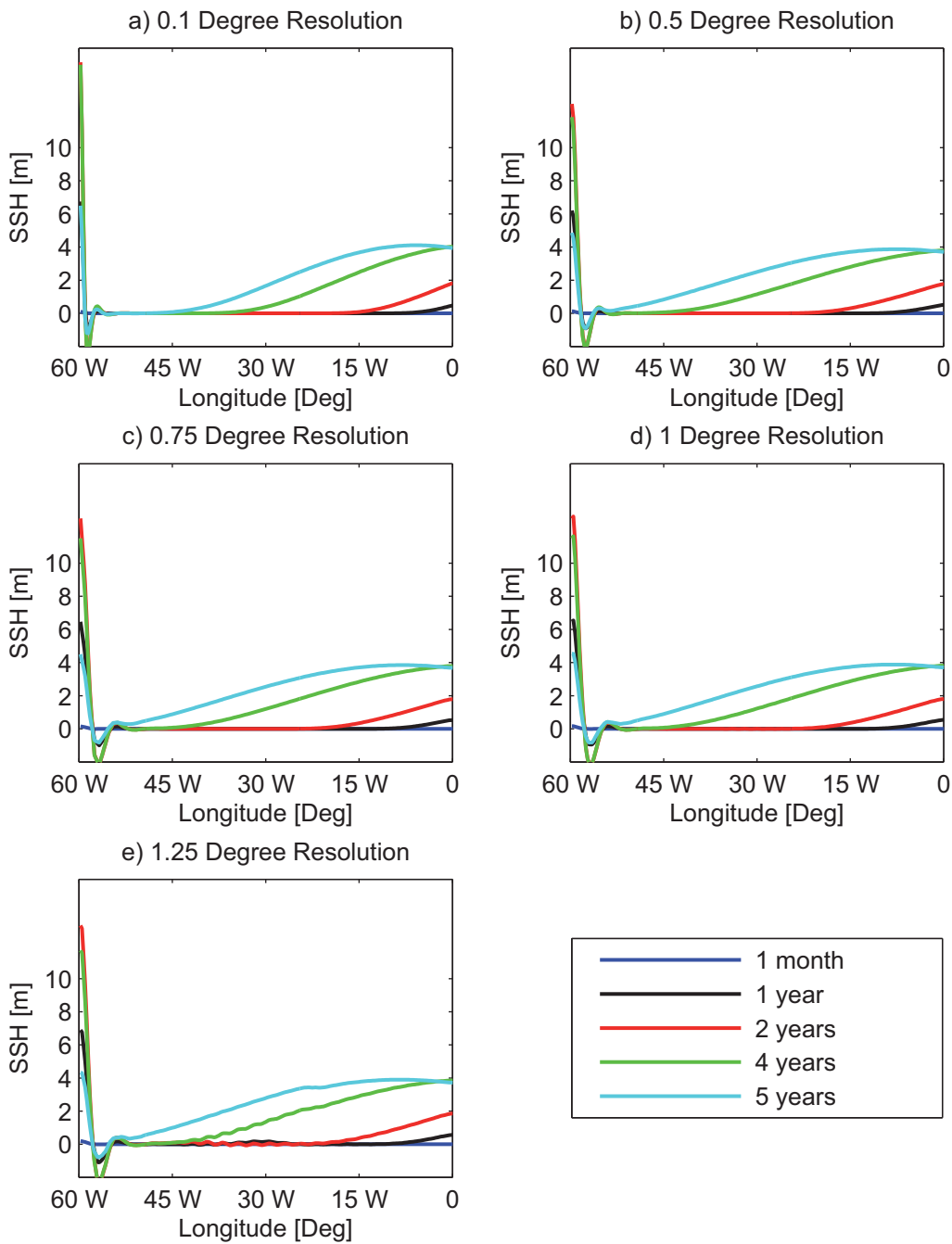


Figure 3.4: Evolution of coastal Kelvin waves and Rossby waves with time on various meshes at 45 N. Note that there is only marginal sensitivity to resolution for the Rossby waves.

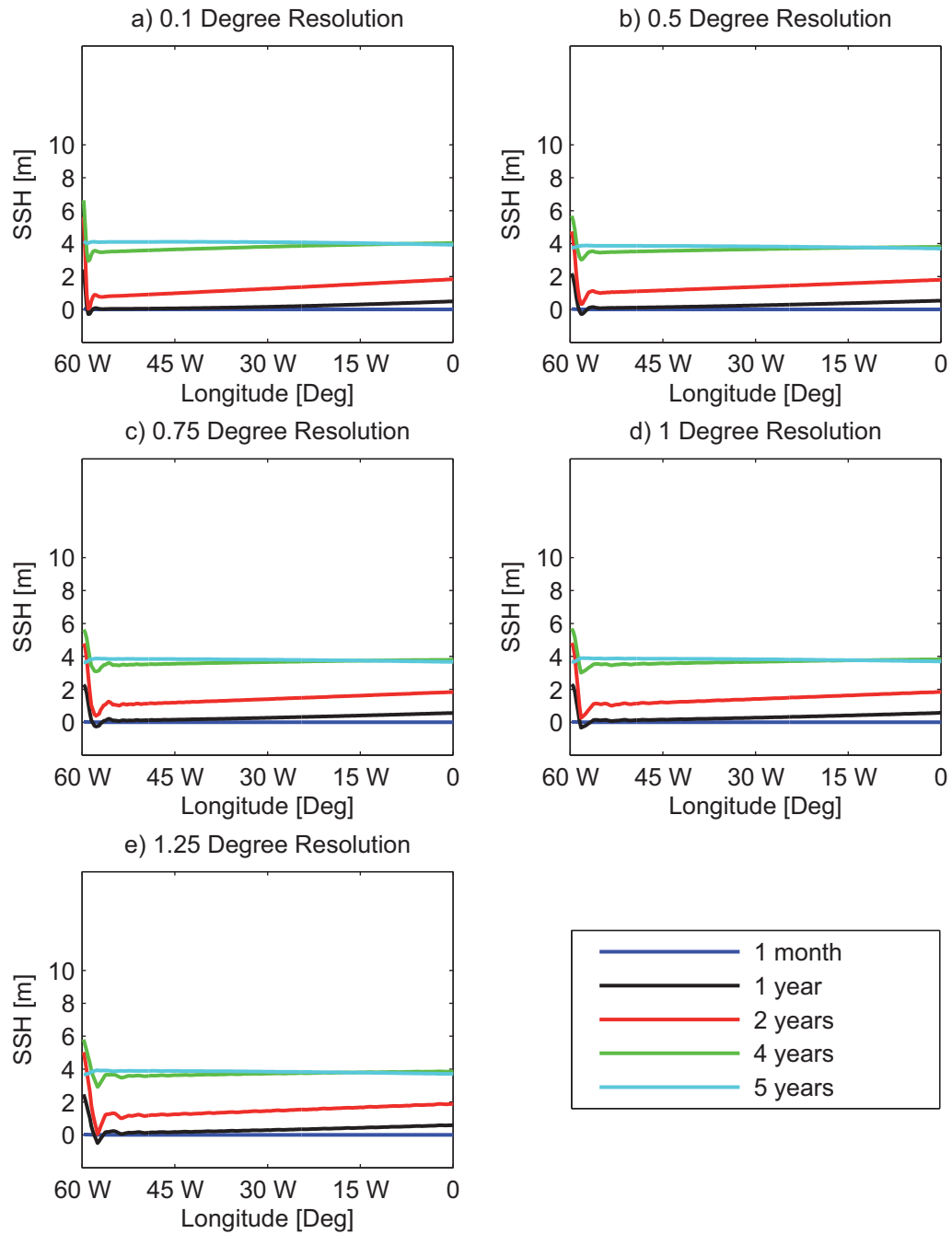


Figure 3.5: Evolution of coastal Kelvin waves and Rossby waves with time on various meshes at 15 N. Note that there is only marginal sensitivity to resolution for the Rossby waves.

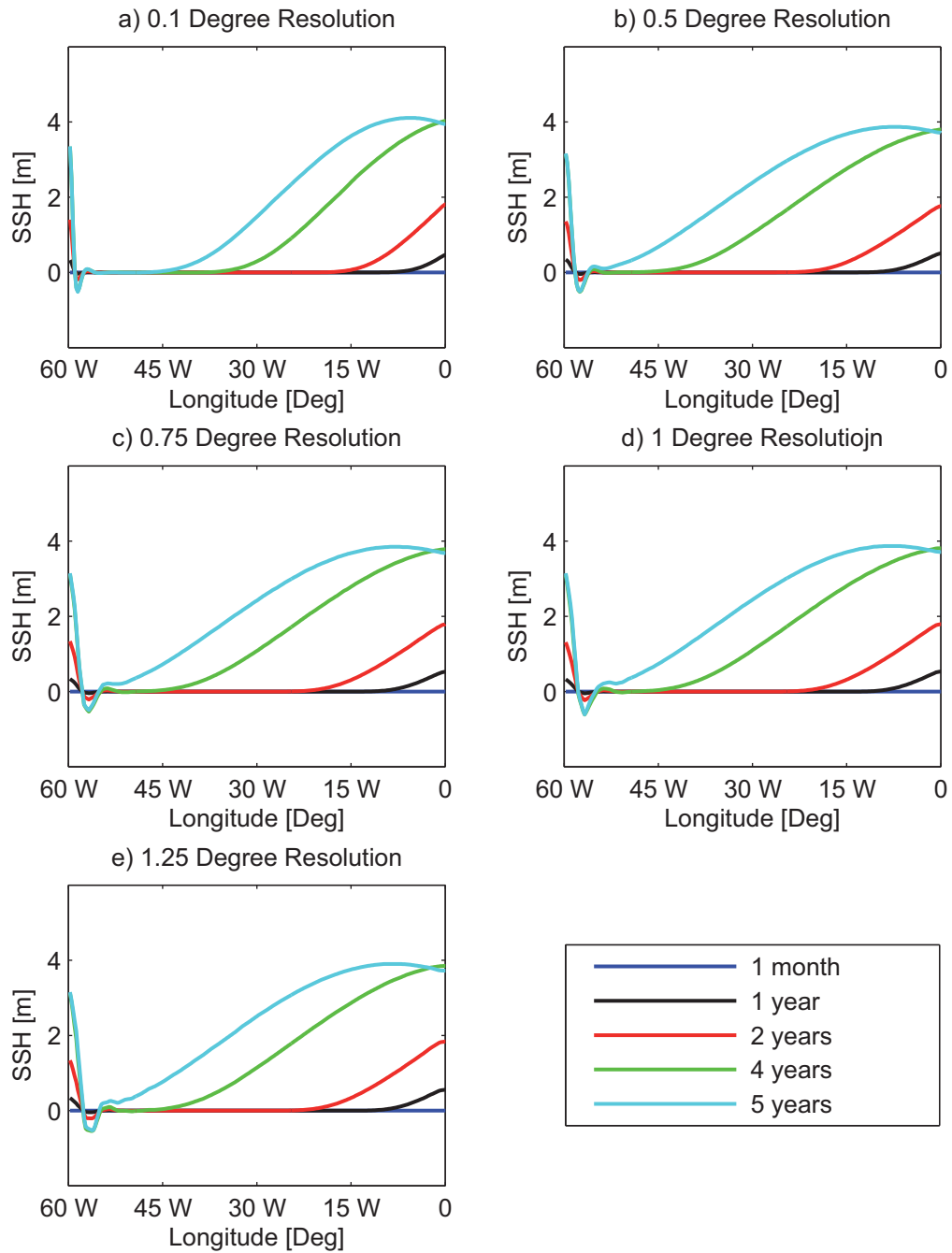


Figure 3.6: Evolution of coastal Kelvin waves and Rossby waves with time on various meshes in the 45 S. Note that there is only marginal sensitivity to resolution for the Rossby waves.

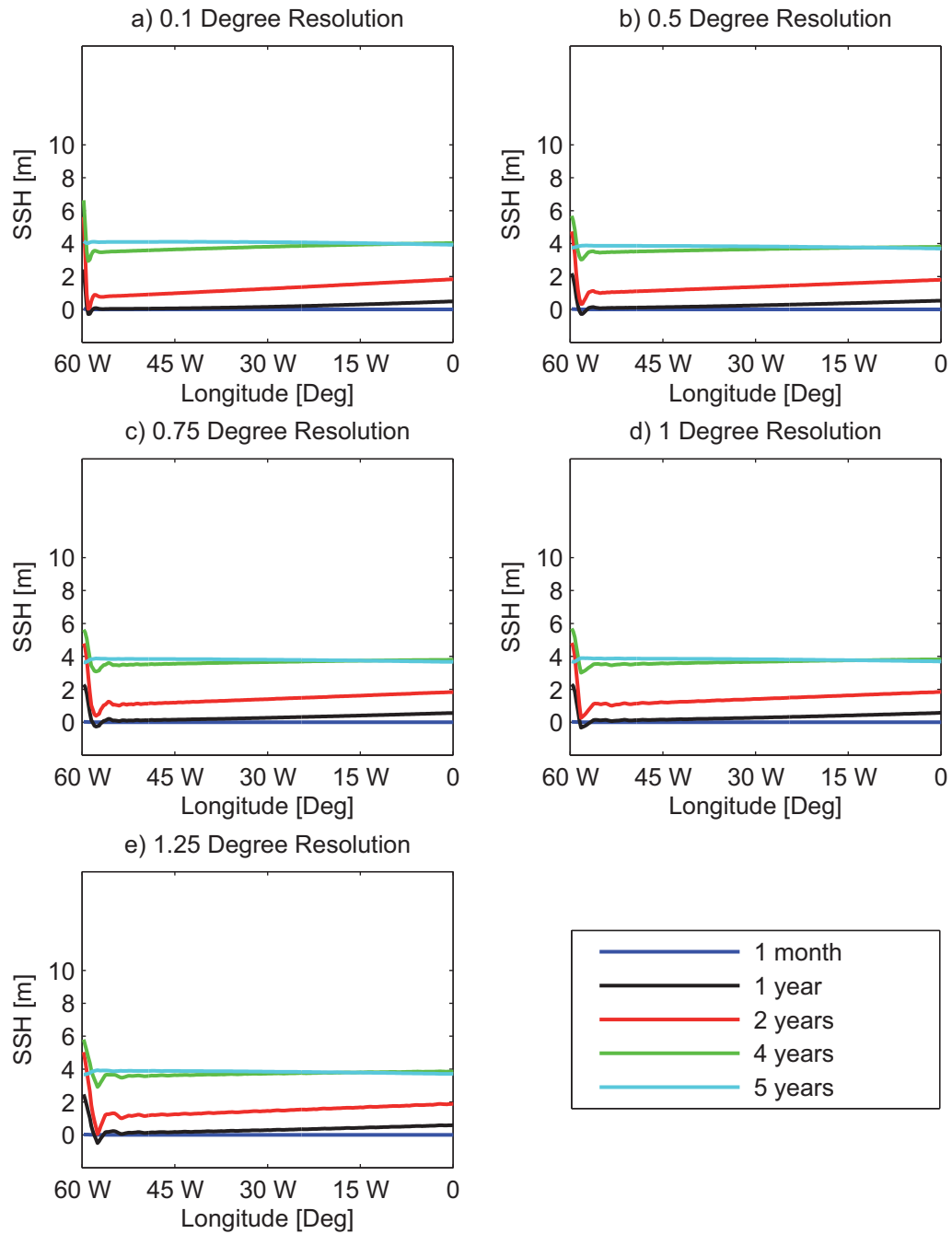


Figure 3.7: Evolution of coastal Kelvin waves and Rossby waves with time on various meshes in the 15 S. Note that there is only marginal sensitivity to resolution for the Rossby waves.

### 3.2.1 Dependence of Kelvin wave on viscosity

To understand the influence of viscosity on boundary waves, we first take a look at the behavior of coastal Kelvin waves at low frequencies. Clarke and Shi (1991) shows that as the frequency of Kelvin wave is reduced, the onshore excursions of fluid particles become progressively larger, so that finally the effect of variable planetary vorticity (beta-effect) becomes essential. Clarke and Shi (1991) derive the following dispersion relation from the shallow water equations for coastal waves (for full derivations please refer to the above mentioned article):

$$k = \frac{-i\beta}{2\omega} \pm \frac{i\beta}{2\omega} \left(1 - \frac{4f^2\omega^2}{\beta^2c^2}\right), \omega < \frac{\beta c}{f} \quad (3.23)$$

$$k = \frac{-i\beta}{2\omega} \pm \frac{f}{c} \left(1 - \frac{4f^2\omega^2}{\beta^2c^2}\right), \omega > \frac{\beta c}{f} \quad (3.24)$$

where  $k$  is the off shore wave number,  $f$  is the Coriolis parameter,  $c$  is the phase speed, upper sign corresponds to the eastern coast and the lower sign corresponds to the western coast. According to this solution, wave ceases to be trapped at sufficiently low frequency. The frequencies depend on latitude, but it can be easily seen that waves with larger than annual periods cannot be trapped at latitudes of 20 digress. At frequency is further reduced, the boundary waves transform to the short Rossby waves on the eastern coast and into long Rossby waves on the eastern coast. The long Rossby waves will not be affected very little by viscosity (as will be shown later in this section). However, as mentioned earlier, the short Rossby waves are dissipated quickly as their wavelength is short. Denoting viscosity by  $\nu$ , we estimate the dissipation time scale as  $\tau = \omega^2/\beta^2/\nu$ . Taking a period of  $N$  days, the estimate reduced to  $\tau = R_E^2/(4N^2\nu)$ , with  $R_E$  the Earth's radius, or  $\tau \approx 15$  days, for  $\nu = 100 \text{ m}^2/\text{s}$ , and a period of 3 years.

Now, in order to understand the dynamics at the coastal regions under the effect of planetary vorticity (beta effect) and in the presence of friction and viscosity, let us consider the following: The quasigeostrophic potential vorticity equation in the case with friction and vorticity will transform to:

$$p_{xxt} + \beta p_x - \frac{f^2}{c^2} p_t = -r p_{xx} + v p_{xxxx} \quad (3.25)$$

here,  $r$  is the coefficient of linear friction. In order for this equation to be valid, frictional and viscous terms should remain large compared to the inverse of the Coriolis parameter. Use of linear friction for baroclinic waves is questionable, however, we keep it in order to treat the problem in a simpler way. The analog of equation (3) from Clarke and Shi (1991) in this case will be:

$$u \approx (\partial_t - f\mathbf{k} \times)(-\nabla p - ru + v\Delta u) \quad (3.26)$$

The most important part of the frictional term in the above equation is the part that comes from the Coriolis parameter, so the boundary condition becomes approximately  $-p_{xt} - fp_y - frv + fv v_{xx} = 0$ , or on applying geostrophic approximation  $v = p_x/f$ , for meridional velocity in frictional terms:

$$-p_{xt} - fp_y - rv + v p_{xxx} = 0, \quad (3.27)$$

This equation along with equation 3.25 combine the effect of  $\beta$  and friction. Let us start with the case  $v = 0$  and  $r \neq 0$ . In this case, the characteristic equation becomes:

$$(-i\omega + r)k^2 + \beta k - i\omega L_R^{-2} = 0 \quad (3.28)$$

We non dimensionalize  $k$  with the Rossby radius  $L_R$  ( $\bar{k} = kL_R$ ) to get:

$$(-i\omega + r)\bar{k}^2 + \beta L_R \bar{k} - i\omega = 0 \quad (3.29)$$

In the absence of beta effect and dissipation, we get  $\bar{k} = \pm 1$ . In the limit of very small frequencies, it is the balance of beta term with friction which sets the scale of  $k$ :

$$\bar{k}_e = 0; \bar{k}_w = -L_R \beta / r \quad (3.30)$$

where  $e$  and  $w$  denotes the eastern and the western boundary solutions. There is no trapping at the eastern boundary. Hence we have the long westward propagating Rossby waves. At the western boundary, we recover a trapped wave, localised on the scale of boundary layer known from the Stommel gyre solution. If  $r$  is sufficiently small  $r = 0.01 \text{ day}^{-1}$ , the low frequency localisation  $\bar{k}_w \sim 4$  (for  $L_R = 30 \text{ km}$  and  $\beta = 1.5 \times 10^{-11} \text{ (ms)}^{-1}$ ). In this case, the scale of trapping is rather small, so that the account for small viscosity will necessarily modify it. For larger  $r$ ;  $r = 0.1 \text{ day}^{-1}$  (which is perhaps too large except for very shallow seas), we obtain  $\bar{k}_w \sim 0.4$ , ie. the localisation scale is 2.5 times larger than the Rossby radius. This illustrates that high dissipation manages to bring back the trapped character of propagation, and may also increase the localisation scale beyond the Rossby radius. The question now is what remains of the propagation. Substituting  $\bar{k}_w$  in the boundary condition, we get the following estimate for the eigenvalue of  $\partial_y$ :

$$k = (i\omega - r)\bar{k}/c \quad (3.31)$$

which indicates that the phase speed is modified to  $c/\bar{k}$  and there is damping as the wave propagates. The  $e$ -folding length is  $c/(r\bar{k}_e)$  in the limit of low frequencies and does not depend on  $r$ . In the example above, it is about 6500 km, so even friction that high does not exclude the propagation.

Now, let us consider the case with viscous damping,  $\nu \neq 0$ ,  $r = 0$ . In this case, the characteristic equation becomes of the 4th order and is unwieldy to analysis. However, we can consider the asymptotic solutions. The difference to the previous case is that now there are two solutions, one additional boundary condition is required to determine the alongshore propagation speed and decay rate (do no-slip conditions and free slip conditions later). The asymptotic solutions for  $\bar{k}$  are well known in the limit of very low frequencies from the theory of the viscous boundary layer in the Munk gyre. In this case,  $\bar{k}_e = 0$  and  $\bar{k}_e = L_R(\beta/\nu)^{1/3}$  at the eastern boundary and  $\bar{k}_w = (-1 \pm \sqrt{3})L_R(\beta/\nu)^{1/3}/2$ . In this case, even with relatively small viscosity of  $100 \text{ m}^2/\text{s}$ ,  $\bar{k}_w$  is less than one. It is important to note that with viscosity included, the waves remain localised along the western

boundary, and generally their localisation is broader than the Rossby radius.

Since the horizontal viscosity in ocean circulation models in the vicinity of the western coast is typically selected so as to resolve the Munk boundary layer, low-frequency localised waves propagating along the coast will be resolved too. For this reason, most models will be able to maintain the propagation of trapped waves. Although these waves decay as they propagate alongshore, they propagate sufficiently fast and manage to play a role similar to the role of a true Kelvin wave. Henceforth in this thesis, these waves will be referred to as Kelvin waves or coastally trapped Kelvin wave for the sake of simplicity.

To show the influence of horizontal viscosity on wave propagation, we performed sensitivity tests with viscosities of  $5 \text{ m}^2/\text{s}^2$ ,  $10 \text{ m}^2/\text{s}^2$ ,  $15 \text{ m}^2/\text{s}^2$ ,  $20 \text{ m}^2/\text{s}^2$ , and  $25 \text{ m}^2/\text{s}^2$ . The values of viscosity are chosen based on the dynamics and resolution, higher values do not seem appropriate for the finest resolution we used. Linear dynamics may run without viscosity in simple geometries, and would require some viscosity if the domain geometry or bottom topography becomes more involved. Since coastally trapped Kelvin waves propagate sufficiently fast ( $\sim 4.5 \text{ m/s}$  in our case), we anticipate that viscosity cannot damp them strongly unless it is extraordinary high. Assuming the Rossby radius  $L_R = 40 \text{ km}$  and viscosity  $\nu = 160 \text{ m}^2/\text{s}$ , the amplitude decrement is only  $\nu/L_R^2 = 10^{-7} \text{ s}^{-1}$ . A wave will travel 45000 km before being attenuated e-fold. This is corroborated by numerical experiments.

Figure 3.8 shows the off-shore decay structure of the coastally trapped Kelvin wave for varying viscosity at  $15^\circ \text{ N}$  on the western boundary. At  $15^\circ \text{ N}$ , the Rossby radius for a baroclinic Kelvin wave in our set up is  $\frac{\sqrt{g'H}}{f} \sim 110 \text{ km}$ . So the Rossby radius at  $15^\circ \text{ N}$  is well resolved by the fine mesh with resolution of 0.1 degree and marginally resolved by the mesh with coastal resolution of 0.5 degree. In Figure 3.8, as we move from (a) to (e), the resolution worsens, and with worsening resolution, we can see a general broadening of the off-shore decay structure of a coastally trapped Kelvin wave. The off-shore decay structure for the 0.1 degree and 0.5 degree mesh is within the limit of the Rossby radius. However, for each resolution, there is a very slight broadening of the off-

shore structure due to increase in viscosity. At  $45^\circ$  N, the Rossby radius for a baroclinic wave is  $\frac{\sqrt{g'H}}{f} \sim 50$  km, so the fine resolution mesh with a resolution of 0.1 degree is the only mesh that resolves Rossby radius at mid and high latitudes. Figure 3.9 shows the off-shore decay structure of the coastally trapped Kelvin wave for varying viscosity at  $45^\circ$  N on the western boundary. As in the case of  $15^\circ$  N, we see that as the resolution worsens, off-shore decay structure of a coastally trapped Kelvin wave broadens. However, the broadening due to change in viscosity is relatively small.

As the Coriolis parameter decreases with latitude, the amplitude of the anomaly should also decrease as it moves towards the equator. Figure 3.10 shows the decay of the amplitude of the coastally trapped Kelvin wave as it propagates along the western boundary from  $55^\circ$  N to the equator for various viscosities and resolution. As mentioned earlier, the perturbation is applied at  $57.5^\circ$  N with a width of  $\sim 2$  degrees, so we show the propagation of the anomaly from  $55^\circ$  N. As we can see, within a reasonable range of viscosity, the decay structure of the amplitude of the coastally trapped Kelvin wave does not vary significantly. Figure 3.10 (b-e) shows the decay structure of the coastally trapped Kelvin wave along the same path for the coarser meshes. Comparing Figures 3.10 (a) to (e), it is clear that viscosity does not have a noticeable influence on the amplitude decay of the coastal Kelvin wave on either high or low resolution triangular grids. There is a remarkable agreement in the amplitude of the signal reaching the equator in the fine and the coarse mesh. The amplitude decay of the coastally trapped Kelvin wave along the western boundary agrees with the theory proposed by (Johnson and Marshall, 2002). However, oscillations appear to increase with worsening resolution due to insufficient viscosity.

Along the eastern boundary, a geostrophically-balanced meridional pressure gradient cannot be maintained since to balance it, a Coriolis force would require a velocity across the coastline. Figure 3.11 shows the amplitude of the signal along the eastern boundary from the equator to  $60^\circ$  N on meshes with various resolution. As predicted by Johnson and Marshall (2002), the signal amplitude along the eastern boundary is uniform in latitude. The varying viscosity does not have a severe impact on the amplitude of the wave

propagating along the eastern boundary. However, we can see that low viscosity on coarse resolution meshes leads to noise in the higher latitudes, and the noise reduces as viscosity increases. The phase speed of the coastally trapped Kelvin wave stays constant with varying viscosity in the fine mesh. In the coarse mesh, for low viscosity ( $5 \text{ m}^2/\text{s}$ ) the phase speed is  $3.97 \text{ m/s}$  and for high viscosity ( $25 \text{ m}^2/\text{s}$ ), the phase speed is  $3.99 \text{ m/s}$ . Still this speed is lower than the theoretical estimate, which can be linked to effects of stabilization.

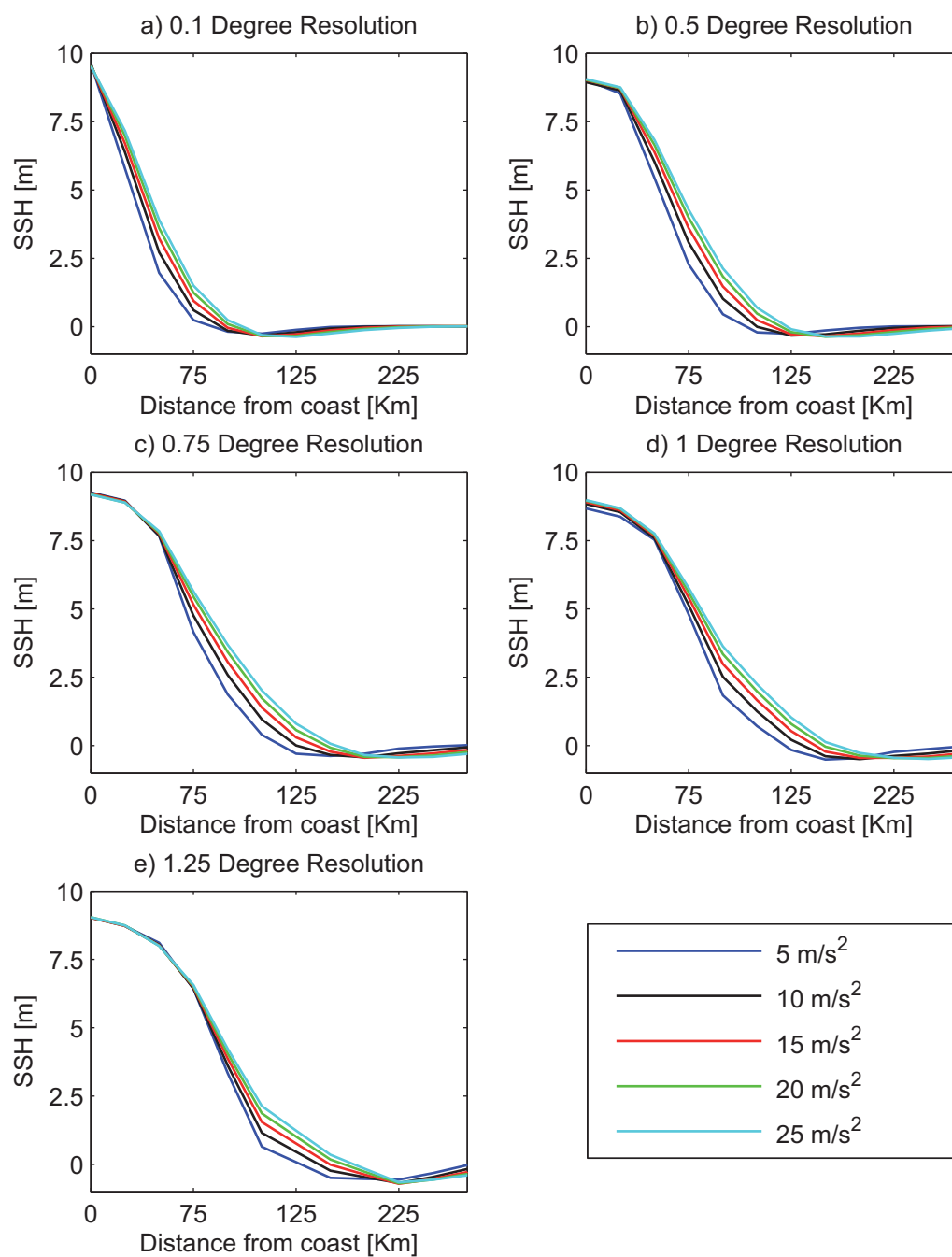


Figure 3.8: Off shore decay of the coastally trapped Kelvin wave amplitude for varying viscosity at 45 N

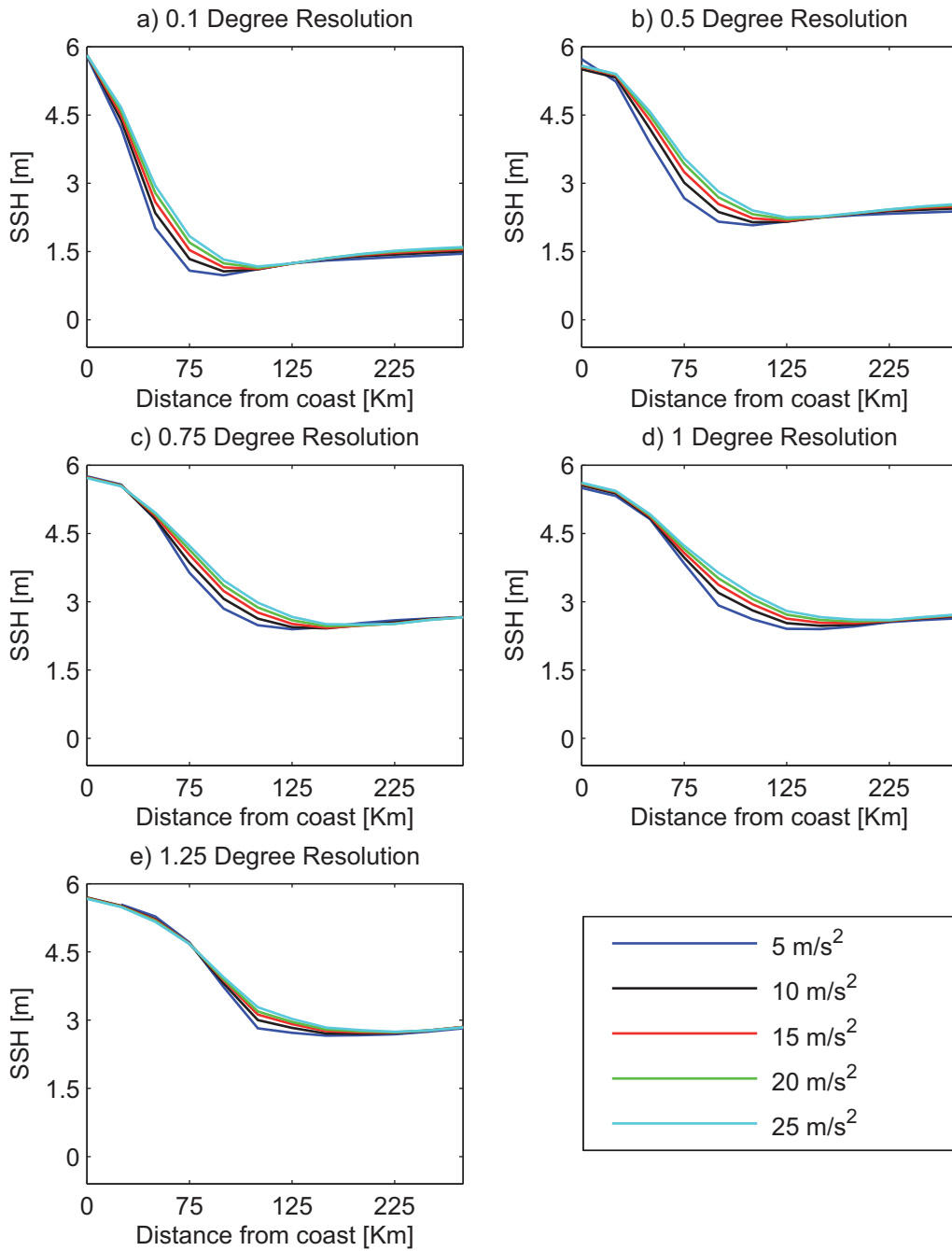


Figure 3.9: Off shore decay of the coastally trapped Kelvin wave amplitude for varying viscosity at  $15^\circ$  N. Arrival of westward propagating Rossby waves front can be seen 125 - 200 km off the coast.

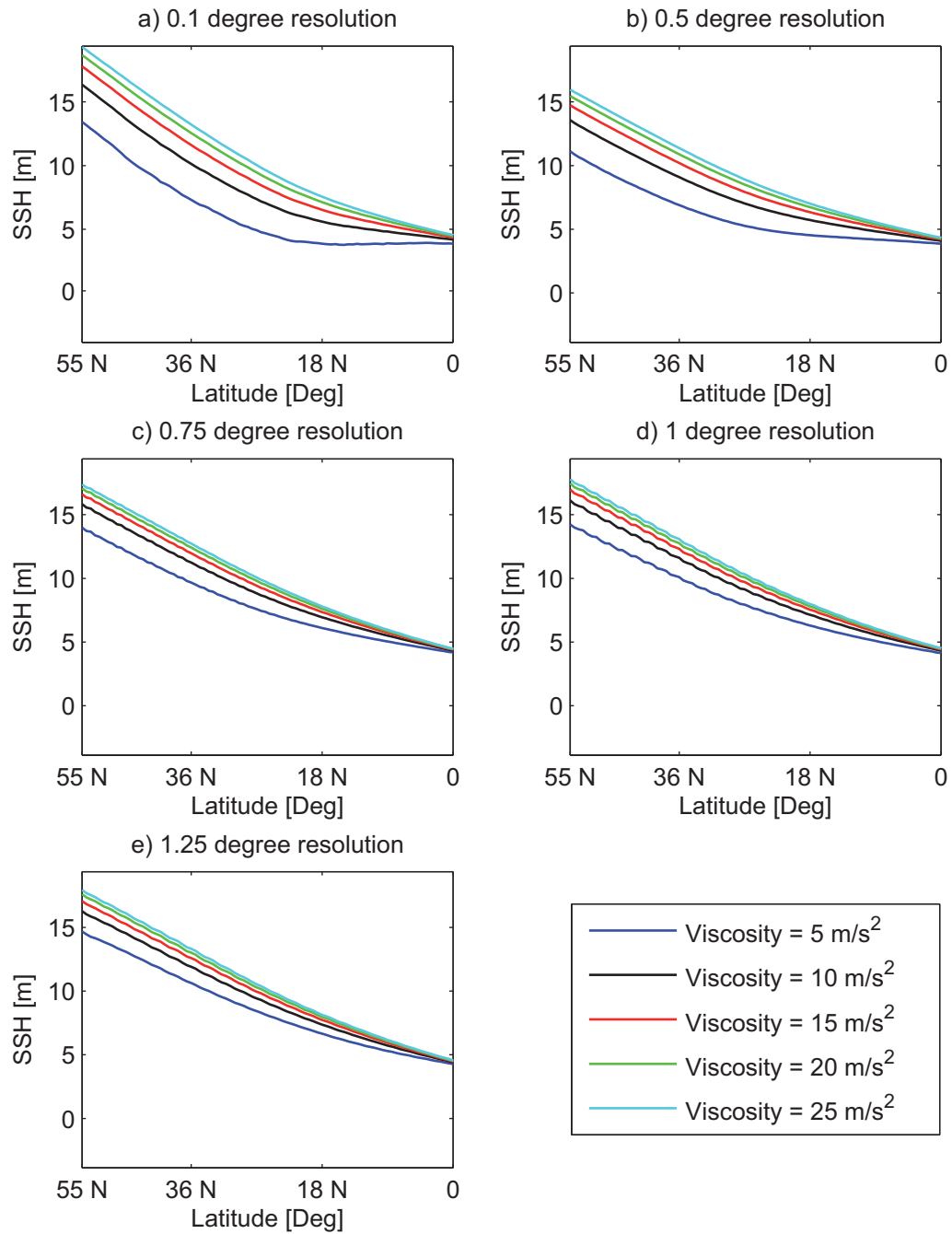


Figure 3.10: Amplitude of the waves as it propagates along the western boundary from the north-west corner of the domain to the equator in various meshes. Insufficient viscosity on the coarse meshes leads to oscillations.

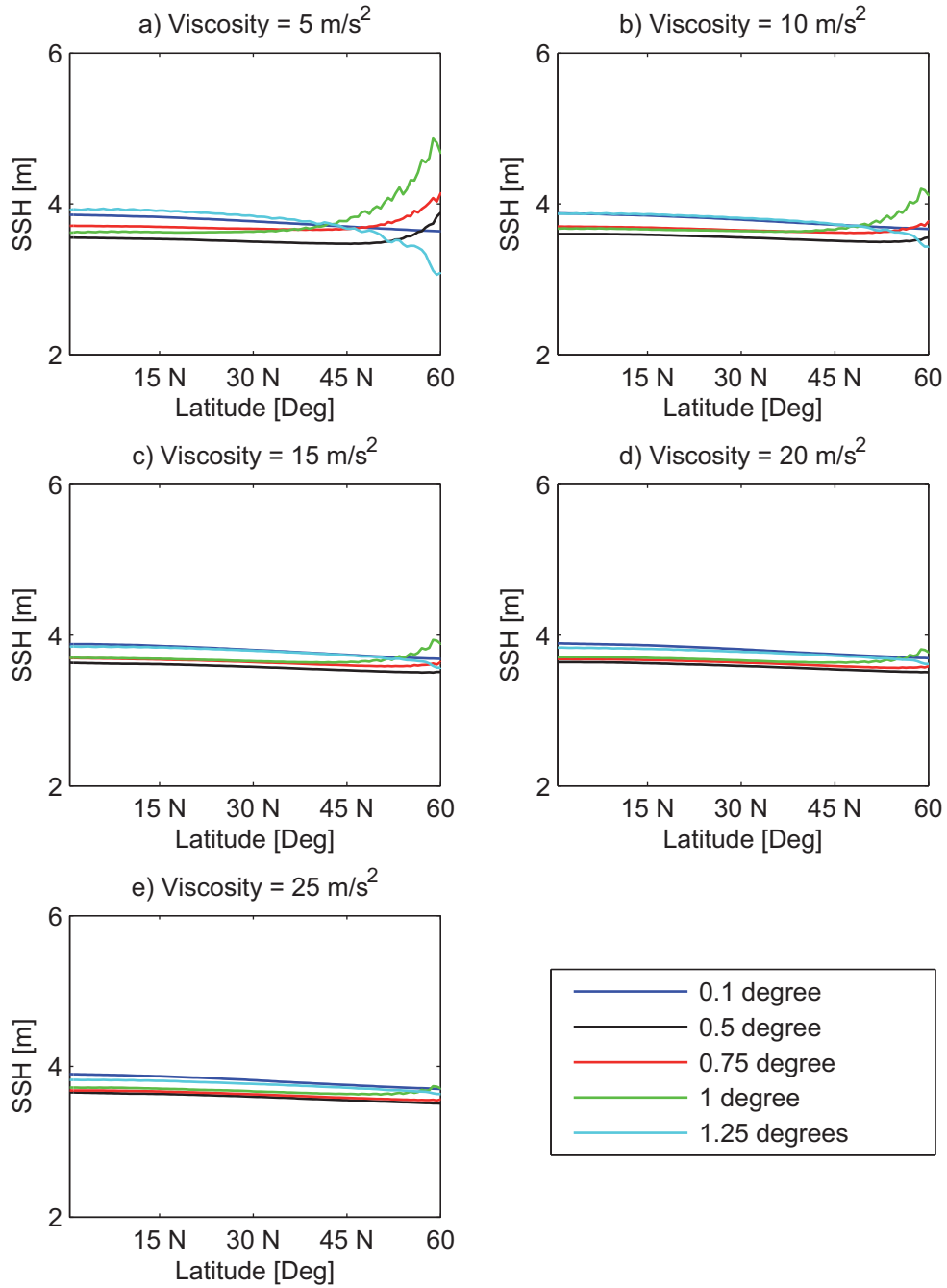


Figure 3.11: Amplitude of the waves as it propagates along the eastern boundary from the north-east corner of the domain to the equator in various meshes. Insufficient viscosity on the course meshes leads to oscillations.

### 3.2.2 Dependence of Kelvin wave on mesh resolution

According to equation 3.15 and 3.16, once the Rossby radius is resolved, the model should be able to simulate the coastally trapped Kelvin wave. In Figure 3.12, we see the off-shore decay structure of a coastally trapped Kelvin wave on the western boundary at  $45^\circ$  N for various resolutions and for various viscosities. At  $45^\circ$  N, the Rossby radius on our set-up is  $\sim 50$  Km. The coastal resolution of the fine mesh is  $\sim 7$  km. So the fine mesh is resolving at the Rossby radius at  $45^\circ$  N. We can see that on the fine mesh, the coastally trapped Kelvin wave decays until the Rossby radius. However, as the resolution of the mesh worsens, the decay structure broadens. On the coarse mesh with resolution of 1.25 degrees, the coastally trapped Kelvin wave decays upto 125 km off-shore. Once the resolution is lower than the Rossby radius, i.e. the distance between two grid points is longer than the Rossby radius, the off-shore decay of the coastally trapped Kelvin wave widens and the widening is governed by equations 3.15 and 3.16. Table 1 shows the widening of the off-shore decay structure of a coastally trapped Kelvin wave for certain common grid sizes. We see that when the resolution is 4 times more than the Rossby radius, the off-shore decay width of the coastally trapped Kelvin wave is less than two times more than the Rossby radius. The spread of the off-shore decay is not significantly high as the resolution worsens.

$\Delta$	$L'/L$	Resolution at $40^\circ$ N
<1	1	7 km
1.7	1.4	50 km
2.5	1.5	75 km
3.3	1.75	100 km
4.1	1.94	125 km

Table 1: Off shore spread of Kelvin wave with worsening resolution in FEOM

Figures 3.10 and 3.14 show how the amplitude of the coastally trapped Kelvin wave varies with varying resolution and viscosity respectively, along the western coast. As dis-

cussed in the previous section, the amplitude is expected to decrease due to the decrease of Coriolis parameter with latitude, and dissipation. However, the amplitude of the signal reaching the equator is remarkably similar in various resolution and viscosity. Figure 3.13 shows how the off-shore decay structure of the coastally trapped Kelvin wave looks like at lower latitudes. At  $15^\circ$  N, the Rossby radius of deformation is  $\sim 110$  km. Again, we see that with worsening resolution, the decay structure broadens. The theoretical phase speed of Rossby wave at  $15^\circ$  N is  $\sim 29$  cm/s. At  $15^\circ$  N, Rossby wave takes approximately 9 months to travel  $60^\circ$  of longitudes. In Figure 3.13, we can see the arrival of the front of the westward propagating Rossby wave at 125 - 200 km off the coast.

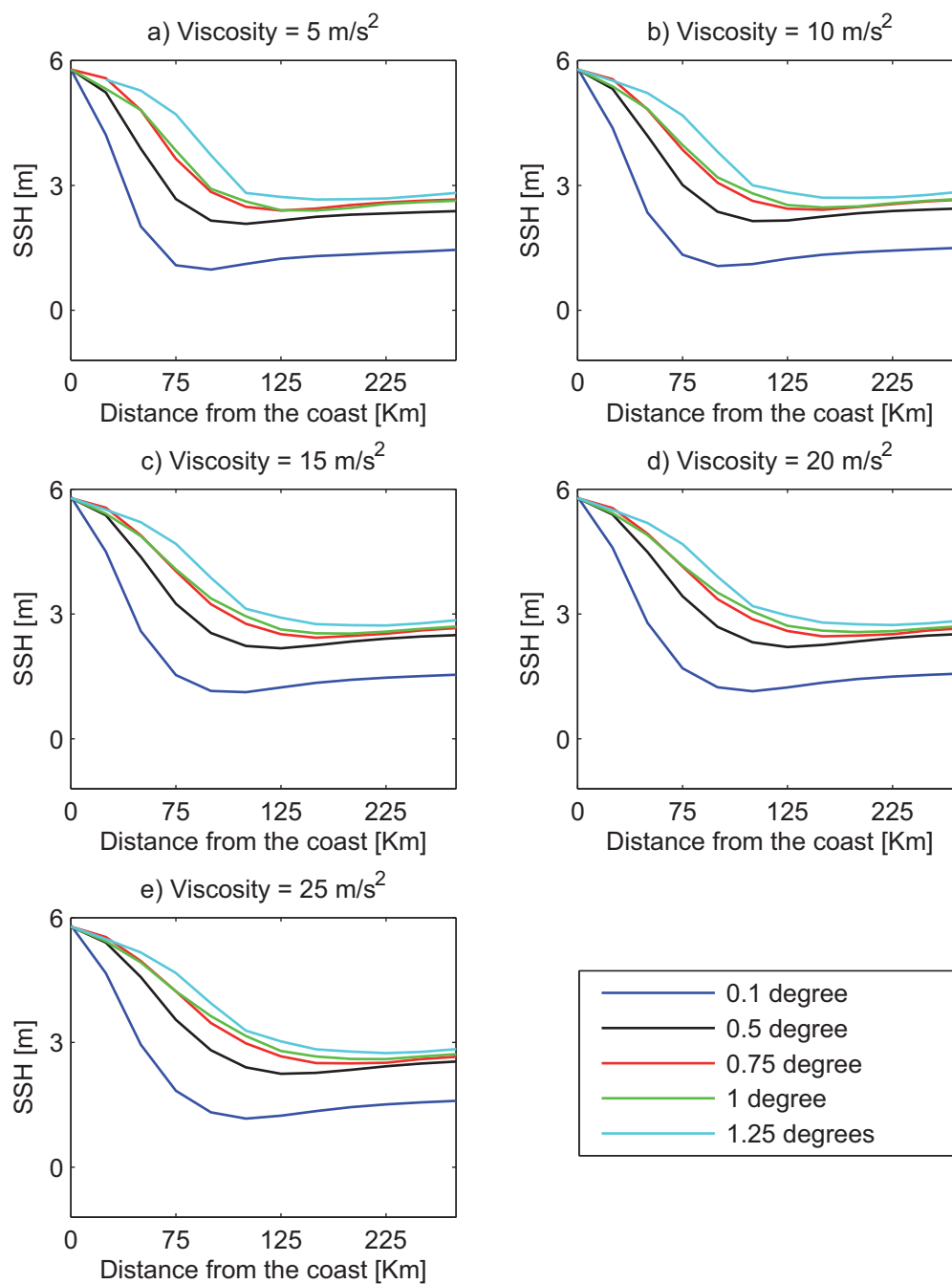


Figure 3.12: Off shore decay of the coastally trapped Kelvin wave amplitude for varying resolution at 45° N

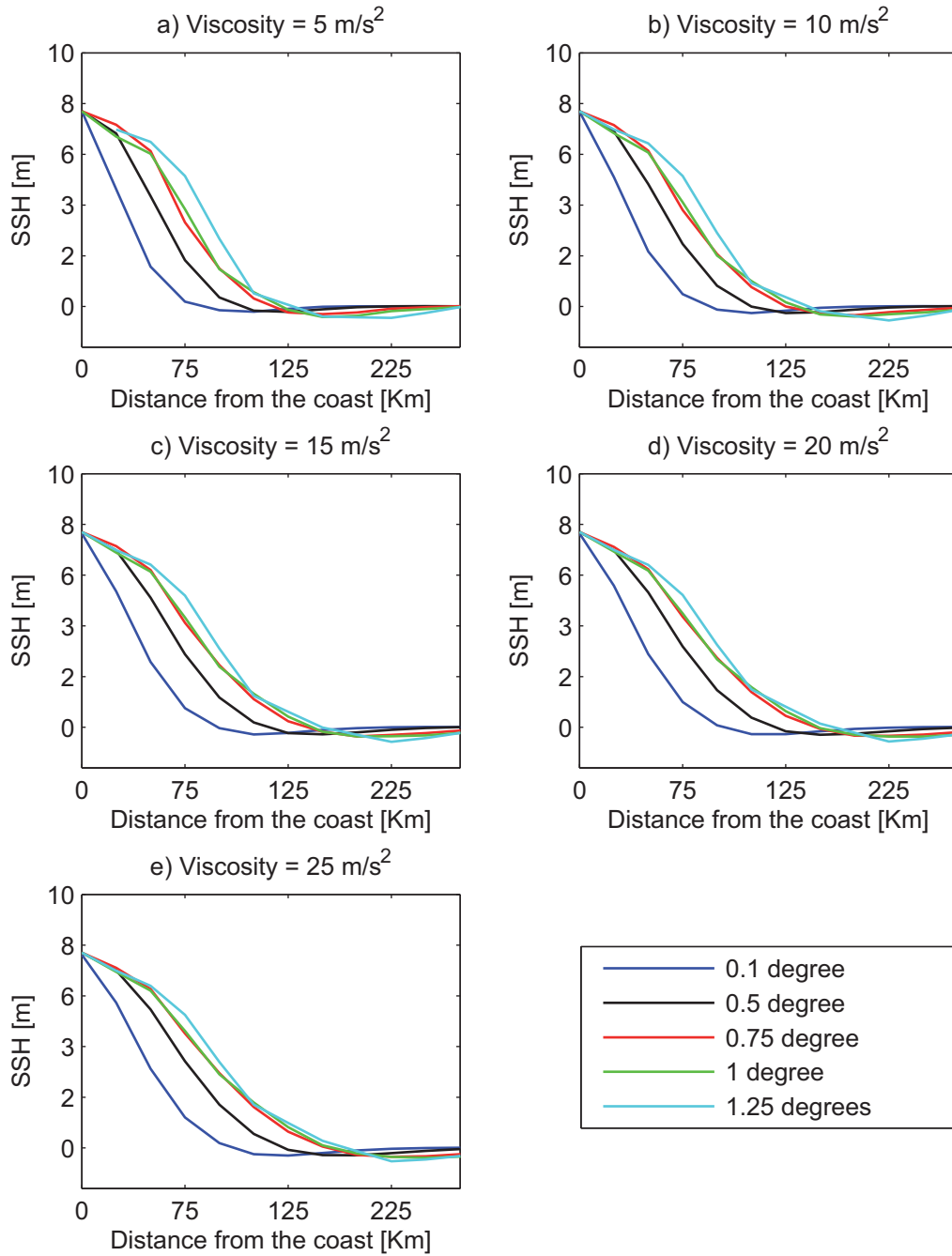


Figure 3.13: Off shore decay of the coastally trapped Kelvin wave amplitude for varying resolution at  $15^\circ \text{ N}$ . Arrival of westward propagating Rossby waves front can be seen 125 - 200 km off the coast.

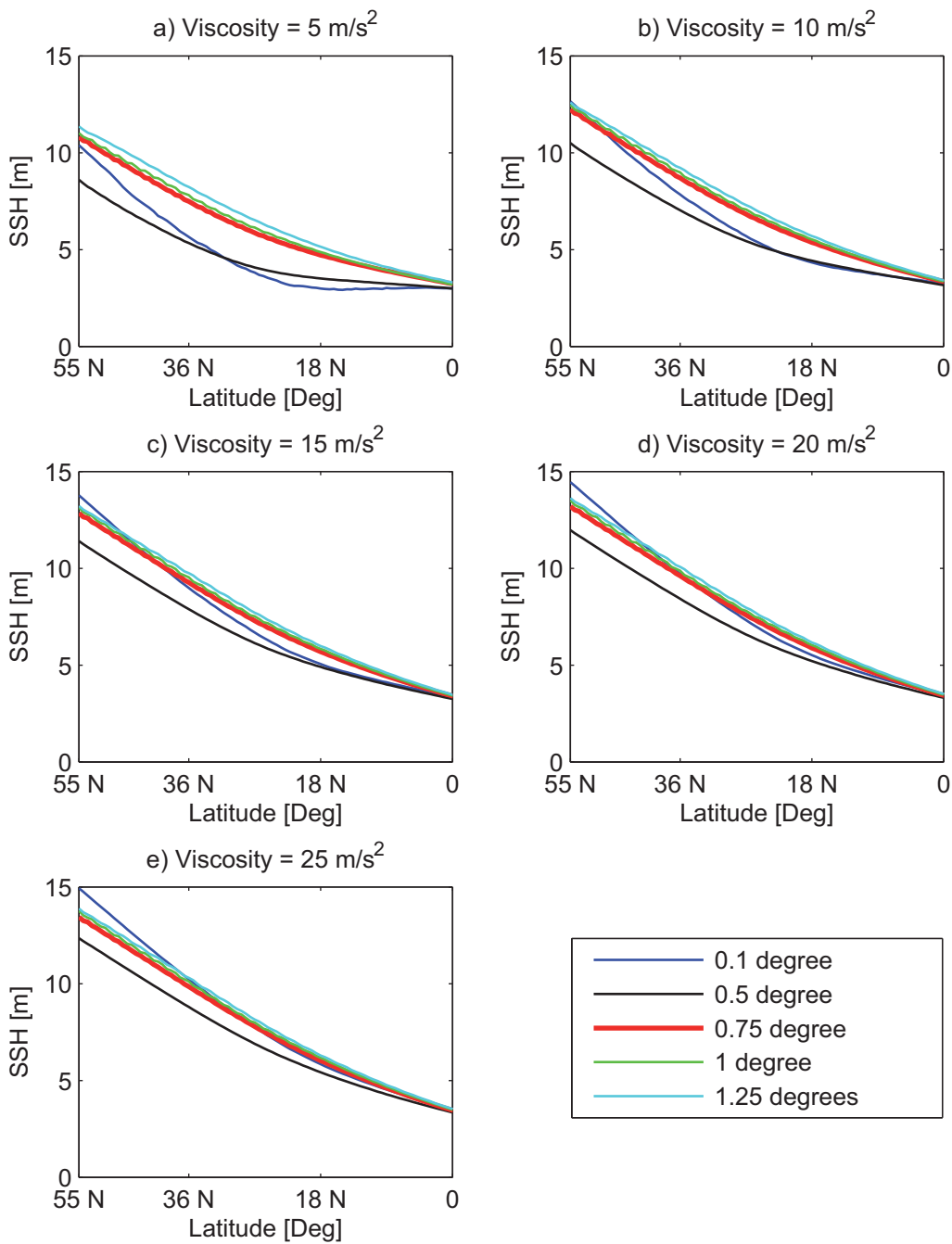


Figure 3.14: Amplitude of the waves as it propagates along the western boundary from the north-west corner of the domain to the equator in various meshes

### 3.3 Discussion

The primary aim of this chapter was to determine whether triangular grids are a suitable tool to study boundary wave dynamics. Towards achieving this goal, we analytically studied the behavior of Kelvin waves on triangular grids. Thereafter the characteristics of a Kelvin wave in a  $P_1 - P_1$  finite-element shallow water model under varying mesh resolution and viscosity has been studied through a series of numerical simulations. This discretization serves a basis of several models, including FESOM. Coastally trapped Kelvin waves play an important role in the initial adjustment to high-latitude perturbations. To simulate this initial adjustment, and the impact of the wave adjustment on large scale ocean circulation through ocean modeling, one needs to resolve these waves in order to properly simulate their phase speed and off-shore decay characteristics.

Our analytical study shows that on uniform triangular meshes, we find the theoretical prediction of Kelvin wave phase speed,  $c_p = 1$  if consistent mass matrices are used. With lumped mass matrices, the wave propagates faster on coarse meshes than the theoretical limit, similar to the B-grid case of Hsieh et al. (1983). The phase speed of Kelvin waves in numerical simulations supports our analytical results, being almost independent on resolution. There is some discrepancy between the measured and predicted speed, which is by all probability is due to the stabilization. Previous studies, using finite-difference numerical models, have shown that the phase speed and the waveguides of the baroclinic Kelvin wave depends dramatically on the discretisation method used by Hsieh et al. (1983). The waveguide structure is better represented by a B-grid than a C-grid, as grid scale oscillations occur for a C-grid as the resolution worsens. On the other side, the phase speed of the Kelvin wave increases dramatically on B-grids as the resolution worsens, in contrast to C-grids where the phase speed remains constant under varying resolution. The case considered by us maintains both the structure and the phase speed.

In the limit when Rossby radius is resolved, i.e.  $\Delta < 1$ , the  $P_1 - P_1$  model used here produces the classical Kelvin wave, with an off-shore decay resembling the theoretical Kelvin wave guide. In the limit when  $\Delta > 1$ , i.e. the Rossby radius along the coast is

not resolved, the Kelvin waveguide broadens. However, the structure is stable and the amplitude of the signal reaching the eastern equator is not significantly affected by the low resolution. In our simulations, the lowest resolution is 1.25 degrees along the coast ( $\sim$  four times the Rossby radius at high latitudes in our set up) and the highest resolution is 7 km along the coast. While comparing the two cases, we find that the amplitude of the signal reaching the equator and the eastern equator is not significantly different. Our results suggest that the finite-element  $P_1 - P_1$  discretization is suitable for simulations of processes involving Kelvin and Rossby wave propagation.

We also found that at low frequencies, the boundary waves cease to be trapped and as the frequency is further lowered, they transform into short Rossby waves on the western coast and long Rossby waves on the eastern coast. Long Rossby waves are affected by viscosity very little.

In the presence of viscosity and the beta effect, trapping along the western boundary is again recovered. Propagation along the western boundary is still maintained through these modified boundary waves. Since the horizontal viscosity in ocean circulation models in the vicinity of western coast is typically selected so as to resolve the Munk boundary layer, low-frequency localised waves propagating along the coast will be resolved too. For this reason most models are able to maintain propagation of trapped waves. Although these waves decay as they propagate alongshore, they propagate sufficiently fast and manage to play a role similar to the role of true Kelvin waves.

Keeping the above findings in mind, we can beneficially use triangular grids to further study the role of boundary waves in ocean teleconnections. In the next chapters, we study how ocean responds to buoyancy forcing in the northern latitudes and wind forcing via wave adjustment through modeling studies on triangular grids.



## **Chapter 4**

# **Dependence of oceanic wave adjustment on frequency of variability and topography**

In this chapter, a numerical ocean circulation model has been used to address the question of dependence of global wave adjustment in the presence of background wind driven circulation and realistic bottom topography, to the frequency of buoyancy forcing at high latitudes of the North Atlantic Ocean. The model used, BarBI, allows dynamics of barotropic and baroclinic waves in the presence of topography and circulation. The results from BarBI are compared with experiments performed on a reduced gravity setup. A complete description of BarBI and the setup can be found in Chapter 2. In section 4.2, we point to the differences in the time scales and pattern of wave adjustment in a BarBI setup with and without any background circulation.

Section 4.1 compares the coastally trapped wave propagation between a coarse resolution and a fine resolution model. It illustrates the propagation of coastally trapped waves while they pass through certain topographic features, like the Caribbean islands and the Gulf of Mexico, by resolving them on a high resolution triangular mesh. In section 4.2, time-scales and pathways of global wave adjustment due to buoyancy forcing

with a white noise spectrum at the North Atlantic are studied through a series of numerical simulations. The response spectra of different ocean basins are analysed based on barotropic and baroclinic dynamics. The results from a reduced gravity setup are compared to the results of the separate barotropic and baroclinic flow in BarBI. Section 4.3 concludes with a summary of the results.

## 4.1 Dependence of tropical response on the frequency of high latitude perturbation

### 4.1.1 Set-up of experiments

To test the dependence of the tropical response due to perturbation in the rate of deep water formation caused by northward outflow and by waves on wave pathways and frequency of perturbation, the linear shallow water model with element-wise linear  $P_1 - P_1$  representation of variables (as in FESOM) under reduced gravity setup, as described in Chapter 2, Section 2.2.1.2 has been used. A mesh of the North Atlantic ( $80^\circ N - 20^\circ S$ ) with unstructured triangular elements is used. The horizontal grid resolution is set to 5 km near the coast, 20 km at the equator and  $\sim 100$  km at the mid-latitude interior ocean.

A perturbation is generated according to equation 2.6 and is centered at the Labrador Sea. The experiment was performed thrice, and the perturbation was forced with sine function, with a period of  $A(t) = 2$  years,  $A(t) = 5$  years and  $A(t) = 10$  years. For the case considered here, Johnson and Marshall (2002) pointed out that the equator acts as a low pass filter to high latitude anomalies, and part of our motivation is to illustrate this. Figure 2.5 a) shows the mesh used and Figure 2.5 b) shows a magnified part of the mesh of the Gulf of Mexico region, to illustrate the resolution of the mesh near the coast and equator.

To test the sensitivity of the wave response to coastline geometry, a mesh of the North Atlantic without the Gulf of Mexico has been generated. The region of Gulf of Mexico, that has been removed, is shown in Figure 2.5 c). The coastal and equatorial resolution of

the new mesh is same as above (5 km at the coast, 20 km at the equator and 100 km at the mid-latitude interior ocean). A coarse mesh with a resolution of 1.5 degrees in the entire domain is created.

Background flow driven by wind forcing and thermohaline forcing is not included in the setup because the main focus of this work is on the coastal and equatorial waves, determine the wave pathways through which oceanic adjustment takes place for time scale of a few decades, and show the sensitivity of these waves to the frequency of the perturbation source and topography of the ocean.

#### 4.1.2 Tropical response to high latitude forcing

In Figure 4.1, we see how the coastally trapped wave is spread across the Atlantic Ocean on the fine mesh of the North Atlantic Ocean once the forcing is switched on. After being initiated at the Labrador Sea, coastally trapped wave propagates along the western coast of the Atlantic Ocean towards the equator (Figure 4.1 a). On a reduced gravity set-up, bottom topography does not play a role. The wave enters the Gulf of Mexico between Florida and the Caribbean islands. It can be seen there is trapping of signal at the Gulf of Mexico (Figure 4.1 c).

The initial coastal wave signal reaches the equator in 2-3 months. After reaching the equator, the coastal wave continues eastward as an equatorial Kelvin wave. The equatorial Kelvin wave crosses the equator in a couple of months and reaches the African coast. Upon reaching the African coast, the equatorial Kelvin wave splits and propagate towards the pole.s The thermocline displacement along the eastern coast of Atlantic Ocean is spread into the interior of the ocean as westward propagating Rossby waves.

The amplitude of the wave (thermocline displacement) decays as it propagates from the source at the Labrador Sea to the equator, along the western boundary. A comparison between the amplitudes of the thermocline displacement at the eastern coast north of the equator (10N 1 W) in the three meshes is shown in Figure 4.2 a). The period of perturbation in this case is 5 years. The wave pathway changes on the mesh without

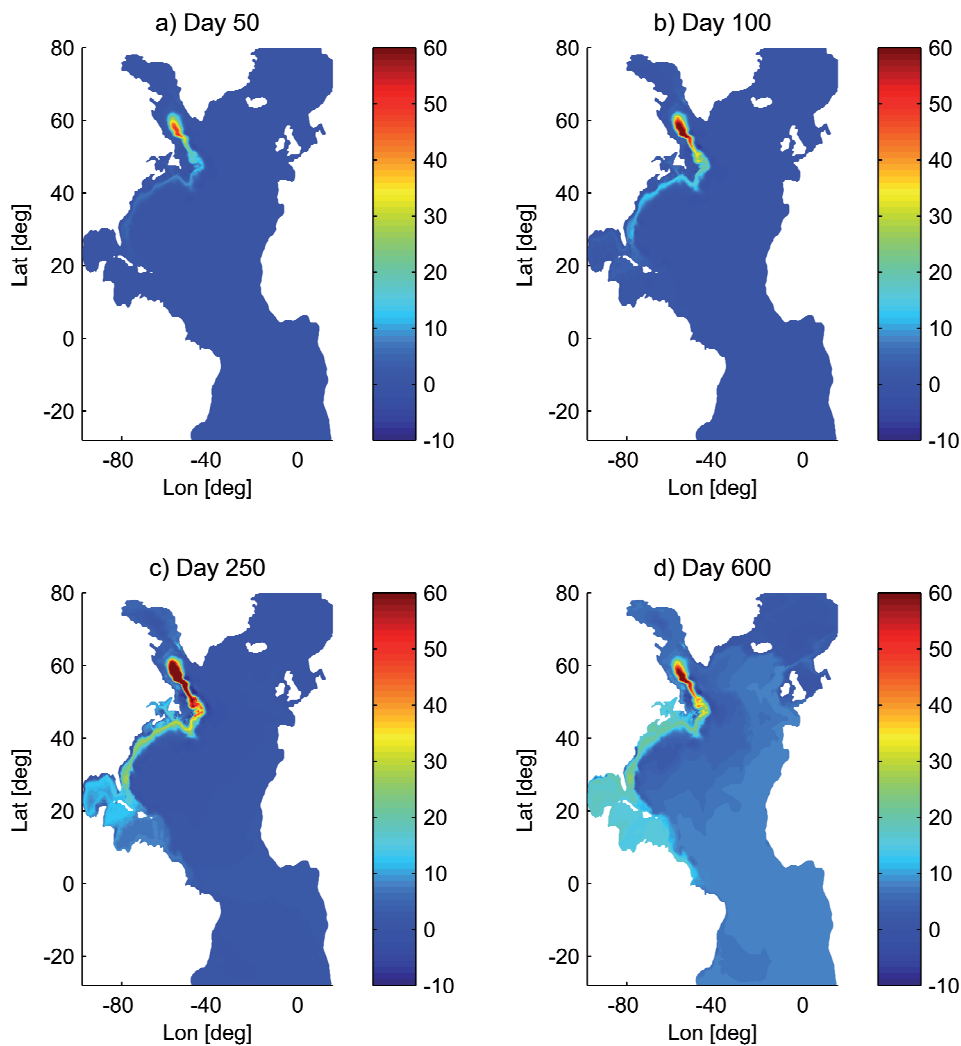


Figure 4.1: Time evolution of the wave adjustment in the North Atlantic after the perturbation of thermohaline is switched on in the Labrador Sea. Wave propagates as a thermocline displacement, with unit of meters.

Gulf of Mexico. The trapping of the wave, as seen in Figure 4.1 c) dampens the tropical response. The amplitude of the thermocline displacement arriving at the equatorial zone is marginally larger for the mesh without the Gulf of Mexico than for the North Atlantic mesh with the Caribbean islands and the Gulf of Mexico. The tropical response is less for the coarse mesh due to higher dissipation.

The tropical amplitude of the anomaly as a function of frequency of forcing is shown in Figure 4.2 b). The amplitude of forcing applied at the Labrador Sea was the same in all

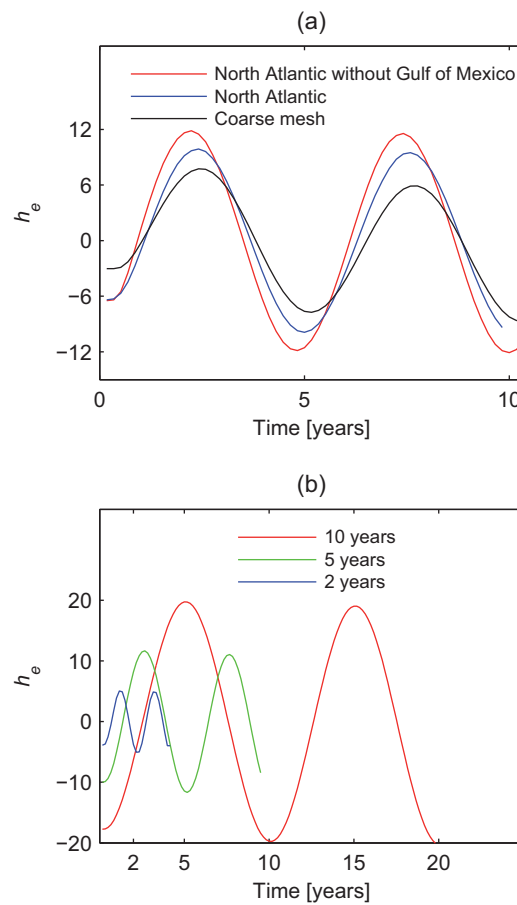


Figure 4.2: a) Amplitude of thermocline's displacement at the eastern coast  $10^\circ$  north of the equator for the three different mesh. b) Amplitude of the thermocline displacements at the eastern coast  $10^\circ$  north of the equator for perturbation of different frequencies

three cases, however there is a significant difference in the tropical response. The lower the frequency of the forcing, the higher the amplitude of the thermocline displacement at the equator is. The figure compares the amplitude for three different periods, 2 years, 5 years, and 10 years. For all three periods, the experiments are performed on the fine mesh of the North Atlantic. These results agree with the theory proposed by Johnson and Marshall (2004), that the equator acts as a low pass filter. A detailed explanation and interpretation of this result will be given in Section 4.2.2.4

## 4.2 Global wave adjustment to high latitude white noise forcing

### 4.2.1 Setup of the 3 experiments

To study the global oceanic response through wave adjustment due to variations in deep water formation rates at the high latitudes of North Atlantic ocean, two models based on simplified physics have been used. A global ocean grid, with structured triangular mesh was used to run all the experiments. The horizontal resolution was 1.5 degrees in both directions. Section 2.2.1 describes the linear shallow water model with reduced gravity setup and section 2.2.2 describes BarBI.

The *reduced gravity* setup has no background flow. Two different setups of BarBI are used. The first setup is, as described in section 2.2.2, without any background flow, henceforth referred to as “*no spin-up*” setup. The second setup of BarBI is with a background circulation driven by annual mean wind stress, as described in section 2.2.2.2, henceforth referred to as “*with spin-up*” setup. A perturbation is generated in all three setups by switching on the sources mimicking the fluctuations of deep water formation in the Labrador Sea. After switching on the sources, its amplitude varies with time as a white noise. The experiment is run for 500 years.

### 4.2.2 Results

The following section examines the spectra of the response in thermocline displacement in the different ocean basins in all three experiments. The next three sections look at the wave propagation patterns in the three setups. The fifth section analyses the differences in amplitude of thermocline displacement in the three experiments. The sixth section identifies the differences in the time scales of adjustment in the setups considered here.

**4.2.2.1 Global oceanic wave adjustment as a function of frequency of forcing**

To understand the response of the ocean in terms of thermocline thickness perturbation at the eastern boundary  $h_e$ , as a function of frequency of buoyancy forcing at the North Atlantic Ocean, we briefly recapitulate the theory developed by Johnson and Marshall (2002). In the following, a brief derivation of an expression that relates the response in thermocline thickness  $h$  to prescribed anomaly in transport  $T_N$  will be described. A detailed derivation and numerical analysis can be found in Johnson and Marshall (2002). We begin with the shallow water equations:

$$u_t + f\mathbf{k} \times \mathbf{u} = -c^2 \nabla h \quad (4.1)$$

$$h_t + \nabla \cdot \mathbf{u} = 0 \quad (4.2)$$

where  $\mathbf{u}$  is the transport velocity,  $c^2 = g'H$ , the phase speed given by the product of reduced gravity and the thermocline thickness. Let us consider an Atlantic like basin with an open boundary to the Southern Ocean. Let  $T_N$  be the prescribed transport through the North Western boundary while  $T_S$  is the transport through the Southern boundary. Integrating the continuity equation 4.2, we have:

$$T_N - T_S = \int h_t dS \quad (4.3)$$

As mentioned above,  $T_N$  is prescribed, which leads to changes in the thermocline thickness at the eastern boundary. Equilibrium in the basin is reached when the magnitude of  $T_S$  reaches the magnitude of  $T_N$ . Let us assume that the  $h$  varies due the long Rossby waves propagating from the eastern coast:

$$h(x, y, t) = h_e(t - x/C(y)) \quad (4.4)$$

where  $C = \beta L_R^2$  is the phase speed of the long baroclinic Rossby waves,  $L_R$  is the Rossby radius of deformation. This expression for  $C$  is only valid at the mid-latitudes and has to

be updated for the equatorial belt. As  $\int h_t dS = -\int C h_x dS = \int (h_e(t - x/C) - h_e(t)) C dy$ , the balance above becomes:

$$T_N - T_S = \int_S^N (h_e(t - L_x/C) - h_e(t)) C dy \quad (4.5)$$

$T_N$  is prescribed, and we express  $T_S$  as  $c^2 h_e / f_S$ . We assume that southeast corner has a thermocline thickness perturbation of  $h_e$  and the thermocline thickness perturbation at the southwest corner is zero. We simplify further by specifying  $T_N = T e^{-i\omega t}$ ,  $h_e = h e^{-i\omega t}$ , which leads to:

$$h = \frac{T}{c^2 / f_S + \int_S^N C (e^{i\omega L_x / C} - 1) dy} \quad (4.6)$$

With this formula, one can estimate the transport at any latitude by taking an arbitrary latitude instead of the southern end of the basin  $S$ . In the limit of extremely low frequencies, when the argument in the exponent is small (for periods in excess of 10 years for the North Atlantic), the above expression can be re-written as:

$$h = \frac{T}{c^2 / f_S + \int_S^N i\omega L_x dy} \quad (4.7)$$

The above expression tells us that as the frequency decreases,  $h$  goes on increasing to a constant value for very low frequencies. This asymptotic value is reached with  $T_N = T_S = c^2 h_e / f_S$ . The second term in the denominator is larger than the first in absolute value if  $\omega > c^2 / f_S / A$ , where  $A$  is the area of the domain, or the period  $T$  smaller than  $2\pi f_S A / c^2$ , which is about  $10^{10} s$  for  $A = 10^{14} m^2$ . This means that  $h$  will be inversely related to frequency until frequencies are really low with periods of 100 years or larger.

Figure 4.3 a) compares the power spectra of potential energy (PE) calculated from the equivalent thermocline depth  $h_e$  ( $PE = g \int \rho_o h_e^2 dS$ ,  $S$  is the surface area), in the Atlantic, Indian and Pacific Ocean, in the *reduced gravity* experiment. We calculate and analyse the PE in the *reduced gravity* case in order to be on equivalent footing with the analysis of PE in the BarBI case. The slopes for the Atlantic and Pacific spectra are calculated

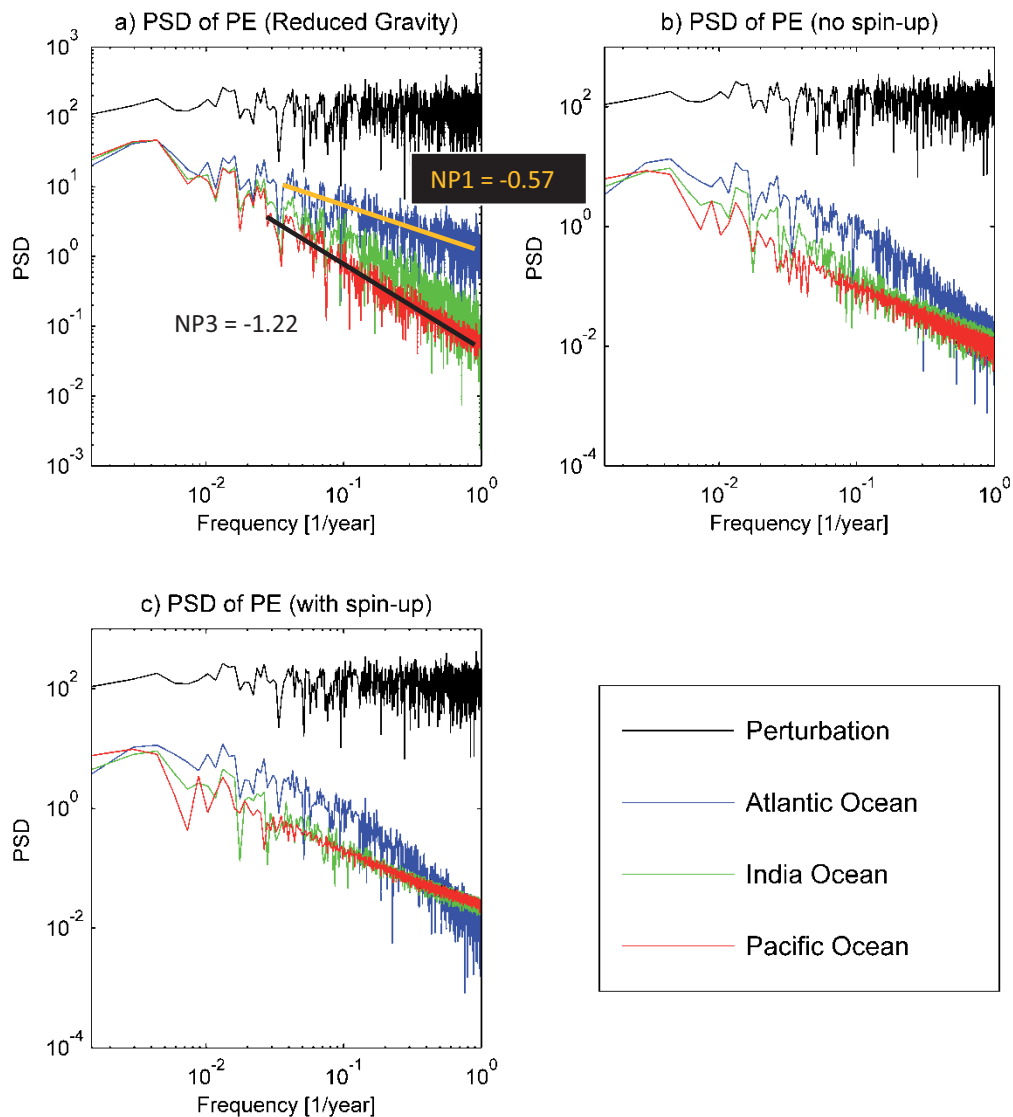


Figure 4.3: Power spectral density of a) PE from the *reduced gravity* experiment units of  $m/year^{-1}$ , b) PE from the BarBI no-spin up experiment and c) PE from the BarBI with spin-up experiment in units of  $(m^3/s^2)/year^{-1}$

using  $\log(psd) = slope \times \log(frequency) + intercept$ , where  $psd$  is the power spectral density, and are found to be  $-0.57$  and  $-1.22$  respectively. The spectra become redder, as the anomaly moves away from its point of origin. The spectra of the three ocean basin converges at frequencies lower than  $0.01 \text{ years}^{-1}$ , which is equivalent to a period of 100 years. Note that the peaks of the spectra of the three ocean basin correlate strongly with the peaks of the perturbation for frequencies less than  $0.2 \text{ year}^{-1}$  (period of 5 years). For

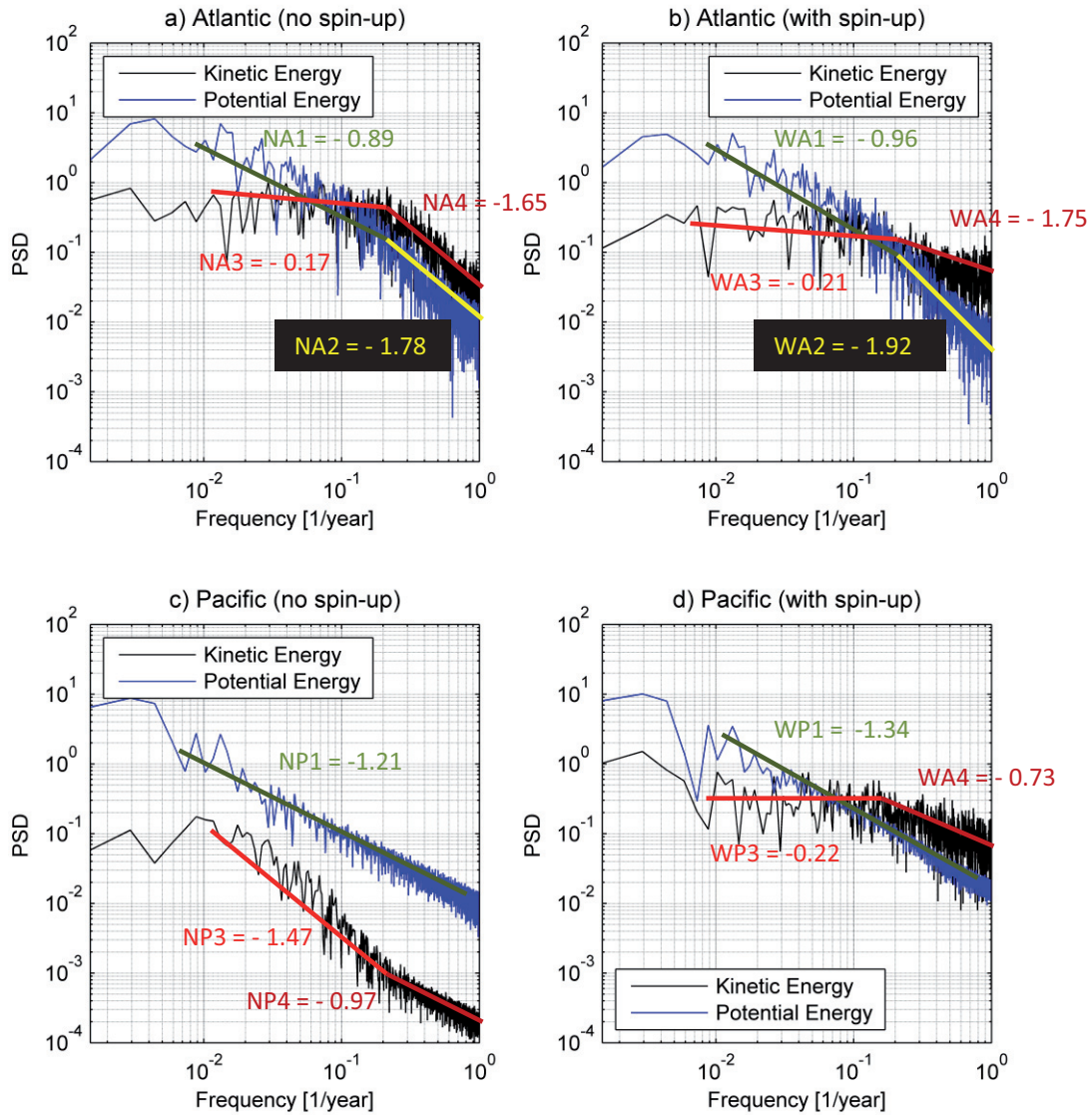


Figure 4.4: Power spectral density of kinetic energy and potential energy of Atlantic Ocean BarBI in the a) no spin-up and b) with spin-up experiments, and Pacific Ocean in c) no spin-up and d) with spin-up experiments. Slopes for the high frequency and low frequency part of the spectra are shown with matching color as the color of trend line. [All psd in units of  $(m^3/s^2)/year^{-1}$ ]

higher frequencies, the perturbation peaks correlate with the peaks of the Atlantic Ocean, but not with the Pacific and Indian Ocean (Figure 4.5 a shows the squared coherence). This result suggests that, although fast Kelvin waves or other coastally trapped waves transmit the initial anomaly along the boundaries and the equator within a few months to a year, the amplitude of response is insignificant, specially in the second and the third basin (Indian

and Pacific in this case), as we can see from the high frequency regime of the spectra. Significant isopycnal displacement is possible only through persistent perturbation with larger periods that generates baroclinic basin modes of Rossby waves.

For a transport of fixed magnitude, the amount of water pumped into the thermocline peaks at  $T_N/\omega$ . This water has to spread over a large area, which explains why  $h_e$  (in our case  $PE \propto h_e^2$ ) is increasing as frequency is reduced. This spreading over large area is the major reason for reddening of the ocean response to fluctuations in high-latitude forcing. With increase in distance from the location of forcing, the water has to spread over larger area, and hence the response gets even redder. The equatorial belt contributes substantially into the integral even at high frequencies as the belt covers a rather large area. As this area has to be filled, it blocks high frequencies and acts as a low pass filter. This phenomenon of the equator acting as a low pass filter is termed as “*equatorial buffer*” by Johnson and Marshall (2002)

Figure 4.3 b) and c) compares the power spectra of PE in the Atlantic, Indian and Pacific Ocean, to the perturbation power spectral density of potential energy from the BarBI *no spin-up* experiment and potential energy from the BarBI *with spin-up* experiments respectively. For the frequency range  $0.001 \text{ year}^{-1}$ -  $0.18 \text{ year}^{-1}$  (period of 1000 years - 5.5 years), the spectra of the Pacific Ocean is redder than the spectra of the Atlantic Ocean (Atlantic slope: - 0.89, Pacific slope: - 1.21), agreeing with the spectra of the *reduced gravity* case. However, for frequencies higher than  $0.18 \text{ year}^{-1}$  (periods smaller than 5.5 years), there is a pronounced difference between the spectra of the Atlantic Ocean in the *reduced gravity* setup and the spectra of the Atlantic in the *no spin-up* and *with spin-up* setup. In this case, for frequencies higher than  $0.18 \text{ year}^{-1}$  (periods smaller than 5.5 years), the spectrum of PE of the Atlantic Ocean reddens and the amplitude drops. In the *with spin-up* case, the reddening and amplitude drop of the spectrum of PE of the Atlantic Ocean is even stronger implying that circulation damps high frequency waves.

BarBI produces the interaction of barotropic and baroclinic waves in the presence of topography and stratification. Figure 4.4 a) compares the spectra of the depth integrated

Kinetic Energy calculated from the streamfunction as,  $KE = \frac{1}{2}H (\nabla\psi/H)^2$ , and PE for the *no spin-up* setup. As we can see, the spectrum is separated at a frequency of  $0.18 \text{ year}^{-1}$  (period of 5.5 years). At that frequency, the slope of the Atlantic Ocean changes from -0.89 to -1.78, clearly indicating the reddening of the spectrum. For frequencies higher than the frequency, the amplitude of the KE leads the amplitude of the PE. However, for frequencies lower than  $0.18 \text{ year}^{-1}$  (period of 5.5 years), the PE amplitude leads, indicating baroclinic timescales.

The reddening of the PE spectrum of the Atlantic Ocean is stronger for the *with spin-up* case than the *no spin-up* case. The slope changes from -0.96 to -1.92 from low to high frequency, as compared to -0.89 to -1.78 for the *no spin-up* case.

There is no significant difference between the reddening of the KE spectra for the *no spin-up* and the *with spin-up* case. As in the *no spin-up* case, for frequencies higher than the critical frequency, the amplitude of the KE leads the amplitude of the PE, and for lower frequencies, baroclinic dynamics dominate.

Figure 4.4 c) and d) compares the spectra of the KE and PE of Pacific Ocean for the *no spin-up* and *with spin-up* cases. The spectrum of PE is slightly redder for the *with spin-up* (slope -1.34) case than for the *no spin-up* (slope -1.21) case, again indicating that high frequency variability is damped by circulation. Yet the difference is not so strong, and the amplitudes are almost identical.

Although, there is a difference between the amplitude of KE for the *no spin-up* and the *with spin-up* case, the amplitudes in both cases are much lower compared to the amplitude of the perturbation (Figure 4.3), which implies that barotropic variability is damped at all frequencies before they reach the 2nd and 3rd basin (Indian and Pacific Ocean respectively).

An important thing to note in Figure 4.3 is that, at all frequencies, the response in all the basins have higher amplitudes in the *reduced gravity* setup than in the *no spin-up* or *with spin-up* setup.

Figure 4.5 a) shows the coherence of PE in the Atlantic, Indian and Pacific Ocean, to

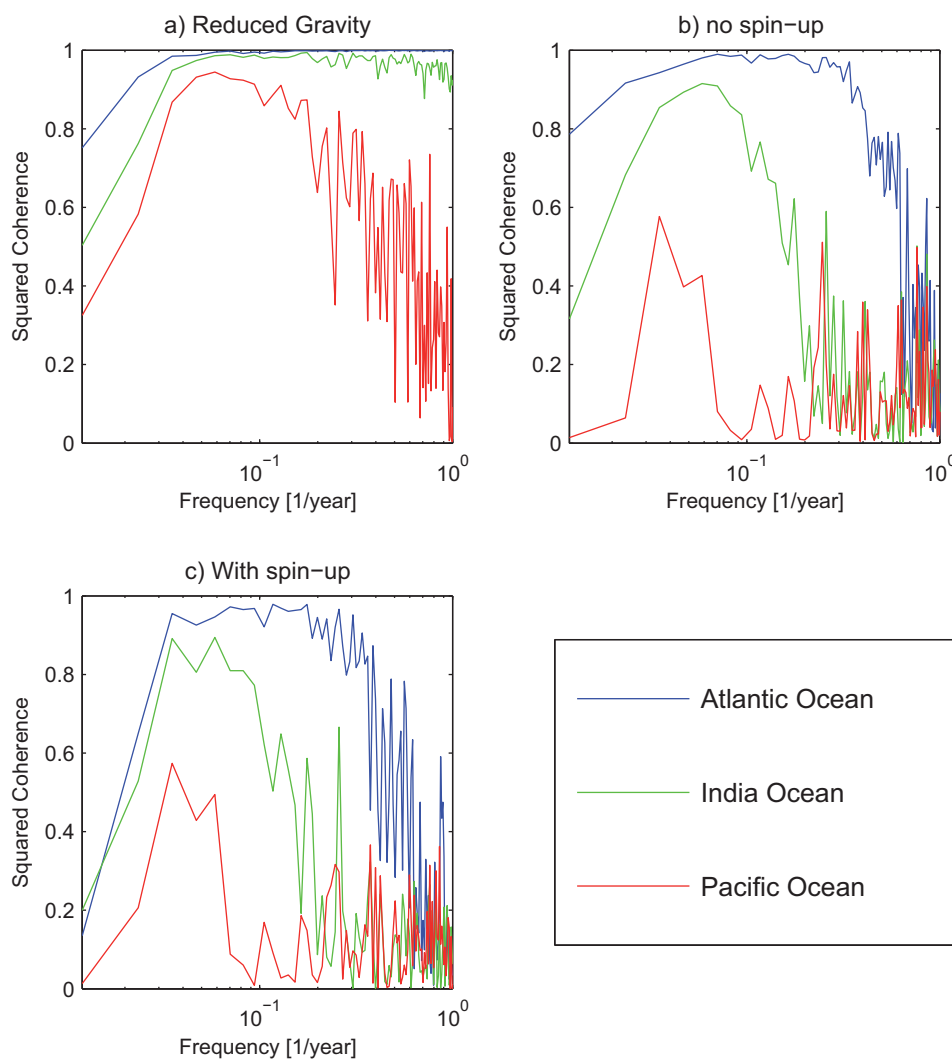


Figure 4.5: Squared coherence of a) SSH from the *FEOM* experiment, b) Potential energy from the BarBI no-spin up experiment and c) Potential energy from the BarBI with spin-up experiment

the square of the perturbation in the *reduced gravity* experiment. At frequencies lower than  $0.035 \text{ year}^{-1}$  (period larger than 30 years), there is a dip in the coherence between the PE of all three ocean basins and the perturbation. PE in the Atlantic is highly coherent with the perturbation in all frequencies above  $0.035 \text{ year}^{-1}$  (periods lower than 30 years). PE of the Indian Ocean is also highly coherent at the frequency of  $0.035 \text{ year}^{-1} - 0.18 \text{ year}^{-1}$ . At frequencies above  $0.18 \text{ year}^{-1}$ , the coherence between the Indian PE and the perturbation is marginally less than the coherence between the Atlantic PE and the

perturbation. The Pacific PE is highly coherent with the perturbation in the frequency range  $0.035 \text{ year}^{-1} - 0.18 \text{ year}^{-1}$ . At frequencies above  $0.128 \text{ year}^{-1}$ , the coherence between the Pacific PE and the perturbation is noticeably less than the coherence between the Atlantic PE and the perturbation.

Figure 4.5 b) and c) show the coherence of PE in the Atlantic, Indian and Pacific Ocean, to the perturbation in the *no spin-up* and *with spin-up* experiments respectively. In both the cases, the PE in the Atlantic is coherent to the perturbation in the frequency range of  $0.035 \text{ year}^{-1} - 0.34 \text{ year}^{-1}$ , in contrast to the *reduced gravity* case, where the Atlantic PE is coherent to the perturbation at higher frequencies as well. The Indian PE is coherent to the perturbation in the frequency range  $0.035 \text{ year}^{-1} - 0.17 \text{ year}^{-1}$  for the *no spin-up* case and in the range  $0.035 \text{ year}^{-1} - 0.12 \text{ year}^{-1}$  for the *with spin-up* case. In both the cases, the PE in the Pacific is coherent to the perturbation in the frequency range of  $0.023 \text{ year}^{-1} - 0.07 \text{ year}^{-1}$ .

#### 4.2.2.2 Wave adjustment in the *reduced gravity* setup

The deep water formation or transport anomaly in the *reduced gravity* setup initiated at the Labrador Sea, propagates as a coastal wave in the form of thermocline displacement along the eastern coast of North America till it reaches the equator. At the equator, the thermocline displacement anomaly propagates eastward as an equatorial Kelvin wave. Upon reaching the West African coast, the wave splits and propagate polewards radiating westward propagating Rossby waves into the interior of the Atlantic Ocean. The wave propagating southward along the western coast of Africa, continues to propagate around the southern tip of Africa, northward into the Indian Ocean. At the equator, the signal turns right and propagate eastwards, crosses the Indonesian archipelago, into the Pacific Ocean, crosses the equator till it reaches the eastern Pacific coast, splits and propagate polewards.

Figure 4.6 a), c) and e) show the first EOF (Empirical Orthogonal Functions) of thermocline displacement in the Atlantic Ocean, Indian Ocean and Pacific Ocean respectively,

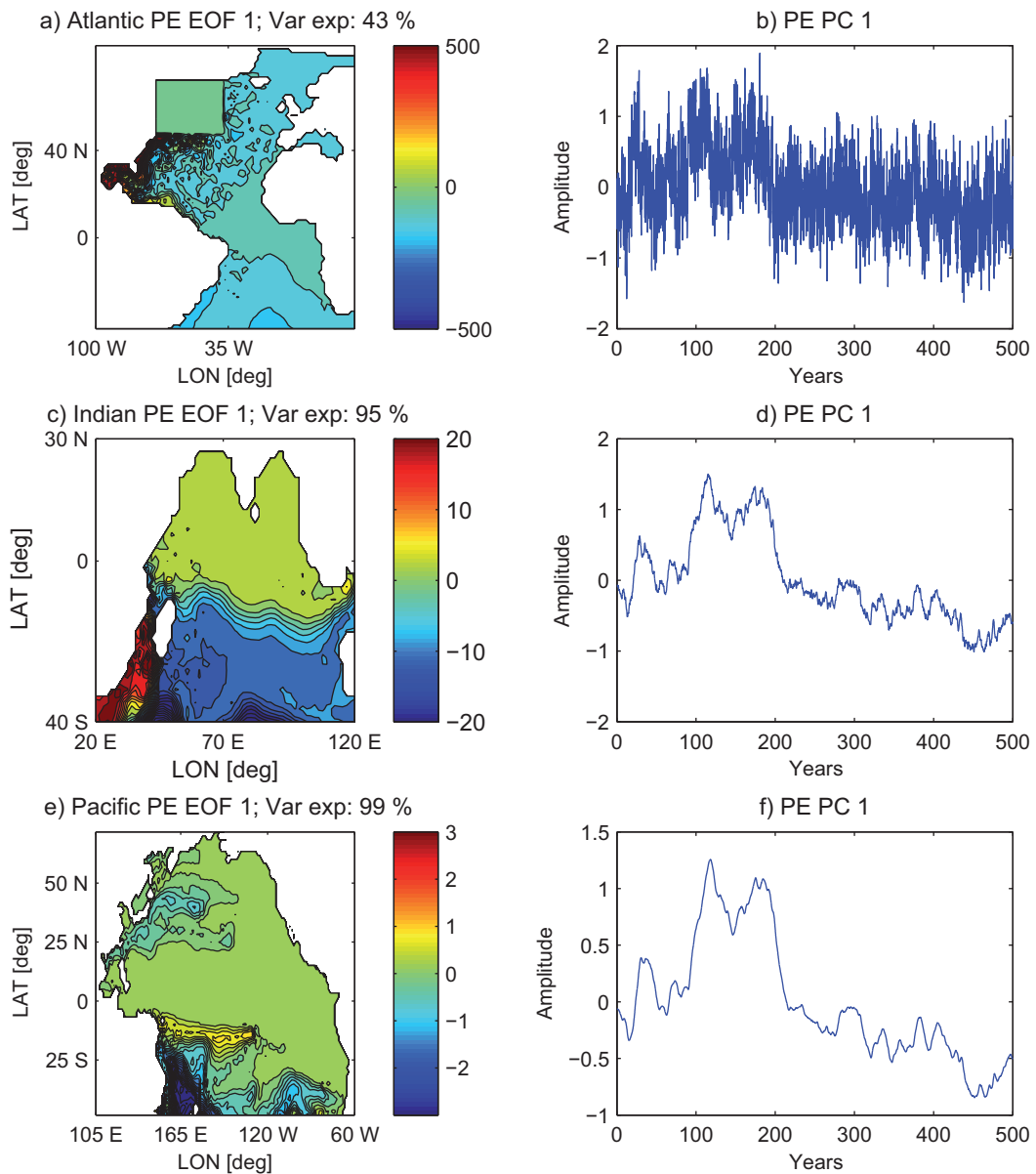


Figure 4.6: EOFs and the corresponding PCs of thermocline displacement of a, b) Atlantic Ocean, c, d) Indian Ocean and e, f) Pacific Ocean from the *reduced gravity* experiment. The location of the prescribed forcing area (Labrador Sea) is removed before calculating the EOFs.

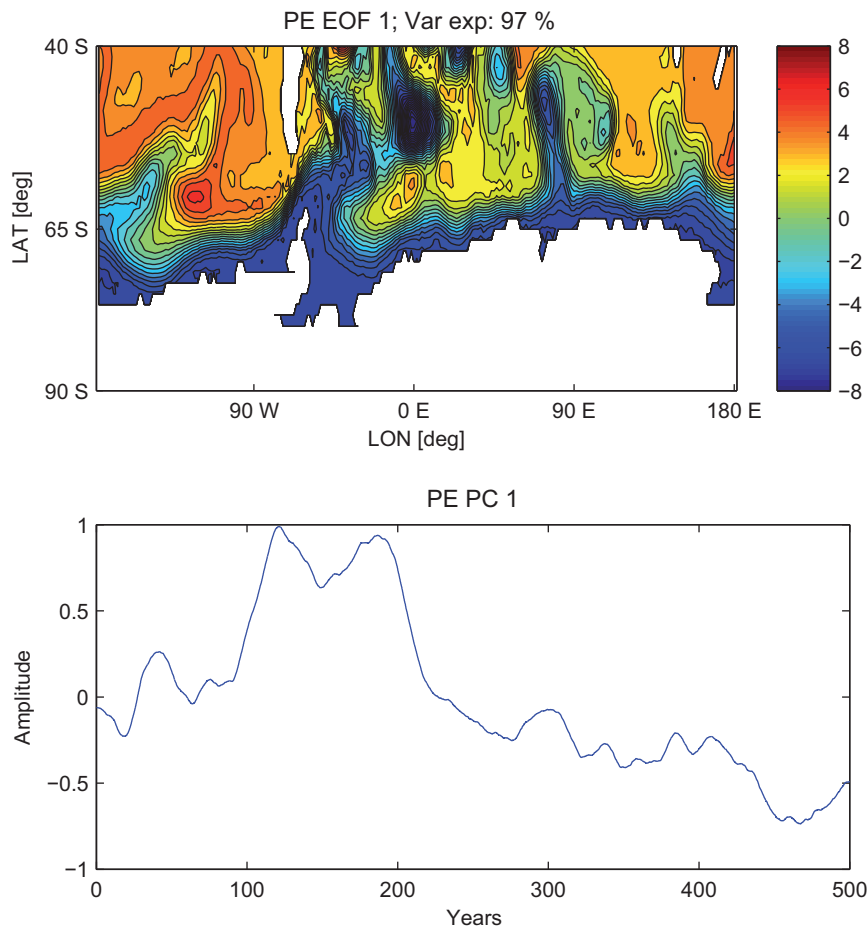


Figure 4.7: EOFs and the corresponding PCs of thermocline displacement of the Southern Ocean from the *reduced gravity* experiment

and b), d) and f) show the respective PC (Principal Components). In order to illustrate the mode, the location of the prescribed forcing area (Labrador Sea) is removed before calculating the EOF. Strongest coherent variability in the Atlantic Ocean can be seen along the eastern coast of North America, where the initial coastal wave carries the thermohaline displacement perturbation southward to the equator. Along the western coast of Africa, the mode of variability is not as strong, as the thermohaline displacement anomaly does not re-amplify (Johnson and Marshall, 2004). The westward propagating pattern of Rossby waves can clearly be seen, with the phase speed of Rossby wave decreasing as one moves poleward from the equator.

The leading mode of adjustment in the Indian Ocean is clearly the westward propagating Rossby waves (Figure 4.6 c) . The response in the Indian Ocean is less than in the Atlantic Ocean. Another strong feature that is observable is the incoming coastally trapped wave from Atlantic Ocean along the south eastern coast of Africa.

The leading mode in the Pacific Ocean is related to the westward propagating Rossby waves. However, the structure of the Rossby wave mode in the Pacific is not as prominent as it is in the Atlantic or the Indian Ocean. The response is even smaller in the Pacific Ocean.

Figure 4.7 a) shows the first EOF of SSH in the Southern Ocean and b) shows the corresponding PC. The coastal region around Antarctica is adjusted through coastally trapped waves. If we compare the PCs of the first EOFs of the Atlantic Ocean, Indian Ocean, Pacific Ocean and Southern Ocean (Figure 4.6 b), d), f) and Figure 4.7 b) respectively), we can see that, as the perturbation moves away from its point of origin, the high frequency component of the signal is filtered out illustrating once again that the ocean acts as a low pass filter.

#### 4.2.2.3 Wave adjustment in the *no spin-up* setup

The global wave adjustment, due to the perturbation of the deep water formation rate at the Labrador Sea in the *no spin-up* setup of BarBI, takes through the same pathways as it does in the *reduced gravity* experiment mentioned earlier. Figure 4.8 a), c) and e) shows the first EOF of thermohaline displacement in the Atlantic Ocean, Indian Ocean and Pacific Ocean respectively, and b), d) and f) shows the respective PC. The location of the prescribed perturbation area (Labrador Sea) has been removed here as well before calculating the EOFs to illustrate the mode of anomaly propagation.

In the Atlantic Ocean, the leading mode includes the coastal wave pathway along the north-western coast, where the initial wave carries the PE perturbation southward to the equator. The interior of the Atlantic is adjusted by westward propagating Rossby waves. The wave-front of these westward propagating Rossby waves is quite pronounced, and

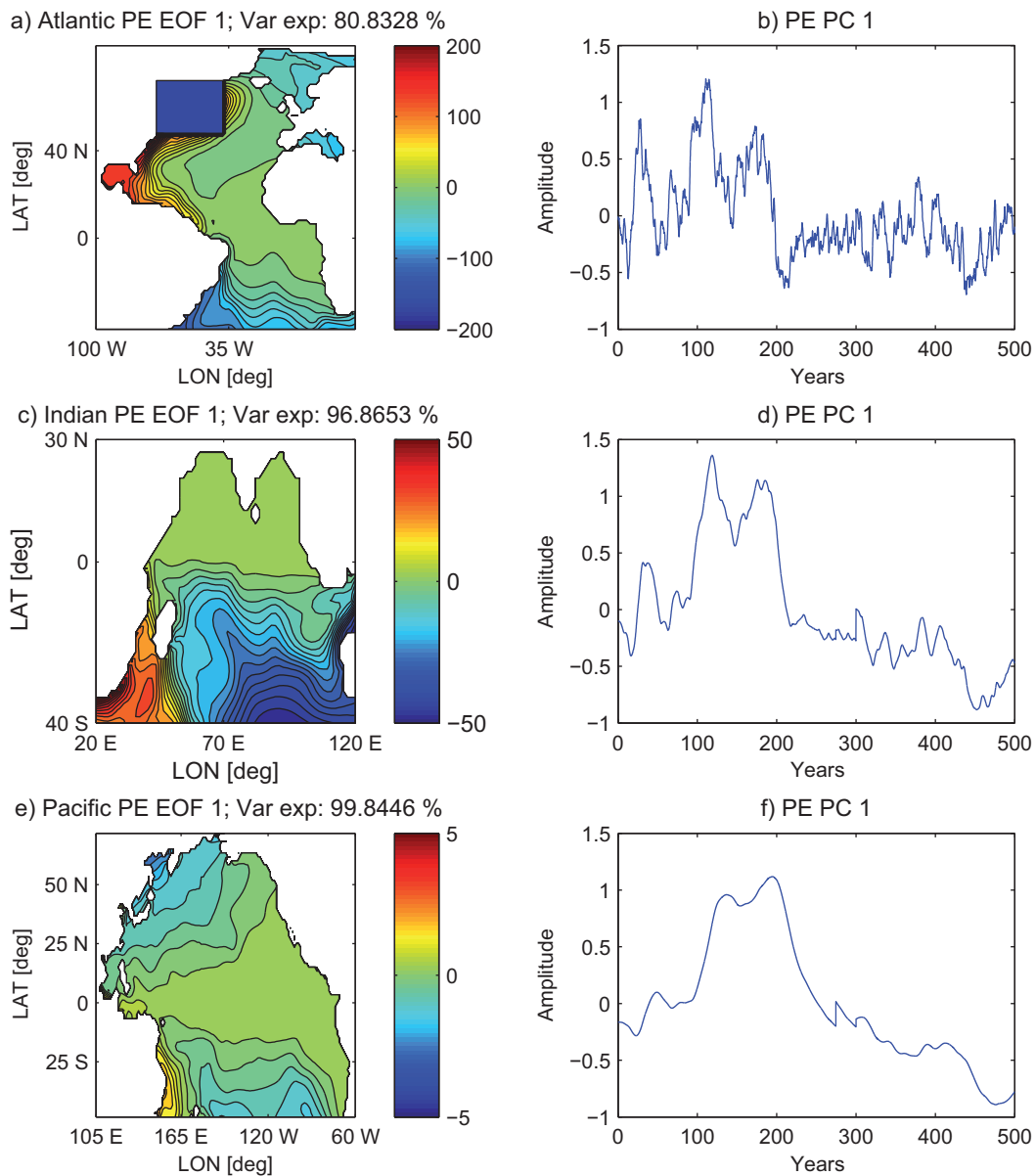


Figure 4.8: EOFs and the corresponding PCs of thermocline displacement of a, b) Atlantic Ocean, c, d) Indian Ocean and e, f) Pacific Ocean from the BarBI *no spin-up* experiment. The location of the prescribed forcing area (Labrador Sea) is removed before calculating the EOFs.

the decrease of Rossby wave phase speed, as one moves poleward from the equator

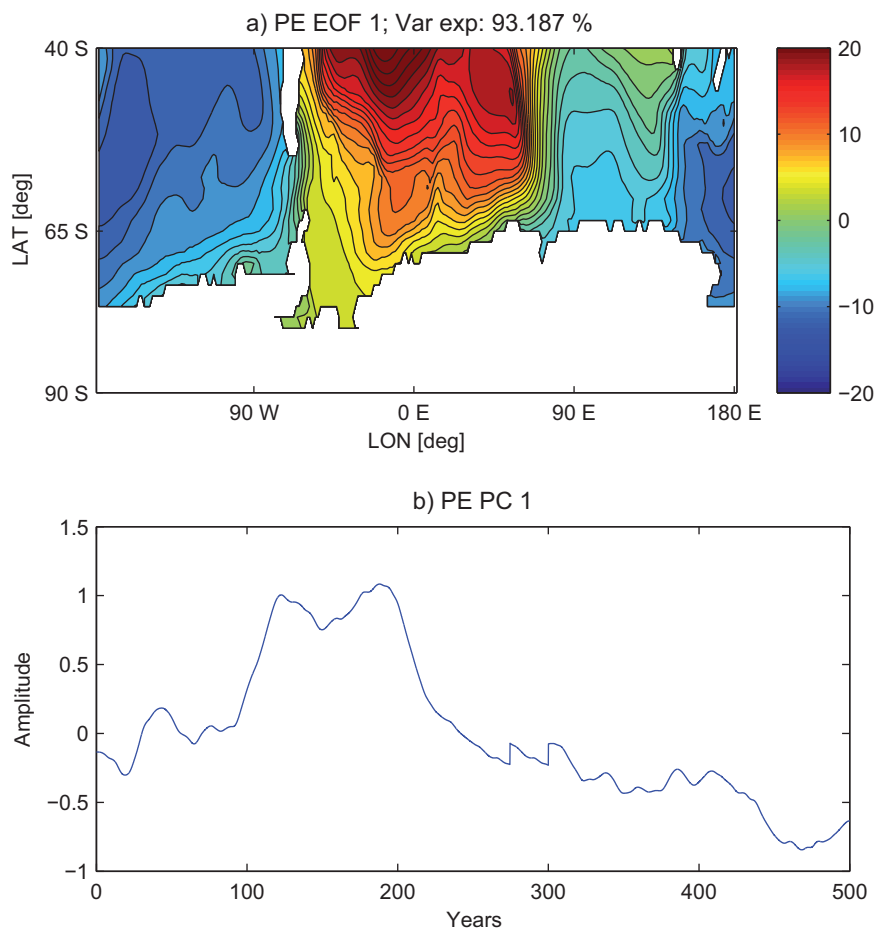


Figure 4.9: EOF and the corresponding PC of thermocline displacement of the Southern Ocean from the BarBI *no spin-up* experiment

can be clearly seen.

The equatorial response PE in the Indian Ocean is reduced due to the topography between Africa and Madagascar. The leading mode of adjustment in the Indian Ocean are the westward propagating Rossby waves.

The leading mode of adjustment of PE in the *no spin-up* setup of BarBI in the Pacific Ocean is much more prominent than the leading mode of adjustment of SSH in *reduced gravity* setup. Equatorial Kelvin wave introduces the perturbation into the Pacific Ocean through the Indonesian Archipelago. The wave crosses the equator, splits upon reaching the eastern coast, propagates poleward, while radiating westward propagating Rossby

waves. The wave-fronts of these westward propagating Rossby waves is quite distinct.

Figure 4.9 a) shows the first EOF of PE in the Southern Ocean and b) shows the corresponding PC. The leading mode here shows that the disturbance is carried into the Southern Ocean through westward propagating Rossby waves in the Atlantic, Pacific and Indian basins. The perturbation is largest in the Atlantic sector of the Southern Ocean as the signal is originated at the Atlantic Ocean. Comparing the PCs of the first EOFs of the Atlantic Ocean, Indian Ocean, Pacific Ocean and Southern Ocean (Figure 4.8 b), d), f) and Figure 4.9 b) respectively), we can again see that, as the perturbation moves away from its point of origin, the high frequency component of the signal is filtered out. The PC of thermohaline displacement from the *reduced gravity* setup in the Indian and the Pacific Ocean are qualitatively similar to the PC of thermohaline displacement from the *no spin-up* BarBI setup in the Indian and the Pacific Ocean.

#### 4.2.2.4 Wave adjustment in the *with spin-up* setup

The global wave adjustment to the perturbation of the deep water formation rate at the Labrador Sea in the *with spin-up* setup of BarBI, takes place through the similar pathways as it does in the *no spin-up* setup of BarBI mentioned earlier in this section. Figure 4.10 a), c) and e) shows the first EOF of thermocline displacement in the Atlantic Ocean, Indian Ocean and Pacific Ocean respectively, and b), d) and f) shows the respective PC. Same as in the other cases, areas where forcing is applied (Labrador Sea) has been removed here as well before calculating the EOFs to illustrate the mode of anomaly propagation.

The leading mode in the Atlantic and the Indian is quite similar to the the leading mode of the *no spin-up* set-up. In the North Atlantic, the pathway of the northern front of the Rossby wave (above  $45^{\circ}N$ ) is confronted by the eastward flowing part of the sub-tropical gyre, hindering the propagation of the slow Rossby wave. Hence, we see a difference in the pattern of the wave front between the *no spin-up* and the *with spin-up* case. As in the previous case, the equatorial response of PE in the Indian Ocean seems to be limited due to the topography between Africa and Madagascar.

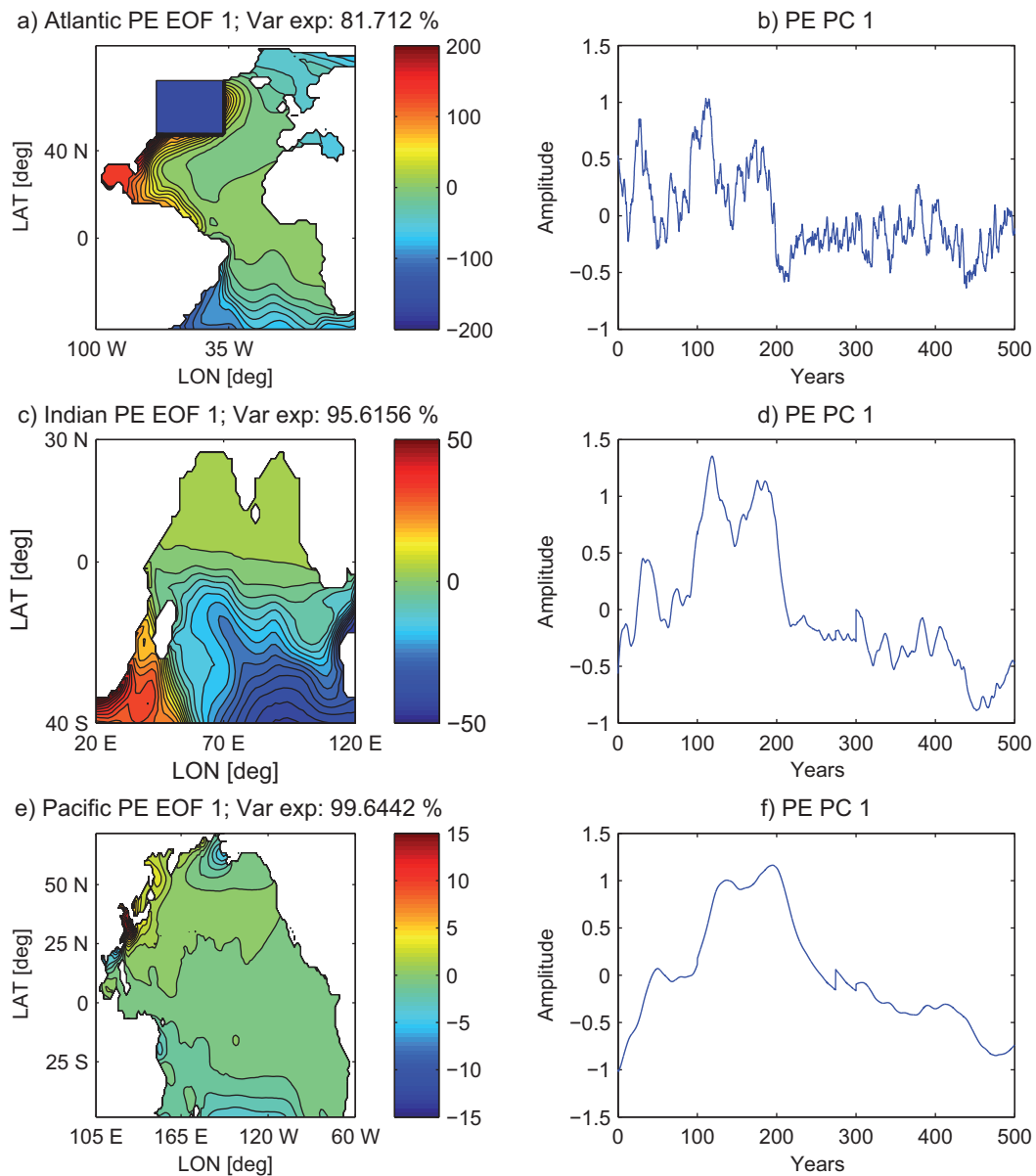


Figure 4.10: EOFs and the corresponding PCs of thermocline displacement of a, b) Atlantic Ocean, c, d) Indian Ocean and e, f) Pacific Ocean from the BarBI *with spin-up* experiment. The location of the prescribed forcing area (Labrador Sea) is removed before calculating the EOFs.

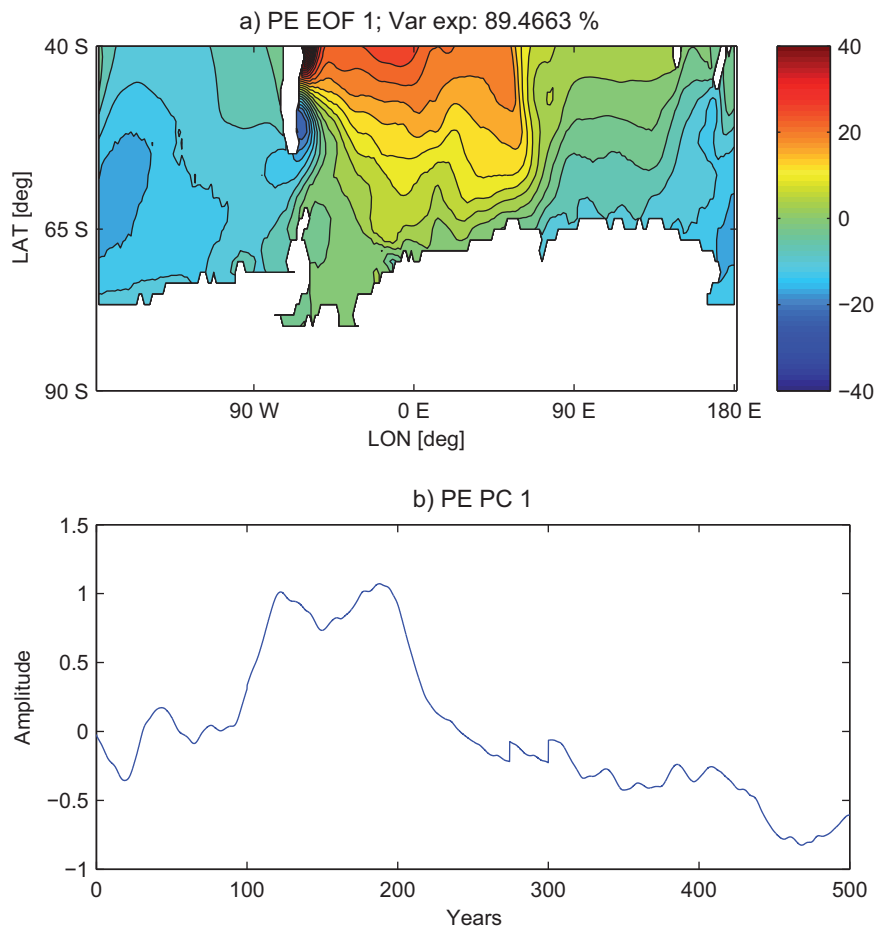


Figure 4.11: EOF and the corresponding PC of thermocline displacement of the Southern Ocean from the BarBI in the *with spin-up* experiment

The leading mode of adjustment of PE in the *with spin-up* set-up of BarBI in the Pacific Ocean is a little different from the *no spin-up* set-up. The perturbation is again introduced by an equatorial Kelvin wave through the Indonesian Archipelago and the interior of the Pacific is adjusted via westward propagating Rossby wave. However, there are certain features in the North-Western Pacific (Figure 4.10 e), which are missing in the case of the *no spin-up* set-up. This feature could be due to the interaction of the westward propagating Rossby wave with the western boundary currents.

Figure 4.11 a) shows the first EOF of thermocline displacement in the Southern Ocean

and b) shows the corresponding PC. The leading mode here is similar to the *no spin-up* set-up. The disturbance is carried into the Southern Ocean through westward propagating Rossby wave in the Atlantic, Pacific and Indian basins. The perturbation is the strongest in the part south of the Atlantic as the signal originated in the Atlantic. Comparison of the PCs of the first EOFs of the Atlantic Ocean, Indian Ocean, Pacific Ocean and Southern Ocean (Figure 4.10 b), d), f) and Figure 4.11 b) respectively), again shows that, as the perturbation moves away from its point of origin, the high frequency component of the signal is filtered out.

#### 4.2.2.5 Amplitude of response in the three setups

To understand the magnitude of impact that is imposed through oceanic wave teleconnection between ocean basins, we look at the amplitude of response in PE ( $\Delta PE \propto (h_e^2 - \bar{h}_e^2)$ ) in the three ocean basins. In Figure 4.12, we compare the amplitude of response at the eastern coast of South Atlantic Ocean (10 E 20 S), eastern coast of South Indian Ocean (100 E 20 S) and eastern coast of South Pacific Ocean (80 W 20 S) for the *reduced gravity*, *no spin-up* and *with spin-up* setup. We chose the South Atlantic Ocean, as the magnitude of response in the Southern hemisphere is slower and smaller due to the equatorial buffer (Johnson and Marshall, 2002). The response in the *reduced gravity* setup is in rough agreement with the theoretical study (c.f. 6 of Johnson and Marshall (2004) in all three basins. However, there is a prominent reduction in the amplitude upon introduction of bottom topography and background mean circulation. In the Southern Hemisphere of basin 1 (Atlantic Ocean), the maximum deviation of PE from its average is 20% in the presence of topography and 12 % in the presence of circulation as opposed to 45 % in the reduced gravity setup for a period of 200 years. The maximum deviation of PE in basin 2 and 3 (Indian and Pacific Ocean respectively) is less than 20 % for all periods in the presence of topography and circulation, while it is above 40 % for large periods in the reduced gravity setup. In the presence of topography, attenuation increases and the amplitude of response in the Indian and the Pacific Ocean, for periods smaller than 100

years is considerably smaller (deviation of 3 % - 5 % from its mean value) than in the reduced gravity case. The response increases marginally for periods larger than 100 years. However, as the experiment was run for 500 years, we should be careful in treating the results for larger periods.

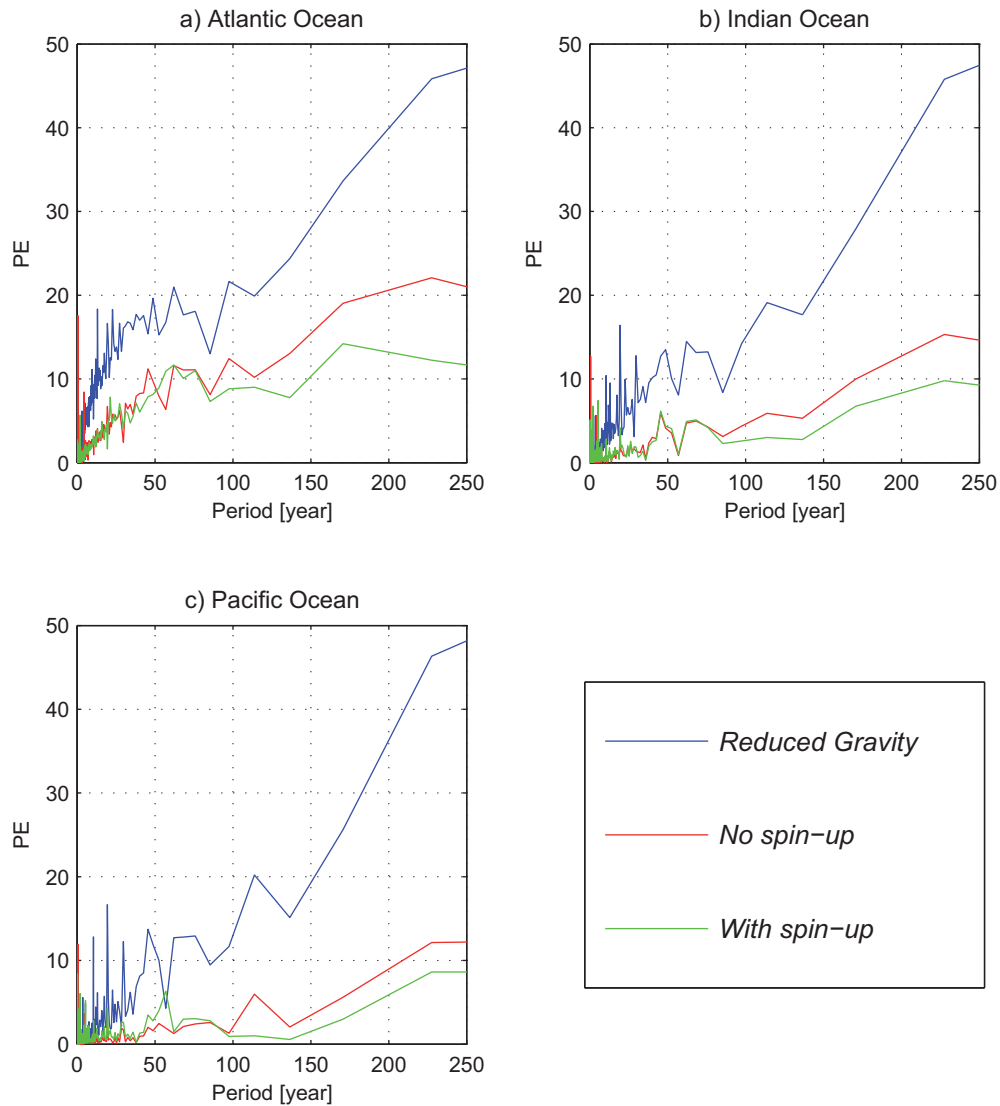


Figure 4.12: Spectrum of PE response to the buoyancy perturbation in Labrador Sea at the a) Atlantic Ocean, b) Indian Ocean, c) Pacific Ocean for the reduced gravity, no spin-up and with spin-up experiments.

In the *no spin-up* experiment, the amplitude of KE is higher for smaller periods in

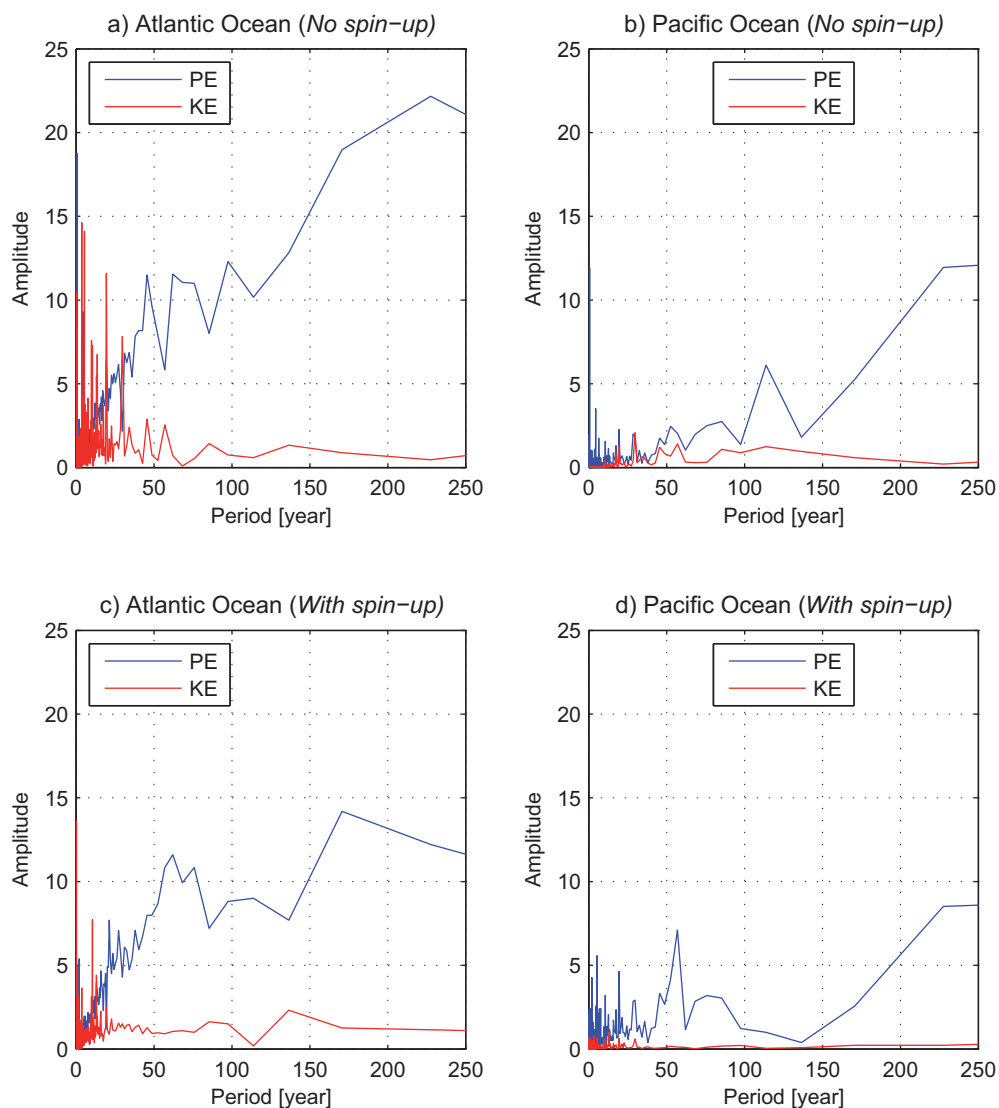


Figure 4.13: Spectrum of PE and KE response to the buoyancy perturbation in Labrador Sea at the a) Atlantic Ocean for the no spin-up experiment, b) Pacific Ocean for the no spin-up experiment, c) Atlantic Ocean for the with spin-up experiment, d) Pacific Ocean for the with spin-up experiment.

the Atlantic Ocean (Figure 4.13). In the *with spin-up* experiment, the amplitude of KE is weak in both the basins. There is less than 2 % deviation from the mean value of KE, which is quite small. There is a decrease of amplitude of PE in the Atlantic Ocean for the with spinup experiments suggesting that circulation dampens the waves. However, the difference in deviation of PE from its mean value at large periods between the *no spin-*

*up* and the *with spin-up* experiments is 4 %, suggesting that for low frequency forcing, circulation does not play a major role in dampening low frequency baroclinic adjustment.

#### 4.2.2.6 Time scale of adjustment in the three experiments

Figure 4 a) show the global thermocline thickness response time for the reduced gravity experiment. Figure 4.14 b), c), d) and e) shows the time scale of propagation of the perturbation of streamfunction and PE in the *no spin-up* and *with spin-up* experiments. The difference in the adjustment time scale of PE for the *with spin-up* and *no spin-up* experiment is shown in Figure 4.14 f). Note that Figure 4.14 does not show the first arrival time of the signal. The time scale of adjustment is calculated by using lag cross correlation. The plot shows the time scales in which the variability is most strongly correlated with the applied perturbation at the Labrador Sea.

The response in streamfunction spreads across the Atlantic ocean within a couple of months and it propagates into the Indian and the Pacific ocean basins within a couple of years. The potential energy take much longer to spread across the three ocean basins as the low frequency baroclinic Rossby waves travel at a speed of few centimeters per second. In both the *no spin-up* and *with spin-up* cases, the anomaly spreads along the western coast upto the equator within the first 5-6 months. It takes another ~ 3 months to cross the equator. The interior of the Atlantic Ocean is adjusted through westward propagating Rossby waves. The North Atlantic is adjusted within 5 years. The South Atlantic takes longer due to the equatorial buffer effect as mentioned above (Johnson and Marshall, 2002). There is a significant difference between the arrival time of the anomaly to the coast of Argentina between the the *no spin-up* and *with spin-up* experiments. As we can see from the spin-up of the wind driven circulation, the ACC turns northward following topography after crossing the Drake Passage (Figure 2.8 on page 19). The difference between the arrival time of the anomaly to the coast of Argentina between the *no spin-up* and *with spin-up* experiments could be due to the interaction of westward propagating Rossby wave with the ACC. Nevertheless, there is no significant difference

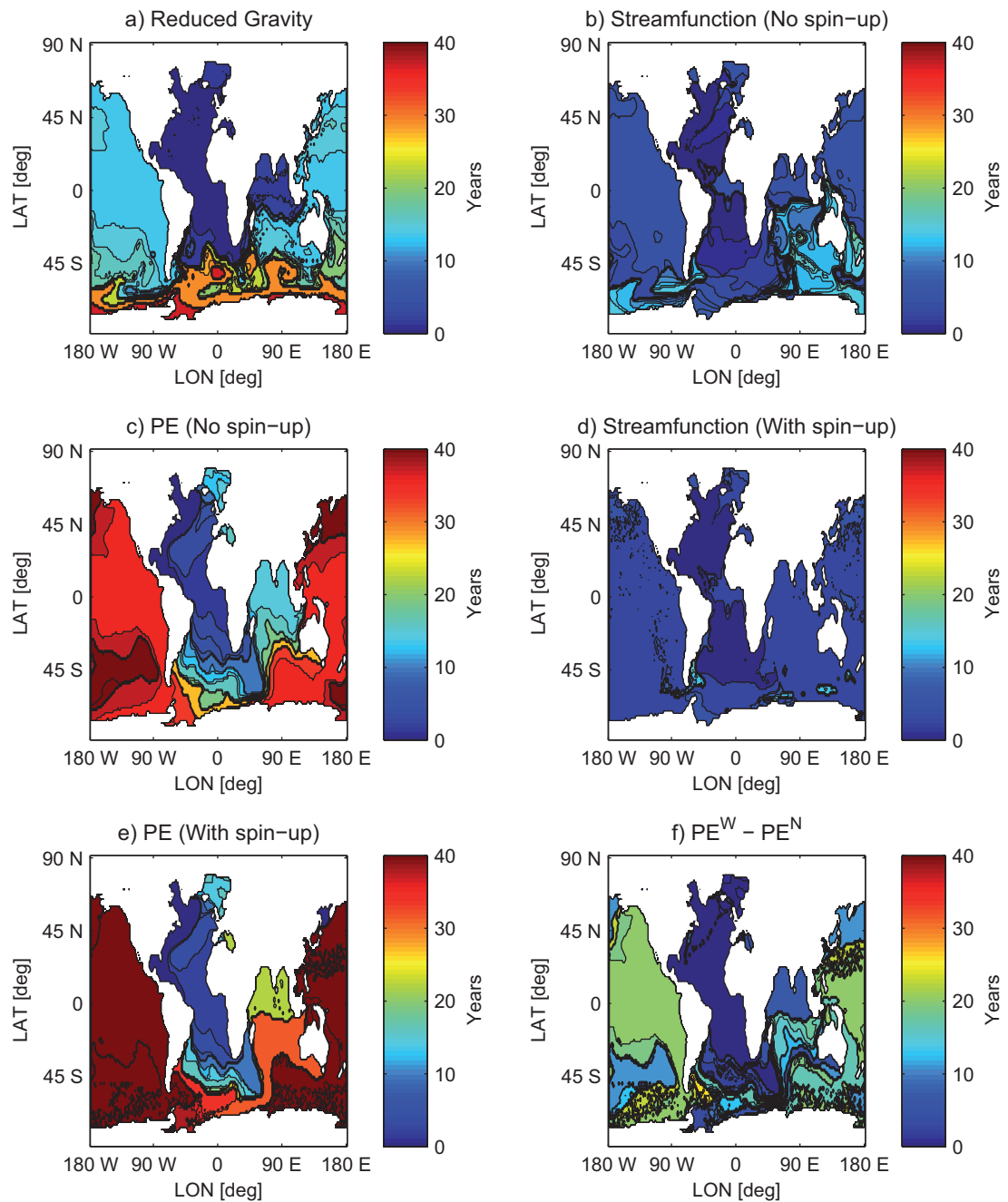


Figure 4.14: Lag plots showing the time taken for the perturbation to travel from the Labrador Sea to the other ocean basins. a) shows the time scales in the *reduced gravity* experiment b) and c) shows the propagation time of the barotropic streamfunction and PE for the *no spin-up* setup respectively; d) and e) shows the propagation time of the barotropic streamfunction and PE for the *no spin-up* setup respectively *with spin-up* experiments; f) shows the difference in the time scales of propagation of PE between the *with spin-up* and *no spin-up* experiments;

in the wave adjustment of the Atlantic basins between the *no spin-up* and *with spin-up* experiments.

However, in the *with spin-up* set-up, as the anomaly enters the Indian Ocean, along the Southern tip of South Africa, it encounters the Northern branch of the sub-tropical gyre and the Mozambique current flowing southward. This slows the response of the Indian Ocean by 7-8 years in the *with spin-up* set-up as compared to the in the *no spin-up* set-up. The signal further slows down before entering the Pacific Ocean, as it encounters the Indonesian through-flow. Hence, the difference in the response time of the Pacific Ocean between the two set-up is of the order of 15 years.

Bottom topography does not play a part in the anomaly propagation in the *reduced gravity* case as the perturbation sits on the upper layer of the ocean. The phase speed of propagation is given by  $c = \sqrt{g'H}$ , and in BarBI, as we have fast and slow modes in the presence of topography and stratification, the phase speed varies and the response is slower.

### 4.3 Discussion

In this chapter, we presented a study towards a better understanding of global barotropic and baroclinic wave adjustment initiated by buoyancy forcing, under the influence of bottom topography, and in the presence of a background wind driven circulation. Our results show that, amplitude and time scale of oceanic teleconnection through wave adjustment changes significantly upon the introduction of bottom topography and background mean circulation.

The amplitude of response in PE in the Southern Hemisphere of the 1st basin (Atlantic Ocean) is reduced from 45 % in a *reduced gravity* model to 20 % upon the introduction of topography and circulation for large periods. The response in the 2<sup>nd</sup> and the 3<sup>rd</sup> basin is less than 20 %.

We found that in the presence of bottom topography, the time scales of adjustment are

much longer than in *reduced gravity* setups. The presence of background mean circulation further hinders wave propagation, and plays a part in shaping the response time scales and amplitudes. Adjustment process was fastest in the *reduced gravity* experiment, and we were simulating only the first baroclinic mode of waves. Adjustment of the Indian Ocean was delayed by 7-8 years in the presence of circulation, and the adjustment of Pacific Ocean by 15 years.

We analysed the spectra of the global wave response to a perturbation at the Labrador Sea with a white noise spectrum. Our findings illustrate that the amplitude of response clearly depends on the frequency of perturbation. The response in thermocline depth  $h_e$  due to a perturbation in the rate of deep water formation increases as the frequency is decreases. For large periods (100 years and above), the response tends asymptotically to a constant value as the transport from the Southern Ocean balances the forcing in the Northern hemisphere. Physically, for a transport of fixed magnitude, the amount of water pumped into the thermocline in the Northern Hemisphere peaks at  $T_N/\omega$ . This water has to spread over a large area, which explains the increase in amplitude of  $h_e$  with decreasing frequency. Hence the spectrum gets redder with distance. The large area of the equatorial region in the Atlantic Ocean leads to the occurrence of the equatorial buffer (the low pass filtering at the equatorial region). If basins were small with its southern boundary at mid latitudes,  $h$  would be less suppressed at inter annual scales.

However, BarBI experiments allow us to analyse the wave response in terms of barotropic and baroclinic dynamics. The spectra from the BarBI experiments indicate that there is a critical period of approximately 5 years. Furthermore, in the presence of circulation, high frequency baroclinic variability is further dampened. Coherence with perturbation at higher frequency is also lost as the wave travels farther from its origin.

Although wave mechanism represents a rapid route for teleconnection between different ocean basins, we show that the amplitude of response through wave teleconnection seems to be quite small, even in the low frequency regime. This implies that wave adjustment processes initiated by buoyancy forcing in the North Atlantic Ocean might not have

a significant impact on climate modes like ENSO in the Pacific (Timmermann, 2005). We should be careful in treating results from reduced gravity models, which are frequently used for the study of thermocline response due to buoyancy forcing in high latitude. As we showed, neglecting the influence of topography and background mean circulation leads to overestimation of the response amplitude and time in the ocean basins.

We consider the results presented here as a preliminary step towards a clearer understanding of the importance of oceanic teleconnections through barotropic and baroclinic waves. We consider interaction of waves only with a mean wind driven circulation, and we consider the response through barotropic mode and the first baroclinic mode. We expect the amplitude to further reduce upon introduction of more complex dynamics.

# Chapter 5

## Oceanic wave adjustment due to low frequency atmospheric variability

The impact of atmospheric circulation modes like SAM and NAO on ocean circulation have been extensively studied. Olbers and Lettmann (2007) show how the SAM affects the ACC transport via barotropic and baroclinic waves. In the following chapter, the barotropic and baroclinic wave mechanism through which the ocean basins adjust to low and high frequency atmospheric modes (eg. NAO, SAM) is studied. The time-scales and pathways of wave propagation are analysed through series of numerical simulations, performed on BarBI. Two sets of artificial wind stress has been created to represent the NAO type forcing over the North Atlantic and SAM type forcing over the Southern Ocean. The set-up of BarBI and the method used to derive the wind forcings are described in section 5.2. The wind varies at various frequencies. The underlying dynamics of barotropic and baroclinic waves depending on the frequency of wind variability are discussed in section 5.3. Section 5.4 summarises the results.

### 5.1 Model set up

To study the global wave adjustment to wind driven variability due to low frequency atmospheric modes, namely NAO and SAM, the BarBI set up (as described in section

2.2.2) has been used. A global mesh with structured triangular elements of resolution 1.5 degrees is used to perform all the experiments. The BarBI set-up is with an annual mean wind driven background circulation as described in Section 2.2.2.1.

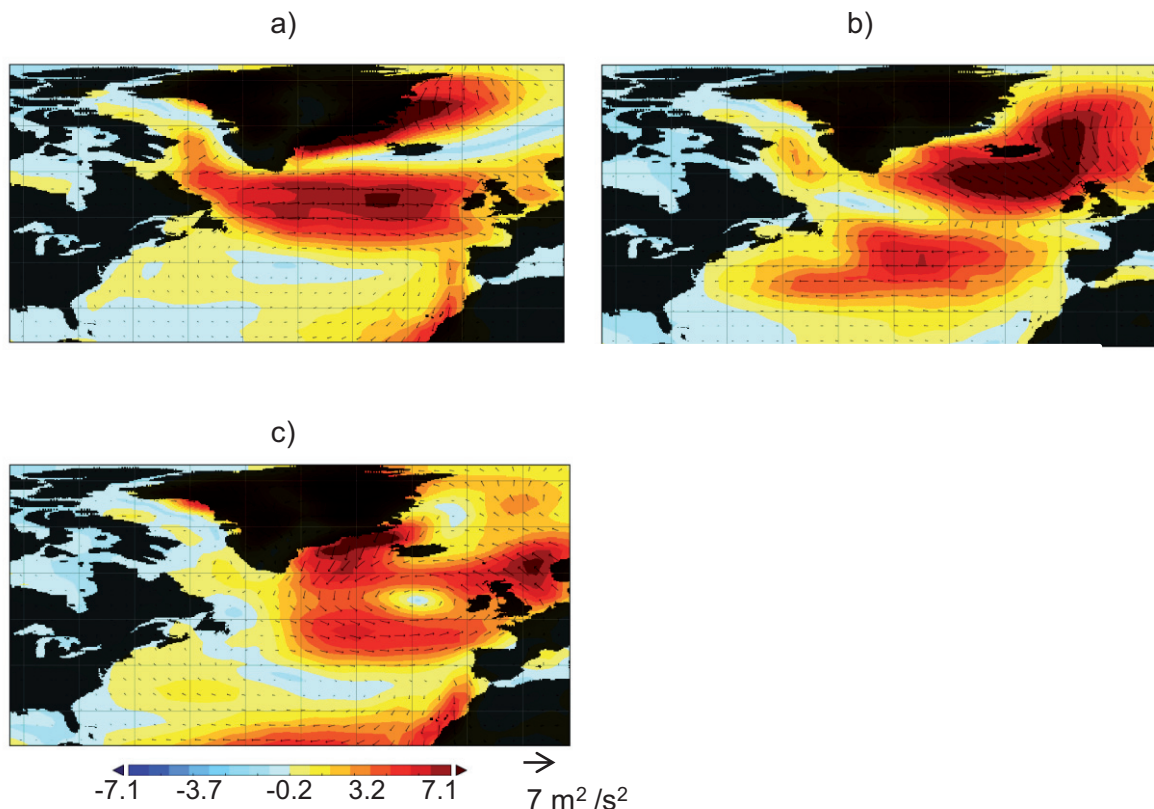


Figure 5.1: First three EOFs (Empirical Orthogonal Functions) of wind stress over the North Atlantic used to develop the NAO type long term wind stress time series, with units  $10^{-2}m^2/s^2$

Two sets of artificial wind stress has been generated to impose NAO type and SAM type perturbation, using a similar method as employed by Olbers and Lettmann (2007). The NAO type wind stress is derived from the first 3 EOFs of the NCEP/NCAR monthly winds of the North Atlantic region ( $25^{\circ}N$   $90^{\circ}W$  -  $75^{\circ}N$   $15^{\circ}E$ ) and a long term mean wind stress  $\bar{\tau}(x,y)$  from 1951 to 2000. The SAM type wind stress is derived from the first 3 EOFs of the NCEP/NCAR monthly winds of the Southern Ocean region (all latitudes below  $40^{\circ}S$ ) and a long term mean wind stress. The first three EOFs for the NAO type wind stress is shown in Figure 5.1 and for the SAM time wind stress is shown in figure 5.2.

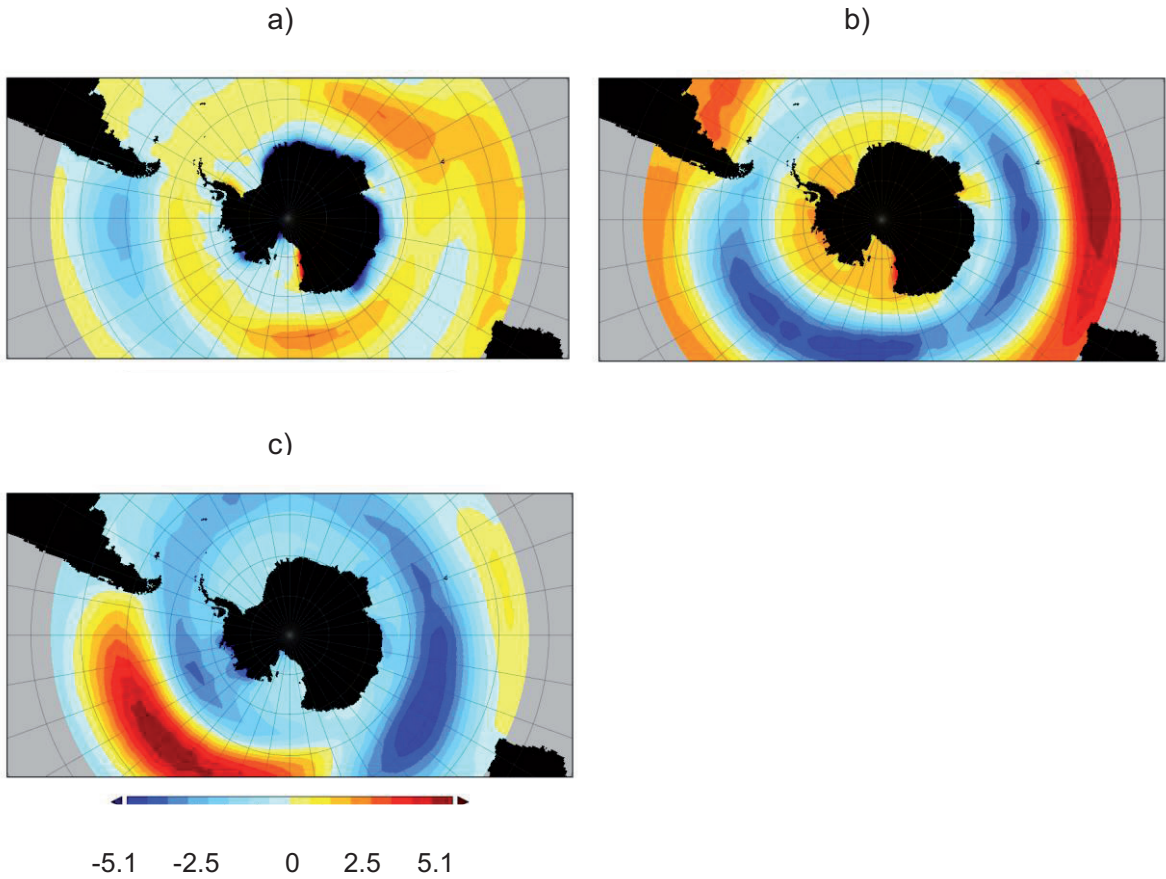


Figure 5.2: First three EOFs of zonal component of the wind stress over the Southern Ocean used to develop the SAM type long term wind stress time series, with units  $10^{-2}m^2/s^2$

The zonal and meridional components of the wind stress have the following forms:

$$\tau^x(x,y,t) = \overline{\tau^x}(x,y) + \sum_{i=1}^3 a_i(t) \cdot \sigma_i^2 \cdot EOF_i^x(x,y) \quad (5.1)$$

$$\tau^y(x,y,t) = \overline{\tau^y}(x,y) + \sum_{i=1}^3 a_i(t) \cdot \sigma_i^2 \cdot EOF_i^y(x,y) \quad (5.2)$$

where  $\sigma_i$  is the variance of the  $i$ -th EOF of  $\tau^x$  or  $\tau^y$ .  $\sigma_i$  helps to control the magnitude of influence of the EOFs. Table 5.2.1 shows the variances of the zonal and meridional components for the NAO and SAM. The amplitudes,  $a_i(t)$  are AR1 type red noise time series with zero mean:

$$a_i(t) = \alpha a_i(t - \Delta t) + Z(t) \quad (5.3)$$

where  $Z(t)$  is white noise, and  $\alpha = 0.79$ . The wind forcings are generated for 1500 years. Figure 5.3 a) shows the spectra of the zonal component of the wind stress used to perturb the Southern Ocean. For periods larger than 10 years, the spectra of the wind stress is white, and for smaller periods, the spectra is slightly red. As we can see, the spectra of the wind stress cover a range of periods from month to centennial and higher, which is the range we are interested in, for short term barotropic adjustment and long term baroclinic adjustment.

NAO	$EOF_1$	$EOF_2$	$EOF_2$
Zonal	0.42	0.26	0.18
Meridional	0.5	0.2	0.11

SAM	$EOF_1$	$EOF_2$	$EOF_3$
Zonal	0.52	0.34	0.13
Meridional	0.85	0.08	0.06

Table 5.2.1: Variances of the first three EOFs for NCEP/NCAR windstress used to derive the NAO type and the SAM type artificial wind stress forcing.

## 5.2 Results

### 5.2.1 SAM perturbation

#### 5.2.1.1 How SAM affected SO

Figure 5.3 a) compares the spectra of applied wind perturbation to Kinetic Energy (KE) and potential energy (PE) through the ACC. Following the notation of Olbers and Lettmann (2007), we take  $(PE_n - PE_s)/f$  to represent the baroclinic flow through the Drake Passage, and  $KE_n - KE_s$  to represent the barotropic flow. At high frequencies (above  $0.03 \text{ year}^{-1}$ ), the flow through the Drake Passage is dominated by the barotropic flow. However, at the low frequency regime ( $0.001 \text{ year}^{-1}$  to  $0.01 \text{ year}^{-1}$ ), baroclinic flow dominates over the barotropic flow.

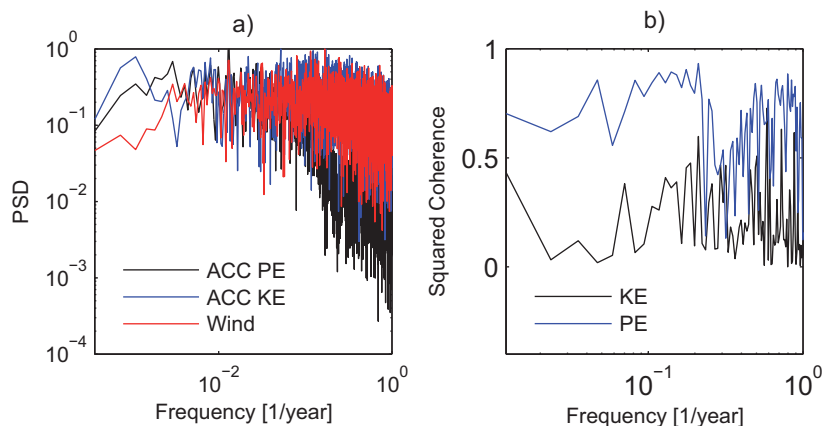


Figure 5.3: a) Normalised power spectral density of kinetic energy, potential energy and wind through the Drake passage; b) Squared coherence of kinetic energy and potential energy through the Drake passage with wind.

Figure 5.3 b) shows the coherence of PE and KE through the Drake Passage to wind variability. KE is moderately coherent with the wind variability at frequencies above  $0.01 \text{ year}^{-1}$ . PE and wind variability is highly coherent at low frequencies ( $0.01 \text{ year}^{-1}$  to  $0.2 \text{ year}^{-1}$ ). A loss of coherence is seen in the frequency range of  $0.2 \text{ year}^{-1}$  to  $0.8 \text{ year}^{-1}$  which is consistent with previous findings by Olbers and Lettmann (2007).

### 5.2.1.2 Wave adjustment in the Atlantic, Pacific and Indian Ocean

The SAM type AR1 wind anomaly applied in the Southern Ocean disturbs the barotropic and the baroclinic fields. This barotropic and baroclinic disturbance spreads across the Pacific, the Atlantic and the Indian Ocean basins (Ivchenko et al., 2004, 2006; Richardson et al., 2005).

Figure 5.4 a), c) and e) show the first EOF of the PE in the Pacific Ocean, Atlantic Ocean and Indian Ocean respectively, and b), d) and f) show their respective PC (Principal Components). Strongest variability in the Pacific Ocean is along the eastern coast Australia where the initial Kelvin wave carries the PE perturbation northward to the equator. Note that the boundary wave, referred to here is a Kelvin wave is actually a modified Kelvin-topographic wave. However, for the sake of simplicity, it is referred to as a Kelvin wave in the rest of this chapter. Along the western coast of North and South Amer-

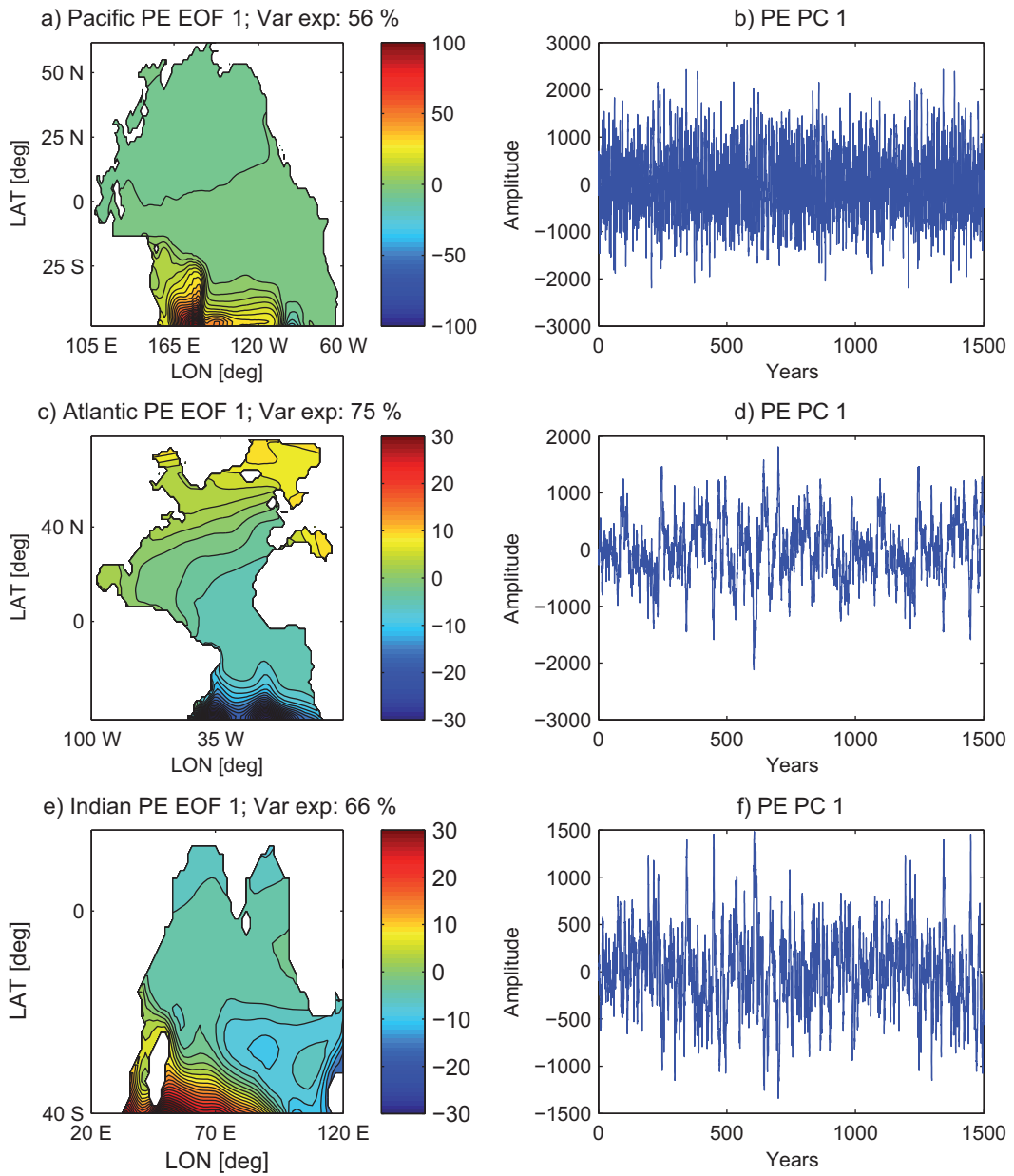


Figure 5.4: EOFs and the corresponding PCs of PE of a, b) Pacific Ocean, c, d) Atlantic Ocean and e, f) Indian Ocean

ica, the mode of variability is not as strong, as the propagating wave anomaly does not re-amplify (Johnson and Marshall, 2004). Due to the equatorial buffer (Johnson and Marshall, 2002), variability in the interior of the ocean from westward propagating Rossby waves is stronger in the Southern Pacific than in the Northern Pacific. The westward

propagating pattern of Rossby waves are clearly visible in the EOF, with the phase speed of Rossby wave decreasing as one moves polewards from the equator.

The leading mode in the Atlantic Ocean is of the Rossby waves. Largest variability is in the Southern Atlantic, with a Kelvin wave structure along the west coast of the Atlantic, and Rossby waves in the interior. As in the case of the Pacific Ocean, anomaly propagation in the North Atlantic is limited due to the equatorial buffer effect.

The equatorial response of the Indian Ocean seems to be limited due to the topography between Africa and Madagascar. The anomaly enters the Indian Ocean, along the Southern tip of South Africa, where it encounters the Northern branch of the sub-tropical gyre and the southward flowing Mozambique current. The leading mode of adjustment in the Indian Ocean is the Rossby wave. Figure 5.5 a) shows the EOF of the barotropic stream function and b) shows the corresponding PC.

Figure 5.6 shows the time taken by the baroclinic PE to propagate into the Atlantic, Indian and Pacific Ocean. Note that Figure 5.6 does not show the first arrival time of the signal. The time scale of adjustment is calculated by using lag cross correlation. The plot shows the time scales in which the variability is most strongly correlated with the applied perturbation at the Labrador sea.

In the Atlantic Ocean, the anomaly in PE initially propagates along the eastern coast of South America. In 5 months, the anomaly reaches the equator, then it turns eastward, crosses the equator within the next 5 months, and splits upon reaching the western coast of Africa. The Atlantic interior is adjusted through Rossby waves. The South Atlantic is adjusted within 3-4 years. The North Atlantic takes 5-6 months, as the Rossby waves have to travel longer distances.

Adjustment of the Indian Ocean takes place through Kelvin waves along the eastern coast of Africa within the first 2 years and the interior Indian Ocean is adjusted through Rossby waves in ~ 5 years. The tip of South Africa is at lower latitudes than the tip of South America. Thus, the time taken by the signal to reach the Indian equatorial region, and establish disturbance there is longer than it takes to reach the equatorial region in the

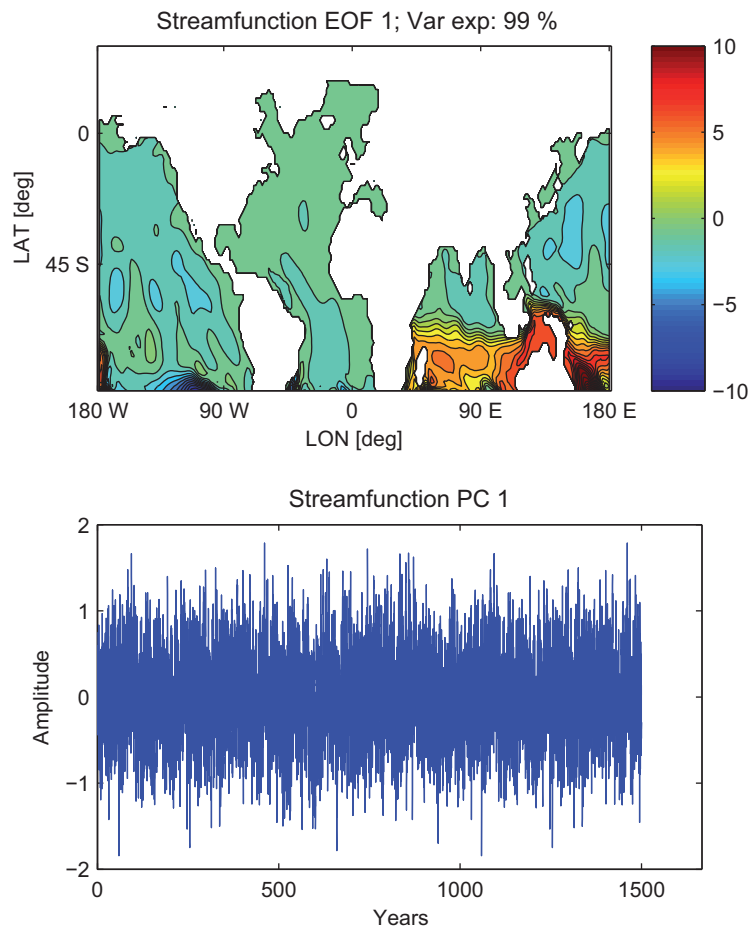


Figure 5.5: EOF and the corresponding PC of barotropic stream function

Atlantic Ocean.

The initial anomaly is introduced into the Pacific Ocean along the eastern coast of Australia, as a coastal Kelvin wave. The coastal Kelvin wave propagates northward until it reaches the equator, turns eastward at the equator and crosses the equator. This adjustment takes  $\sim 4$  years in the Pacific Ocean. The reason for longer adjustment period of the Kelvin wave could be discontinuous topography as opposed to the continuous Kelvin wave guide along the eastern coast of the South American continent in the Atlantic Ocean. The Rossby wave adjustment at the interior of the North Pacific takes upto 20 years.

Along  $50^\circ$  N, a front appears at the boundary between Southern Ocean and the Atlantic, Pacific and Indian basins. At this front, the westward propagating Rossby wave

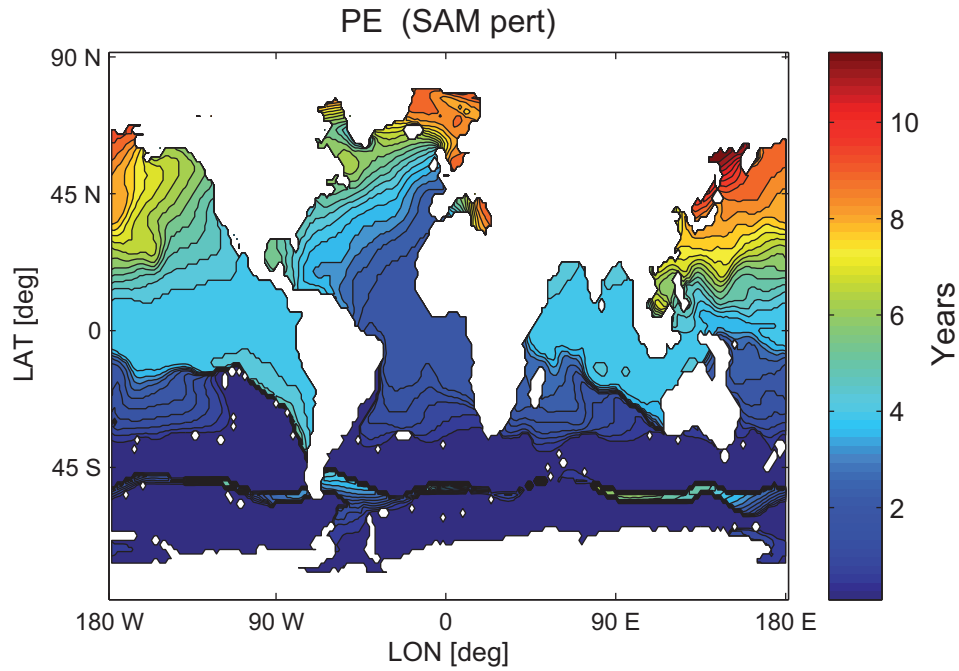


Figure 5.6: Lag plots showing the time taken for the PE to travel from the Southern Ocean to the other ocean basins. The time scale of adjustment is calculated by using lag cross correlation.

from the western coast of South America in the Pacific, Africa in the Atlantic and Australia in the Indian Ocean, meets the Southern Ocean where the perturbed wind forcing is applied. This shows that the initial baroclinic anomaly spreads into the Atlantic, Pacific and Indian basins as coastal Kelvin waves along eastern boundaries of the continents.

Figure 5.7 compares the power spectra of the KE and PE in all three ocean basins. Kinetic Energy spectra shows the fast response while potential energy spectra depicts the slow response which is caused by the slow uplifting of isopycnals. The high frequency regime (frequency over  $0.22 \text{ year}^{-1}$  or period shorter than 4 years) is dominated by the barotropic fields in the Indian and Pacific Ocean. For periods larger than 12-13 years, PE becomes more dominant in all the ocean basins. That is the time scale in which the initial baroclinic Kelvin wave is introduced into all three ocean basins (Figure 5.6). Figure 5.8 a) compares the power spectra of the PE in all three ocean basins. There is no noticeable difference between the spectra of the basins. The spectra for the Pacific Ocean is marginally more red than the Indian and the Atlantic Ocean. As mentioned earlier, this

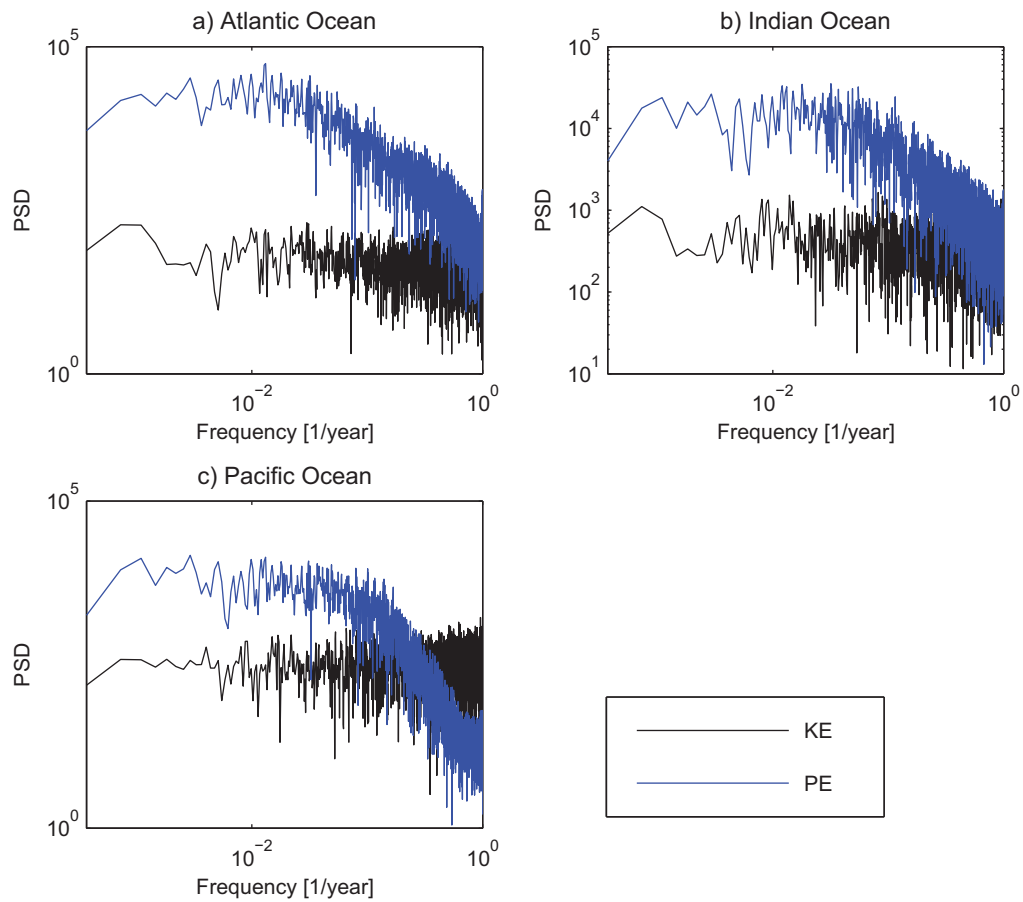


Figure 5.7: Power spectral density of KE and PE

could be due to longer adjustment times of the Pacific Ocean. The spectra of the field in all three oceans are almost identical (Figure 5.8 b).

Figure 5.9 a), b) and c) shows the coherence of KE and PE in the Atlantic, Pacific and Indian Ocean respectively, to the wind variability while d) compares the coherence of the baroclinic PE to the wind variability in the three basins. The KE has a few peaks in the frequency range of  $0.08 \text{ year}^{-1}$  to  $0.1 \text{ year}^{-1}$ . Strong coherence exist between the wind variability and the field at low frequencies ( $0.01 \text{ year}^{-1}$ -  $0.25 \text{ year}^{-1}$ ). A loss of coherence is seen in the frequency range of  $0.25 \text{ year}^{-1}$  to  $0.8 \text{ year}^{-1}$  in all the basins, which is seen in the coherence of the PE through Drake passage with the zonal wind field.

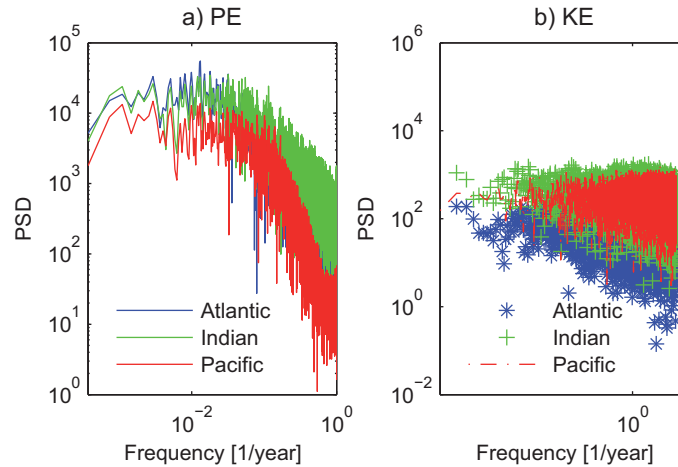


Figure 5.8: Power spectral density of a) PE and b) KE. [All psd in units of  $(m^3/s^2)/year^{-1}$ ]

### 5.2.2 NAO perturbation

The NAO type AR1 wind anomaly applied at the North Atlantic Ocean disturbs the barotropic and the baroclinic fields. This barotropic and baroclinic disturbance spreads across the South Atlantic, Indian, Pacific and Southern Ocean.

The propagation of PE anomaly takes the same route as it did in the Labrador Sea perturbation (Chapter 4). A coastally trapped wave (to be referred as Kelvin waves hereafter for the sake for simplicity, although the wave is a coastally trapped mixed topographic-Kelvin wave) is generated at the eastern coast of North America. This wave carries the anomaly southward to the equator. At the equator, the anomaly propagates eastward as an equatorial Kelvin wave. Upon reaching the West African coast, the wave splits and propagates polewards again as coastal Kelvin waves radiating westward propagating Rossby waves into the interior of the Atlantic Ocean. The signal propagating southward along the western coast of Africa, continues to propagate around the southern tip of Africa, Northward into the Indian Ocean. At the equator, the signal turns right and propagates eastwards, crosses the Indonesian archipelago, into the Pacific Ocean, crosses the equator until it reaches the eastern Pacific coast, where it splits and propagates poleward.

Figure 5.10 a), c) and e) show the first EOFs of the PE in the Pacific Ocean, Indian Ocean and Southern Ocean respectively, and b), d) and f) show the respective PCs. A

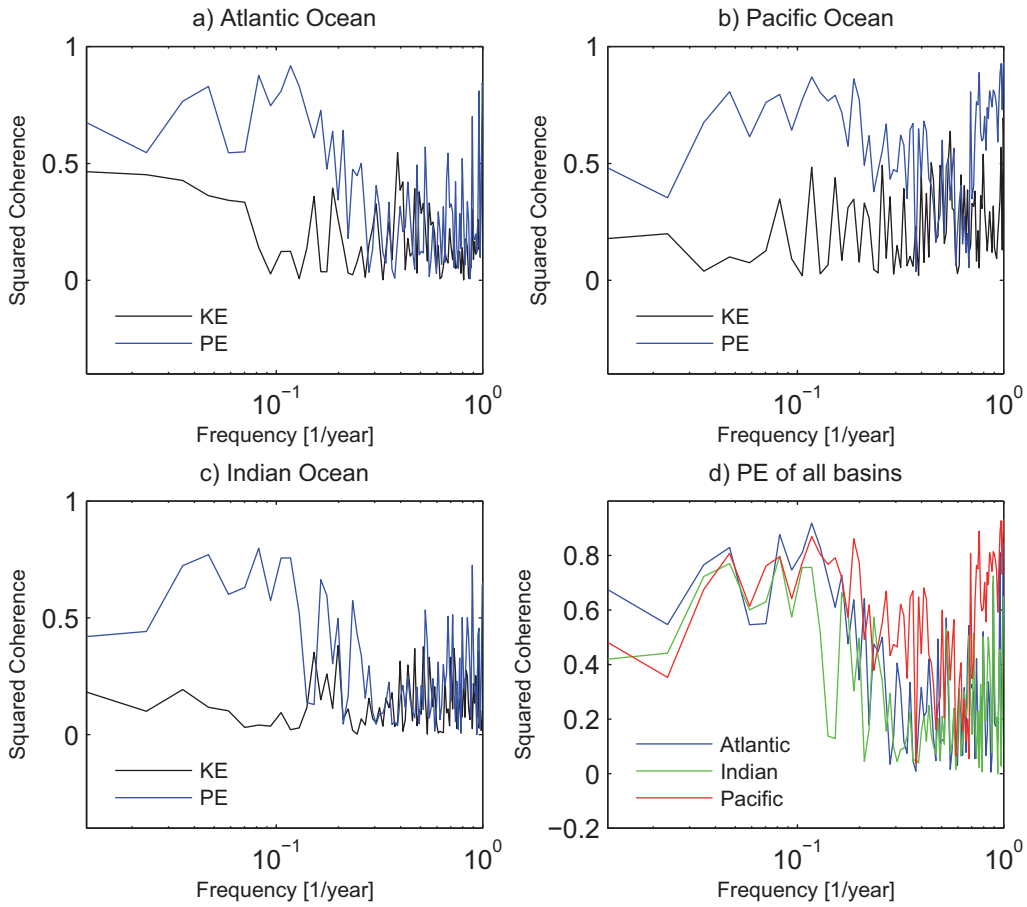


Figure 5.9: Squared coherence of kinetic energy and potential energy with wind variability in a) Atlantic Ocean, b) Pacific Ocean, c) Indian Ocean. d) Squared coherence of potential energy with wind variability in all three ocean basins

dominant mode of variability is not apparent in the Pacific Ocean. Traces of wavefront of a westward propagating Rossby wave can be seen in the Northern Hemisphere.

The anomaly enters the Indian Ocean, along the Southern tip of South Africa, it encounters the Northern branch of the sub-tropical gyre and the Mozambique current flowing Southward. As in the earlier cases, the equatorial response of the Indian Ocean seems to be limited due to the topography between Africa and Madagascar. The leading mode of adjustment in the Indian Ocean is the westward propagating Rossby wave.

The disturbance is carried into the Southern Ocean through westward propagating Rossby waves in the Atlantic, Pacific and Indian basin as shown by the leading mode. The leading mode here shows the perturbation is most severe in the Atlantic sector of the

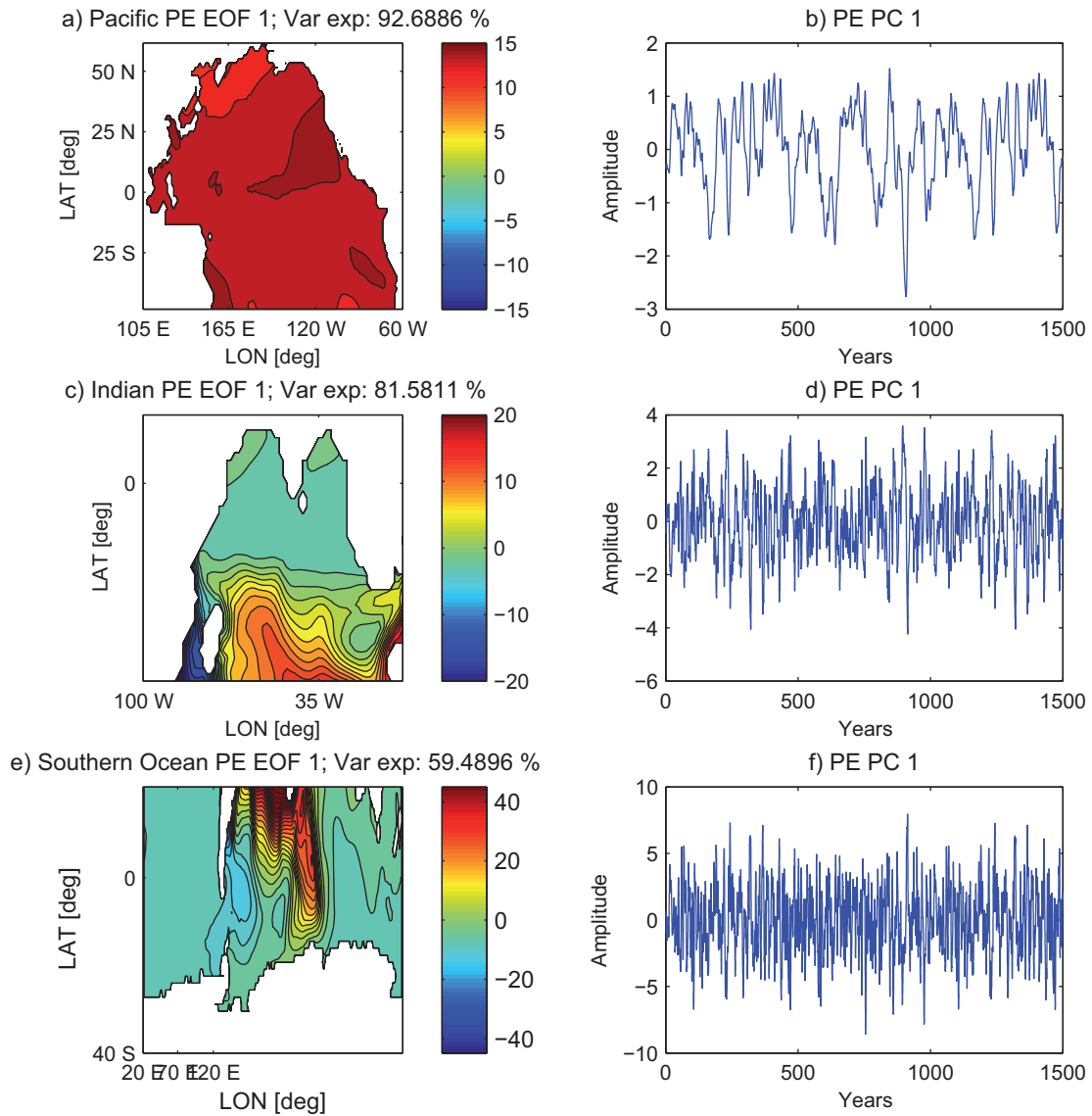


Figure 5.10: EOFs and the corresponding PCs of PE of a, b) Pacific Ocean, c, d) Indian Ocean and e, f) South Atlantic Ocean

Southern Ocean, as the signal originated in the Atlantic.

Figure 5.11 shows the time taken by the PE anomaly to propagate from the Atlantic Ocean to the Indian, Southern and the Pacific Ocean. Initial adjustment occurs through coastal and equatorial Kelvin waves. The anomaly reaches the equatorial Atlantic in 2-3 months. The disturbance propagates into the equatorial Indian Ocean in 1-2 years and

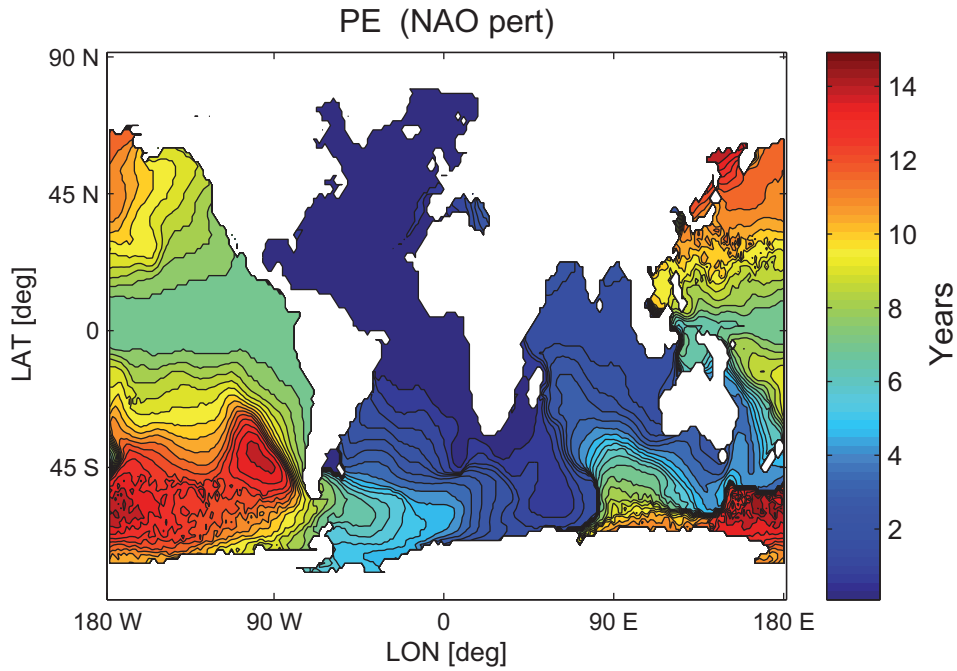


Figure 5.11: Lag plots showing the time taken for the PE anomaly to travel from the North Atlantic Ocean to the other ocean basins.

in 5 years into the Pacific. The anomaly is carried into the South Atlantic by Rossby waves and the adjustment process takes up 5 years. The interior Indian Ocean is adjusted through Rossby waves in ~ 5 years. Interior Pacific Ocean is adjusted through Rossby waves, and the adjustment takes 15-20 years.

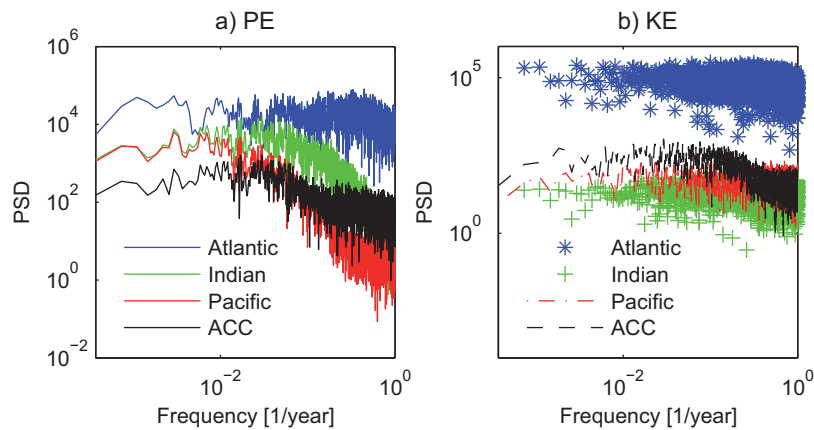


Figure 5.12: Power spectral density of KE and PE. [All psd in units of  $(m^3/s^2)/year^{-1}$ ]

Figure 5.12 a) compares the power spectra of the PE in all three ocean basins. As the signal moves farther away from the basin of origin (in this case, North Atlantic), the

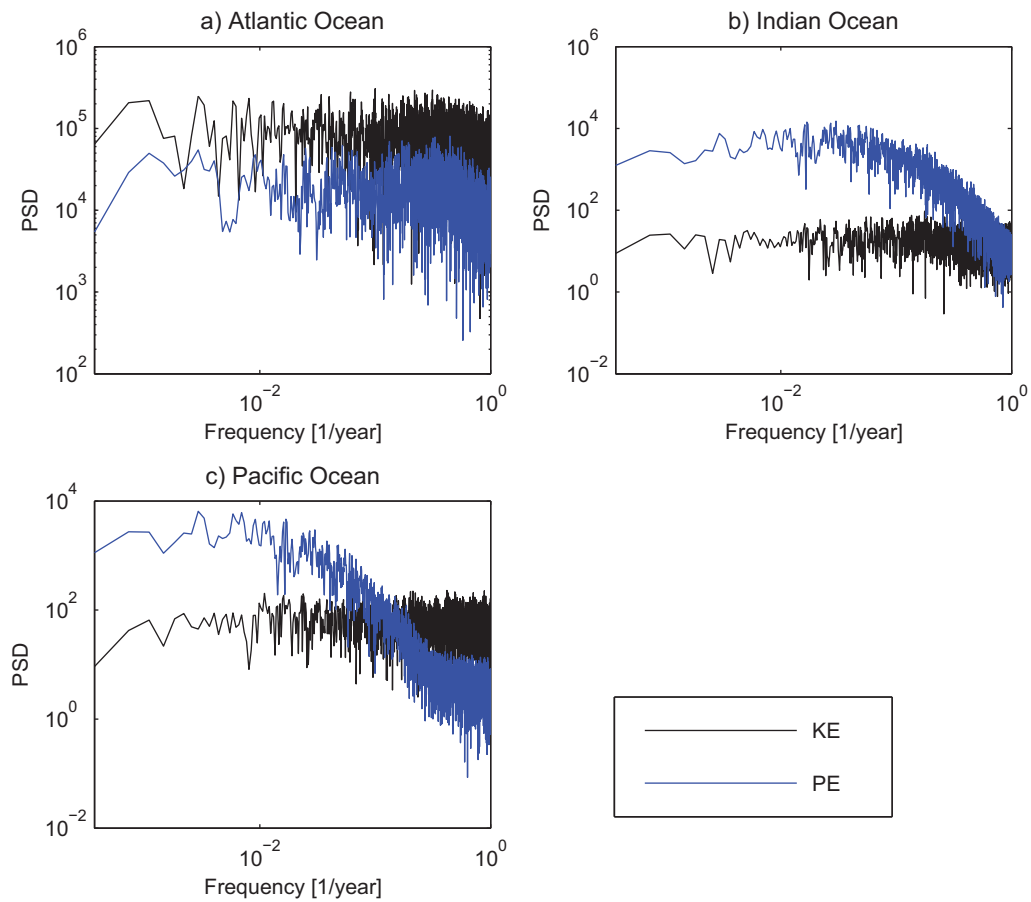


Figure 5.13: Power spectral density of a) PE and b) KE. [All psd in units of  $(m^3/s^2)/year^{-1}$ ]

dominance of the high frequency regime (frequency above  $0.038 year^{-1}$ ) decreases. High frequency variability is filtered out, whereas the low frequency variability persists on to other ocean basins, as we can see from the convergence of the spectra of the Pacific and Indian at the frequency range  $0.001 year^{-1}$  to  $0.01 year^{-1}$ . Figure 5.12 b) shows the spectra of the KE in the ocean basins. Barotropic influence is quite high at the basin of origin as we see from the high spectra of the Atlantic Ocean. However, the barotropic response on the other basins is limited due to stronger decay as we see from the low spectra of the Indian, Pacific and Southern Ocean.

Figure 5.13 compares the power spectra of KE and PE in all three ocean basins. The high frequency regime is dominated by the barotropic field in all the ocean basins. How-

ever, as the perturbation moves away from the North Atlantic into the Indian and then into the Pacific, the low frequency variability becomes more dominant. In the basin of origin, the Atlantic Ocean, the barotropic flow dominates in the whole frequency spectrum.

### **5.3 Conclusion**

Variability in large scale atmospheric circulation induces barotropic and baroclinic perturbation in the ocean circulation in daily to decadal and centennial time scales (Eden and Willebrand, 2001). As the temporal range of oceanic observation is relatively short, we present a study on the analysis of the timescales and pathways of barotropic and baroclinic wave adjustment in the ocean through a series of numerical simulations on a simple wind driven wave model with proper representation of topography (Olbers and Eden, 2003). An AR1 type 1500 years long artificial time series of wind stress is created using the leading mode of variability in atmospheric pressure in the northern and the southern hemisphere, namely NAO and SAO.

Our analysis of the impact of SAM type wind on the ACC is in agreement with previous such simulations by Olbers and Lettmann (2007). We observed that the barotropic field dominates the high frequency limit of variability in ACC transport through barotropic Rossby waves. However, for lower frequencies and on longer time scales, the isopycnals are disturbed, generating baroclinic Rossby waves. Hence, variability of ACC in the low frequency regime is dominated by baroclinic dynamics. We extend the analysis conducted by Olbers and Lettmann (2007) to global adjustment of barotropic and baroclinic fields.

The barotropic and baroclinic variability generated at the Southern Ocean propagates north into the Atlantic, Indian and Pacific Ocean. The barotropic component of the variability is transmitted within a few months. However, the amplitude of their barotropic variability is dominant only in the high frequency regime for the Atlantic and the Pacific Ocean.

The baroclinic variability is transmitted northwards though the western boundary

Kelvin wave pathway. As the Southern tip of South America is at a higher latitude as compared to the Southern tip of South Africa or Australia, it provides a smooth wave-guide for the coastal Kelvin wave to carry the variability northwards. The Southern tip of Africa is at lower latitudes, and the Kelvin wave carrying the perturbation into the Indian Ocean along the eastern coast of Africa encounters the Northern branch of the sub-tropical gyre and the Mozambique current flowing Southward. This leads to longer time scales of adjustment in the Indian Ocean. Pacific Ocean adjustment also takes longer due to discontinuous topography along the eastern coast of Australia.

The northern hemisphere of the Atlantic and Pacific Ocean are adjusted only through westward propagating Rossby waves. Hence adjustment time scales are in the order of decades.

The NAO type AR1 wind perturbation in the North Atlantic sector also leads to barotropic and baroclinic wave adjustment in all ocean basins. However, only the Atlantic Ocean is adjusted within a decade. The amplitude and time scales of baroclinic adjustment in the Indian and the Pacific Ocean is limited due to interaction with topography and circulation.

So, we can conclude that, in annual time scales, variabilities generated by wind perturbations are limited to the basin of origin. High frequency variability, with time scales comparable to the Kelvin wave propagation time, are contained within the hemisphere of origin due to interference. Topography also plays a role in limiting the response as Kelvin waves require a coastal wave guide to propagate and transmit anomaly from one basin to the other. Additionally, currents hinder wave propagation, as we saw limited response in the Indian Ocean from both the NAO type and SAM type perturbation due to the interaction of the waves with the Northern branch of the sub-tropical gyre and the Mozambique current flowing Southward.

Results are based on simulations on a model with simplified physics, identifying barotropic and baroclinic flow in the presence of topography, and a simple wind-driven circulation, representing the sub-tropical and sub-polar gyres and a stable ACC. How-

ever, the results hint in the general direction of how wind variability affects circulation by generating barotropic and baroclinic perturbations. The spatial extent of disturbance is governed by barotropic and baroclinic waves. At the low frequency regime of the spectra, the disturbance is transmitted through wave adjustment to other ocean basins. However, the time scales for significant adjustment to occur are in the order of decades. Results suggest that although fast teleconnection through Kelvin wave allows variability to transmit from one ocean basin to another within a few years, the amplitude decays significantly for high frequency variability. Significant perturbation of isopycnals in the 2nd and 3rd basin occurs only for low frequency variability, with periods of a few decades.

# Chapter 6

## Summary and Outlook

The aim of this PhD project was to provide new insights into oceanic teleconnections through wave mechanisms. A series of numerical simulations have been performed on models with triangular grids to understand how the ocean responds to buoyancy and wind stress perturbations, and the wave routes through which adjustment and teleconnections take place. The initial adjustment takes place through rapid coastally trapped waves and equatorial Kelvin waves. Westward propagating Rossby waves adjust the interior of the ocean. The key findings can be summarized as follows:

- The analytical study shows that on uniform triangular meshes, we obtain the theoretical prediction of Kelvin wave phase speed,  $c_p = 1$  if consistent mass matrices are used. With lumped mass matrices, the wave propagates faster than the theoretical limit on coarse meshes, similar to the B-grid case of Hsieh et al. (1983). The phase speed of Kelvin waves in numerical simulations is almost independent of resolution. There is some discrepancy between the measured and predicted speed, which by all probability is due to the stabilization.
- When the Rossby radius is resolved, the  $P_1 - P_1$  model used here produces the classical Kelvin wave, with an off-shore decay resembling the theoretical Kelvin wave guide. When the Rossby radius along the coast is not resolved, the Kelvin waveguide broadens. However, the structure is stable and the amplitude of the signal

reaching the eastern equator is not significantly affected by the low resolution.

- At low frequencies, the boundary waves ceases to be trapped and as the frequency is further lowered, they transform into short Rossby waves on the western coast and long Rossby waves on the eastern coast. Long Rossby waves are not affected by viscosity. In the presence of viscosity and the beta effect, trapping along the western boundary is again recovered. Propagation along the western boundary is still maintained through these modified boundary waves. Although these waves decay as they propagate alongshore, they propagate sufficiently fast and manage to play a role similar to the role of true Kelvin waves. Nevertheless, since the horizontal viscosity is selected so as to resolve the Munk boundary layer, low frequency localised waves propagating along the coast will be resolved by the models used.
- The oceanic response to high latitude buoyancy forcing depends on the frequency of the forcing itself. The spectra of response becomes redder as one moves away from the location of the perturbation. The quantity of water pumped into the thermocline in the Northern Hemisphere has to spread over a large area, which explains the increase in amplitude of response with decreasing frequency. For large periods (100 years and above), the response tends asymptotically towards a constant value as the transport from the Southern Ocean balances the forcing in the Northern Hemisphere.
- We found that in the presence of bottom topography, the time scales of adjustment are much longer than in *reduced gravity* setups. The presence of background mean circulation further hinders wave propagation, and plays a part in shaping the time scales of response. The amplitude of PE response in the Southern Hemisphere of the 1<sup>st</sup> basin (Atlantic Ocean) is reduced from 45 % in a *reduced gravity* model to 20 % upon the introduction of topography and circulation for large periods. The response in the 2<sup>nd</sup> and the 3<sup>rd</sup> basin is less than 20 %.
- The ocean reacts to low frequency atmospheric variability such as SAM over the

Southern Ocean and NAO in the North Atlantic Ocean. Adjustment takes place through boundary waves and Rossby waves. However, the amplitude of ocean adjustment solely responding to wind stress variability is strongest only on the basin where the perturbation occurs. The baroclinic response in terms of isopycnal displacement is strongest in the hemisphere where the perturbation is applied. The amplitude in the opposite hemisphere is weakened by the equatorial buffer mechanism. The baroclinic response of the ocean is found to be stronger for buoyancy perturbation compared to wind stress perturbation.

As mentioned earlier in the introduction, wave adjustment in the ocean presents one mechanism of rapid anomaly (in the sense of thermocline uplifting or deepening) transmission in time scales of a few years. This can lead to changes in SST fields which have serious consequences for local weather and climate. This thesis worked towards finding a modeling tool and using it to understand and explain the mechanism through which this wave adjustment due to buoyancy and wind forcing takes place. The models used for this work are based on simplified physics. A natural next step is to extend this study to complex earth system models towards understanding the impact the ocean may have on other components of the climate system through wave mechanism processes. Also, our preliminary modeling results suggest that interaction of waves with topography and circulation hampers wave propagation, and has an impact on the time scales and amplitude of adjustment. It is important to develop this study towards having an improved physical understanding of how these interactions manifest themselves, enabling us to understand the role of ocean waves during potential future rapid climate change, in response to anthropogenic warming.



# Bibliography

- Aagaard, K., 1968: Temperature variations in the greenland sea deep-water. *Deep Sea Research and Oceanographic Abstracts*, **15 (3)**, 281 – 296, doi:10.1016/0011-7471(68)90006-5, URL <http://www.sciencedirect.com/science/article/pii/0011747168900065>.
- Bacon, S., 1998: Decadal variability in the outflow from the nordic seas to the deep atlantic ocean. *Nature*, **394 (6696)**, 871–874, URL <http://dx.doi.org/10.1038/29736>.
- Barber, D. C., et al., 1999: Forcing of the cold event of 8,200 years ago by catastrophic drainage of laurentide lakes. *Nature*, **400 (6742)**, 344–348, URL <http://dx.doi.org/10.1038/22504>.
- Broecker, W., 1991: The great ocean conveyor. *Oceanography*, **4**, 79–89.
- Cessi, P., K. Bryan, and R. Zhang, 2004: Global seiching of thermocline waters between the atlantic and the indian-pacific ocean basins. *Geophys. Res. Lett.*, **31 (4)**, L04 302–, URL <http://dx.doi.org/10.1029/2003GL019091>.
- Chelton, D. B. and M. G. Schlax, 1996: Global observations of oceanic rossby waves. *Science*, **272 (5259)**, 234–238, doi:10.1126/science.272.5259.234, URL <http://www.sciencemag.org/content/272/5259/234.abstract>, <http://www.sciencemag.org/content/272/5259/234.full.pdf>.

- Cipollini, P., D. Cromwell, P. G. Challenor, and S. Raffaglio, 2001: Rossby waves detected in global ocean colour data. *Geophys. Res. Lett.*, **28** (2), 323–326, URL <http://dx.doi.org/10.1029/1999GL011231>.
- Clarke, A. J. and C. Shi, 1991: Critical frequencies at ocean boundaries. *J. Geophys. Res.*, **96** (C6), 10731–10738, URL <http://dx.doi.org/10.1029/91JC00933>.
- Clarke, R., J. H. Swift, J. L. Reid, and K. Koltermann, 1990: The formation of greenland sea deep water: double diffusion or deep convection? *Deep Sea Research Part A. Oceanographic Research Papers*, **37** (9), 1385 – 1424, doi:10.1016/0198-0149(90)90135-I, URL <http://www.sciencedirect.com/science/article/pii/019801499090135I>.
- Dansgaard, W., et al., 1993: Evidence for general instability of past climate from a 250-kyr ice-core record. *Nature*, **364** (6434), 218–220, URL <http://dx.doi.org/10.1038/364218a0>.
- Davey, M. K., W. W. Hsieh, and R. C. Wajsowicz, 1983: The free kelvin wave with lateral and vertical viscosity. *J. Phys. Oceanogr.*, **13** (12), 2182–2191, doi:10.1175/1520-0485(1983)013<2182:TFKWVL>2.0.CO;2, URL [http://dx.doi.org/10.1175/1520-0485\(1983\)013<2182:TFKWVL>2.0.CO;2](http://dx.doi.org/10.1175/1520-0485(1983)013<2182:TFKWVL>2.0.CO;2).
- Delworth, T., S. Manabe, and R. J. Stouffer, 1993: Interdecadal variations of the thermohaline circulation in a coupled ocean-atmosphere model. *J. Climate*, **6** (11), 1993–2011, doi:10.1175/1520-0442(1993)006<1993:IVOTTC>2.0.CO;2, URL [http://dx.doi.org/10.1175/1520-0442\(1993\)006<1993:IVOTTC>2.0.CO;2](http://dx.doi.org/10.1175/1520-0442(1993)006<1993:IVOTTC>2.0.CO;2).
- Dickson, B., J. Meincke, I. Vassie, J. Jungclauss, and S. Osterhus, 1999: Possible predictability in overflow from the denmark strait. *Nature*, **397** (6716), 243–246, URL <http://dx.doi.org/10.1038/16680>.
- Dickson, J. M. S. A. M., R. R. and A. J. Lee, 1988: The "great salinity anomaly" in the northern north atlantic 1968-1982. *Prog. Oceanography*, **20**, 103–151.

- Dickson, R. . and J. Brown, 1994: The production of north atlantic deep water: Sources, rates, and pathways. *J. Geophys. Res.*, **12**, 319–341.
- Dickson, R., J. Lazier, J. Meincke, P. Rhines, and J. Swift, 1996: Long-term coordinated changes in the convective activity of the north atlantic. *Progress In Oceanography*, **38** (3), 241–295, doi:10.1016/S0079-6611(97)00002-5, URL <http://www.sciencedirect.com/science/article/pii/S0079661197000025>.
- Dickson, R. R., E. M. Gmitrowicz, and A. J. Watson, 1990: Deep-water renewal in the northern north atlantic. *Nature*, **344** (6269), 848–850, URL <http://dx.doi.org/10.1038/344848a0>.
- Doescher, R., C. W. Baeñning, and P. Herrmann, 1994: Response of circulation and heat transport in the north atlantic to changes in thermohaline forcing in northern latitudes: A model study. *J. Phys. Oceanogr.*, **24** (11), 2306–2320, doi:10.1175/1520-0485(1994)024<2306:ROCAHT>2.0.CO;2, URL [http://dx.doi.org/10.1175/1520-0485\(1994\)024<2306:ROCAHT>2.0.CO;2](http://dx.doi.org/10.1175/1520-0485(1994)024<2306:ROCAHT>2.0.CO;2).
- Eden, C. and J. Willebrand, 2001: Mechanism of interannual to decadal variability of the north atlantic circulation. *J. Climate*, **14** (10), 2266 – 2280, doi:10.1175/1520-0442(2001)014<2266:MOITDV>2.0.CO;2, URL [http://dx.doi.org/10.1175/1520-0442\(2001\)014<2266:MOITDV>2.0.CO;2](http://dx.doi.org/10.1175/1520-0442(2001)014<2266:MOITDV>2.0.CO;2).
- Fevrier, S., J. Sirven, and C. Herbaut, 2007: Interaction of a coastal kelvin wave with the mean state in the gulf stream separation area. *J. Phys. Oceanogr.*, **37** (6), 1429–1444, doi:10.1175/JPO3062.1, URL <http://dx.doi.org/10.1175/JPO3062.1>.
- Gill, A., 1982: *Atmosphere-Ocean Dynamics, International Geophysics Series*.
- Haekkinen, S., 1999: A simulation of thermohaline effects of a great salinity anomaly. *J. Climate*, **12** (6), 1781–1795, doi: 10.1175/1520-0442(1999)012<1781:ASOTEO>2.0.CO;2, URL [http://dx.doi.org/10.1175/1520-0442\(1999\)012<1781:ASOTEO>2.0.CO;2](http://dx.doi.org/10.1175/1520-0442(1999)012<1781:ASOTEO>2.0.CO;2).

- Haekkinen, S., 2001: Variability in sea surface height: A qualitative measure for the meridional overturning in the north atlantic. *J. Geophys. Res.*, **106** (C7), 13 837–13 848, URL <http://dx.doi.org/10.1029/1999JC000155>.
- Hsieh, W. W. and K. Bryan, 1996: Redistribution of sea level rise associated with enhanced greenhouse warming: a simple model study. Springer Berlin / Heidelberg, URL <http://dx.doi.org/10.1007/BF00207937>, 535–544 pp., URL <http://dx.doi.org/10.1007/BF00207937>.
- Hsieh, W. W., M. K. Davey, and R. C. Wajsowicz, 1983: The free kelvin wave in finite-difference numerical models. *J. Phys. Oceanogr.*, **13** (8), 1383–1397, doi:10.1175/1520-0485(1983)013<1383:TFKWIF>2.0.CO;2, URL [http://dx.doi.org/10.1175/1520-0485\(1983\)013<1383:TFKWIF>2.0.CO;2](http://dx.doi.org/10.1175/1520-0485(1983)013<1383:TFKWIF>2.0.CO;2).
- Huang, R. X., M. A. Cane, N. Naik, and P. Goodman, 2000: Global adjustment of the thermocline in response to deepwater formation. *Geophys. Res. Lett.*, **27** (6), 759–762, URL <http://dx.doi.org/10.1029/1999GL002365>.
- Ivchenko, V. O., V. B. Zalesny, and M. R. Drinkwater, 2004: Can the equatorial ocean quickly respond to antarctic sea ice/salinity anomalies? *Geophys. Res. Lett.*, **31** (15), L15 310–, URL <http://dx.doi.org/10.1029/2004GL020472>.
- Ivchenko, V. O., V. B. Zalesny, M. R. Drinkwater, and J. Schröter, 2006: A quick response of the equatorial ocean to antarctic sea ice/salinity anomalies. *J. Geophys. Res.*, **111** (C10), C10018–, URL <http://dx.doi.org/10.1029/2005JC003061>.
- Jacobs, G. A., H. E. Hurlburt, J. C. Kindle, E. J. Metzger, J. L. Mitchell, W. J. Teague, and A. J. Wallcraft, 1994: Decade-scale trans-pacific propagation and warming effects of an el nino anomaly. *Nature*, **370** (6488), 360–363, URL <http://dx.doi.org/10.1038/370360a0>.

- Jacobson, A. R. and J. L. Spiesberger, 1998: Observations of el niño-southern oscillation induced rossby waves in the northeast pacific using in situ data. *J. Geophys. Res.*, **103 (C11)**, 24 585–24 596, URL <http://dx.doi.org/10.1029/98JC02444>.
- Johnson, H. L. and D. P. Marshall, 2002: A theory for the surface atlantic response to thermohaline variability. *J. Phys. Oceanogr.*, **32 (4)**, 1121 – 1132, doi:10.1175/1520-0485(2002)032<1121:ATFTSA>2.0.CO;2, URL [http://dx.doi.org/10.1175/1520-0485\(2002\)032<1121:ATFTSA>2.0.CO;2](http://dx.doi.org/10.1175/1520-0485(2002)032<1121:ATFTSA>2.0.CO;2).
- Johnson, H. L. and D. P. Marshall, 2004: Global teleconnections of meridional overturning circulation anomalies. *J. Phys. Oceanogr.*, **34 (7)**, 1702 –1722, doi:10.1175/1520-0485(2004)034<1702:GTOMOC>2.0.CO;2, URL [http://dx.doi.org/10.1175/1520-0485\(2004\)034<1702:GTOMOC>2.0.CO;2](http://dx.doi.org/10.1175/1520-0485(2004)034<1702:GTOMOC>2.0.CO;2).
- Kawase, M., 1987: Establishment of deep ocean circulation driven by deep-water production. *J. Phys. Oceanogr.*, **17 (12)**, 2294–2317, doi:10.1175/1520-0485(1987)017<2294:EODOCD>2.0.CO;2, URL [http://dx.doi.org/10.1175/1520-0485\(1987\)017<2294:EODOCD>2.0.CO;2](http://dx.doi.org/10.1175/1520-0485(1987)017<2294:EODOCD>2.0.CO;2).
- Knutti, R., J. Fluckiger, T. F. Stocker, and A. Timmermann, 2004: Strong hemispheric coupling of glacial climate through freshwater discharge and ocean circulation. *Nature*, **430 (7002)**, 851–856, URL <http://dx.doi.org/10.1038/nature02786>.
- Liu, Z., L. Wu, and E. Bayler, 1999: Rossby wave: Coastal kelvin wave interaction in the extratropics. part i: Low-frequency adjustment in a closed basin. *J. Phys. Oceanogr.*, **29 (9)**, 2382 – 2404, doi:10.1175/1520-0485(1999)029<2382:RWCKWI>2.0.CO;2, URL [http://dx.doi.org/10.1175/1520-0485\(1999\)029<2382:RWCKWI>2.0.CO;2](http://dx.doi.org/10.1175/1520-0485(1999)029<2382:RWCKWI>2.0.CO;2).
- Lohmann, G., 2003: Atmospheric and oceanic freshwater transport during weak atlantic overturning circulation. *Tellus*, **55**, 438–449.

- Macdonald, A. M. and C. Wunsch, 1996: An estimate of global ocean circulation and heat fluxes. *Nature*, **382**, 436 – 439.
- Manabe, S. and R. J. Stouffer, 1993: Century-scale effects of increased atmospheric CO<sub>2</sub> on the ocean-atmosphere system. *Nature*, **364 (6434)**, 215–218, URL <http://dx.doi.org/10.1038/364215a0>.
- Massmann, S., A. Androsov, and S. Danilov, 2010: Intercomparison between finite element and finite volume approaches to model north sea tides. *Continental Shelf Research*, **30 (6)**, 680–691, doi:10.1016/j.csr.2009.07.004, URL <http://www.sciencedirect.com/science/article/pii/S0278434309002118>.
- McCalpin, J. D., 1995: Rossby wave generation by poleward propagating kelvin waves: The midlatitude quasigeostrophic approximation. *J. Phys. Oceanogr.*, **25 (6)**, 1415–1425, doi:10.1175/1520-0485(1995)025<1415:RWGBPP>2.0.CO;2, URL [http://dx.doi.org/10.1175/1520-0485\(1995\)025<1415:RWGBPP>2.0.CO;2](http://dx.doi.org/10.1175/1520-0485(1995)025<1415:RWGBPP>2.0.CO;2).
- Meinke, J., 1990: The greenland sea interannual variability. *ICES CM 1990/C: 17*.
- Meyers, S. D., A. Melsom, G. T. Mitchum, and J. J. O'Brien, 1998: Detection of the fast kelvin wave teleconnection due to el niño-southern oscillation. *J. Geophys. Res.*, **103 (C12)**, 27 655 –27 663, URL <http://dx.doi.org/10.1029/98JC02402>.
- Milliff, R. F. and J. C. McWilliams, 1994: The evolution of boundary pressure in ocean basins. *J. Phys. Oceanogr.*, **24 (6)**, 1317–1338, doi:10.1175/1520-0485(1994)024<1317:TEOBPI>2.0.CO;2, URL [http://dx.doi.org/10.1175/1520-0485\(1994\)024<1317:TEOBPI>2.0.CO;2](http://dx.doi.org/10.1175/1520-0485(1994)024<1317:TEOBPI>2.0.CO;2).
- Olbers and Eden, 2003: A simplified general circulation model for a baroclinic ocean with topography. part i: theory, waves, and wind-driven circulations. *J. Phys. Oceanogr.*, **33**, 2719 – 2737.
- Olbers, D. and K. Lettmann, 2007: Barotropic and baroclinic processes in the transport variability of the antarctic circumpolar current. *Ocean*

- Dynamics*, **57** (6), 559–578, doi:doi:10.1007/s10236-007-0126-1, URL <http://www.ingentaconnect.com/content/klu/10236/2007/00000057/00000006/00000126>.
- Olbers, D., K. Lettmann, and R. Timmermann, 2007a: Six circumpolar currents on the forcing of the antarctic circumpolar current by wind and mixing. *Ocean Dynamics*, **57**, 12–31, URL <http://dx.doi.org/10.1007/s10236-006-0087-9>, 10.1007/s10236-006-0087-9.
- Olbers, D., K. Lettmann, and J.-O. Wolff, 2007b: Wave-induced topographic formstress in baroclinic channel flow. *Ocean Dynamics*, **57**, 511–530, URL <http://dx.doi.org/10.1007/s10236-007-0109-2>, 10.1007/s10236-007-0109-2.
- Pacanowski, R. C., 1995: Mom 2 documentation, users guide and reference manual. *GFDL Ocean Group Tech. Report*, 232.
- Peixoto, J. P. and A. H. Oort, 1992: *Physics of climate / Jose P. Peixoto and Abraham H. Oort ; foreword by Edward N. Lorenz*. American Institute of Physics, New York :, xxxix, 520 p. : pp.
- Polo, I., A. Lazar, B. Rodriguez-Fonseca, and S. Arnault, 2008: Oceanic kelvin waves and tropical atlantic intraseasonal variability: 1. kelvin wave characterization. *J. Geophys. Res.*, **113** (C7), C07009–, URL <http://dx.doi.org/10.1029/2007JC004495>.
- Rahmstorf, S., 2006: Thermohaline ocean circulation. *Encyclopedia of Quaternary Sciences*.
- Richardson, G., M. R. Wadley, K. J. Heywood, D. P. Stevens, and H. T. Banks, 2005: Short-term climate response to a freshwater pulse in the southern ocean. *Geophys. Res. Lett.*, **32** (3), L03702–, URL <http://dx.doi.org/10.1029/2004GL021586>.
- Roemmich and Wunsch, 1985: Two transatlantic sections: meridional circulation and heat flux in the subtropical north atlantic ocean. *Deep Sea Research Part A. Oceanographic Research Papers*, **32**, 619 – 664.

- Schlosser, B. G. R. M., P. and R. Bayer, 1991: Reduction of deepwater formation in the greenland sea during the 1980s: Evidence from tracer data. *Science*, **251** (4997), 1054–1056, URL <http://www.sciencemag.org/content/251/4997/1054.abstract>.
- Thompson, D. W. J. and J. M. Wallace, 2000: Annular modes in the extratropical circulation. part i: Month-to-month variability\*. *J. Climate*, **13** (5), 1000–1016, doi:10.1175/1520-0442(2000)013<1000:AMITEC>2.0.CO;2, URL [http://dx.doi.org/10.1175/1520-0442\(2000\)013<1000:AMITEC>2.0.CO;2](http://dx.doi.org/10.1175/1520-0442(2000)013<1000:AMITEC>2.0.CO;2).
- Timmermann, A., U. Krebs, F. Justino, H. Goosse, and T. Ivanochko, 2005: Mechanisms for millennial-scale global synchronization during the last glacial period. *Paleoceanography*, **20** (4), PA4008–, URL <http://dx.doi.org/10.1029/2004PA001090>.
- Timmermann, A. S. U. K. H. G., A., 2005: Enso suppression due to weakening of the north atlantic thermohaline circulation. *Journal of Climate*, **18**, 3122 – 3139.
- Vellinga, M. and R. A. Wood, 2002: Global climatic impacts of a collapse of the atlantic thermohaline circulation. *Climatic Change*, **54**, 251–267, URL <http://dx.doi.org/10.1023/A:1016168827653>, 10.1023/A:1016168827653.
- Wajsowicz, R. C. and A. E. Gill, 1986: Adjustment of the ocean under buoyancy forces. part i: The role of kelvin waves. *J. Phys. Oceanogr.*, **16** (12), 2097–2114, doi:10.1175/1520-0485(1986)016<2097:AOTOUB>2.0.CO;2, URL [http://dx.doi.org/10.1175/1520-0485\(1986\)016<2097:AOTOUB>2.0.CO;2](http://dx.doi.org/10.1175/1520-0485(1986)016<2097:AOTOUB>2.0.CO;2).
- Walker, G. T. and E. W. Bliss, 1932: World weather v. *Mem. Roy. Met. Soc.*, **4**, 53 – 84.
- Wallace, D. S., John M.; Gutzler, 1981: Teleconnections in the geopotential height field during the northern hemisphere winter. *Monthly Weather Review*, **109**, 784.

# List of Figures

1.1	Ocean thermohaline circulation with sinking site and upwelling sites marked (Broecker, 1991; Rahmstorf, 2006). . . . .	2
2.1	Properties of planetary wave dispersion relation(Gill, 1982) . . . . .	9
2.2	Location of the velocity components $u$ and $v$ , and the sea surface displacement $\eta$ Arakawa $B$ and $C$ grids. . . . .	10
2.3	Shallow-water model with moving surface layer and infinitely deep, motionless, lower layer. Thermohaline overturning is represented by a prescribed outflow from the surface layer on the northern boundary. Different model domains are used for different experiments and they are described in the corresponding setup sections in this chapter. . . . .	11
2.4	Location of the velocity components $u$ and $v$ , and the sea surface displacement $h$ in a $P_1 - P_1$ grid. . . . .	12
2.5	a) North Atlantic mesh; b) Magnified Gulf of Mexico of the North Atlantic mesh; c) Magnified region of the mesh without Gulf of Mexico . . . . .	14
2.6	Two layer ocean to show the derivation of the buoyancy forcing in BarBI . . .	16
2.7	a) Barotropic streamfunction [Sv] and b) Baroclinic potential [ $m^3/s^2$ ] energy after 200 years of forcing BarBI with a time mean wind stress . . . . .	18
2.8	ACC transport in BarBI after switching on the time mean wind stress . . . . .	19
2.9	Steady state of all the ocean basins after 200 years of forcing BarBI with a time mean windstress $\bar{\tau}(x,y)$ , in units of Sv. . . . .	20

3.1	Location of the velocity components $u$ and $v$ , and the sea surface displacement $h$ in a $P_1 - P_1$ grid. . . . .	23
3.2	Kelvin wave adjustment in the North Atlantic after the SSH perturbation is turned on at the north-west corner of the domain. Wave propagates as a SSH (isopycnal displacement in reduced gravity set up) signal, with unit of meters. . . . .	28
3.3	Rossby wave adjustment. Wave propagates as a SSH (isopycnal displacement in reduced gravity set up) signal, with unit of meters. . . . .	29
3.4	Evolution of coastal Kelvin waves and Rossby waves with time on various meshes at 45 N. Note that there is only marginal sensitivity to resolution for the Rossby waves. . . . .	31
3.5	Evolution of coastal Kelvin waves and Rossby waves with time on various meshes at 15 N. Note that there is only marginal sensitivity to resolution for the Rossby waves. . . . .	32
3.6	Evolution of coastal Kelvin waves and Rossby waves with time on various meshes in the 45 S. Note that there is only marginal sensitivity to resolution for the Rossby waves. . . . .	33
3.7	Evolution of coastal Kelvin waves and Rossby waves with time on various meshes in the 15 S. Note that there is only marginal sensitivity to resolution for the Rossby waves. . . . .	34
3.8	Off shore decay of the coastally trapped Kelvin wave amplitude for varying viscosity at 45 N . . . . .	41
3.9	Off shore decay of the coastally trapped Kelvin wave amplitude for varying viscosity at 15° N. Arrival of westward propagating Rossby waves front can be seen 125 - 200 km off the coast. . . . .	42
3.10	Amplitude of the waves as it propagates along the western boundary from the north-west corner of the domain to the equator in various meshes. Insufficient viscosity on the course meshes leads to oscillations. . . . .	43

3.11	Amplitude of the waves as it propagates along the eastern boundary from the north-east corner of the domain to the equator in various meshes. Insufficient viscosity on the course meshes leads to oscillations. . . . .	44
3.12	Off shore decay of the coastally trapped Kelvin wave amplitude for varying resolution at 45° N . . . . .	47
3.13	Off shore decay of the coastally trapped Kelvin wave amplitude for varying resolution at 15° N. Arrival of westward propagating Rossby waves front can be seen 125 - 200 km off the coast. . . . .	48
3.14	Amplitude of the waves as it propagates along the western boundary from the north-west corner of the domain to the equator in various meshes . . . . .	49
4.1	Time evolution of the wave adjustment in the North Atlantic after the perturbation of thermohaline is switched on in the Labrador Sea. Wave propagates as a thermocline displacement, with unit of meters. . . . .	56
4.2	a) Amplitude of thermocline's displacement at the eastern coast 10° north of the equator for the three different mesh. b) Amplitude of the thermocline displacements at the eastern coast 10° north of the equator for perturbation of different frequencies . . . . .	57
4.3	Power spectral density of a) PE from the <i>reduced gravity</i> experiment units of $m/year^{-1}$ , b) PE from the BarBI no-spin up experiment and c) PE from the BarBI with spin-up experiment in units of $(m^3/s^2)/year^{-1}$ . . . . .	61
4.4	Power spectral density of kinetic energy and potential energy of Atlantic Ocean BarBI in the a) no spin-up and b) with spin-up experiments, and Pacific Ocean in c) no spin-up and d) with spin-up experiments. Slopes for the high frequency and low frequency part of the spectra are shown with matching color as the color of trend line. [All psd in units of $(m^3/s^2)/year^{-1}$ ] . . . . .	62
4.5	Squared coherence of a) SSH from the <i>FEOM</i> experiment , b) Potential energy from the BarBI no-spin up experiment and c) Potential energy from the BarBI with spin-up experiment . . . . .	65

4.6	EOFs and the corresponding PCs of thermocline displacement of a, b) Atlantic Ocean, c, d) Indian Ocean and e, f) Pacific Ocean from the <i>reduced gravity</i> experiment. The location of the prescribed forcing area (Labrador Sea) is removed before calculating the EOFs. . . . .	67
4.7	EOFs and the corresponding PCs of thermocline displacement of the Southern Ocean from the <i>reduced gravity</i> experiment . . . . .	68
4.8	EOFs and the corresponding PCs of thermocline displacement of a, b) Atlantic Ocean, c, d) Indian Ocean and e, f) Pacific Ocean from the BarBI <i>no spin-up</i> experiment. The location of the prescribed forcing area (Labrador Sea) is removed before calculating the EOFs. . . . .	70
4.9	EOF and the corresponding PC of thermocline displacement of the Southern Ocean from the BarBI <i>no spin-up</i> experiment . . . . .	71
4.10	EOFs and the corresponding PCs of thermocline displacement of a, b) Atlantic Ocean, c, d) Indian Ocean and e, f) Pacific Ocean from the BarBI <i>with spin-up</i> experiment. The location of the prescribed forcing area (Labrador Sea) is removed before calculating the EOFs. . . . .	73
4.11	EOF and the corresponding PC of thermocline displacement of the Southern Ocean from the BarBI in the <i>with spin-up</i> experiment . . . . .	74
4.12	Spectrum of PE response to the buoyancy perturbation in Labrador Sea at the a) Atlantic Ocean, b) Indian Ocean, c) Pacific Ocean for the reduced gravity, no spin-up and with spin-up experiments. . . . .	76
4.13	Spectrum of PE and KE response to the buoyancy perturbation in Labrador Sea at the a) Atlantic Ocean for the no spin-up experiment, b) Pacific Ocean for the no spin-up experiment, c) Atlantic Ocean for the with spin-up experiment, d) Pacific Ocean for the with spin-up experiment. . . . .	77

4.14	Lag plots showing the time taken for the perturbation to travel from the Labrador Sea to the other ocean basins. a) shows the time scales in the <i>reduced gravity</i> experiment b) and c) shows the propagation time of the barotropic streamfunction and PE for the <i>no spin-up</i> setup respectively; d) and e) shows the propagation time of the barotropic streamfunction and PE for the <i>no spin-up</i> setup respectively <i>with spin-up</i> experiments; f) shows the difference in the time scales of propagation of PE between the <i>with spin-up</i> and <i>no spin-up</i> experiments; . . . . .	79
5.1	First three EOFs (Empirical Orthogonal Functions) of wind stress over the North Atlantic used to develop the NAO type long term wind stress time series, with units $10^{-2}m^2/s^2$ . . . . .	84
5.2	First three EOFs of zonal component of the wind stress over the Southern Ocean used to develop the SAM type long term wind stress time series, with units $10^{-2}m^2/s^2$ . . . . .	85
5.3	a) Normalised power spectral density of kinetic energy, potential energy and wind through the drake passage; b) Squared coherence of kinetic energy and potential energy through the drake passage with wind. . . . .	87
5.4	EOFs and the corresponding PCs of PE of a, b) Pacific Ocean, c, d) Atlantic Ocean and e, f) Indian Ocean . . . . .	88
5.5	EOF and the corresponding PC of barotropic stream function . . . . .	90
5.6	Lag plots showing the time taken for the PE to travel from the Southern Ocean to the other ocean basins. The time scale of adjustment is calculated by using lag cross correlation. . . . .	91
5.7	Power spectral density of KE and PE . . . . .	92
5.8	Power spectral density of a) PE and b) KE. [All psd in units of $(m^3/s^2)/year^{-1}$ ] 93	
5.9	Squared coherence of kinetic energy and potential energy with wind variability in a) Atlantic Ocean, b) Pacific Ocean, c) Indian Ocean. d) Squared coherence of potential energy with wind variability in all three ocean basins . . . . .	94

5.10 EOFs and the corresponding PCs of PE of a, b) Pacific Ocean, c, d) Indian Ocean and e, f) South Atlantic Ocean . . . . .	95
5.11 Lag plots showing the time taken for the PE anomaly to travel from the North Atlantic Ocean to the other ocean basins. . . . .	96
5.12 Power spectral density of KE and PE. [All psd in units of $(m^3/s^2)/year^{-1}$ ] . .	96
5.13 Power spectral density of a) PE and b) KE. [All psd in units of $(m^3/s^2)/year^{-1}$ ] . .	97